

Nanofabricated structures and microfluidic devices for bacterial communities

Elena Mancinelli

Master of Science by research

University of York
Electronic Engineering
November 2020

Abstract

Bacteria commonly live in diverse and dense communities interacting through physical contact and through the exchange of biochemical metabolites. Studying these interactions is of paramount importance not only to harvest the full metabolic potential of the microbial world but also to deepen our understanding and treatment of infectious disease.

While common co-culturing methods can be adapted to the study of bacterial interactions, they typically operate within bulk cultures and do not provide physical separation between different bacterial species. This limits the ability to study spatial and temporal differences in bacterial interactions at the single cell level, prevents the optimization of growth conditions for each species in the bacterial community and masks heterogeneity within the bacterial community.

This thesis discusses the potential of microfluidic devices to study chemical interactions between different bacterial species individually cultured in independent growth chambers separated by hydrogel membranes. Two PDMS microfluidic platforms for culturing of individual bacterial species have been fabricated using Direct Laser Writing as lithography technique, and tested by inoculating with *Escherichia coli*. Bacterial growth within the microfluidic device was monitored using optical microscopy and an image processing algorithm developed to quantify bacterial growth at the single cell level. Bacterial growth within the device was confirmed over a 12-hour period albeit at an extremely slow growth rate.

It was observed that successful inoculation of the culture chamber was critically dependent on the geometry of the microfluidic device. Computational models were performed using COMSOL to better understand fluid flow within the devices and subsequently used to optimise the design of a double-layer PDMS microfluidic bacterial culture system. This double-layer microfluidic module could ultimately be fabricated in an array format in which adjacent chambers are connected via a permeable hydrogel to enable co-culturing of mixed bacterial species.

Contents

Abstract	2
Contents	3
List of Figures	5
Acknowledgements	7
Author's declaration	8
1 Introduction and aims	9
1.1 Background	9
1.2 Goals of the project	11
2 Literature Review	14
2.1 Introduction	14
2.1.1 Importance of microbiota and microbial communities study	14
2.1.2 Need for co-culture systems	17
2.2 Microfluidics: technology for microbial co-culture systems	18
2.2.1 Bacterial culture in microfluidic platforms	19
2.2.2 Microfluidic co-culture systems	26
2.3 Conclusions	44
3 Materials and methods	46
3.1 Fabrication of a sealed microfluidic PDMS device	48
3.2 Experimental techniques: Direct Laser Writing	49
3.2.1 Focusing height and dynamic lithography parameters	51
3.3 Mould preparation	55
3.3.1 Silicon substrate preparation	55
3.3.2 Coating and exposure	55
3.4 PDMS replication moulding, PDMS cutting and PDMS-glass bonding	59
3.5 Double layer PDMS device	60
3.6 Sample preparation, device loading, experimental setup and post-processing . .	60

4	Preliminary results and discussion	62
4.1	Microfluidic compartments separated by nano-channel	62
4.1.1	K-CL: DLW parameters optimisation	63
4.1.2	SU-8: DLW parameters optimisation	64
4.2	Microfluidic module for bacterial culture	68
4.2.1	First design: back-pressure and priming difficulties	68
4.2.2	Second design: back-pressure and priming difficulties	70
4.2.3	Third design: clogging and difficulties in the specific localisation of bacteria within the device	71
4.2.4	Double height culturing device	75
4.3	Bacterial cell counting	80
4.3.1	Binary image creation	80
4.3.2	Bacterium area estimate and bacteria counting	84
5	COMSOL simulations	94
5.1	Priming difficulties and channel dimension: back-pressure	94
5.2	Device design and bacteria confinement	97
6	Conclusion and future prospective	100
6.1	Toward a mixed-species co-culturing device	101
A	Appendix: Dilase 650 for DLW lithography	104
A.1	Physical equipment	104
A.2	Software suit	105
A.2.1	KloeDesign	105
A.2.2	DilaseSoft	106
	Bibliography	107

List of Figures

1.1	Microfluidic platform operating principles: 3D scheme	12
2.1	Main motivations for co-culture experiments	17
2.2	Microfluidic device for channel culture: working principle	19
2.3	Bacterial micro-channel culture for antimicrobial susceptibility testing	20
2.4	Mother machine microfluidic chip	21
2.5	Micro-patterned agarose pad	21
2.6	Microfluidic device for chamber culture: working principle	22
2.7	Bacterial micro-chamber culture for biofilm formation analysis	23
2.8	PDMS double layer microfluidic device for chamber culture: working principle	24
2.9	Bacterial micro-wells culture in a two layer PDMS device	25
2.10	Single bacterium micro-chamber culture	25
2.11	Common approaches for microfluidic co-culture systems: review	27
2.12	Microfluidic array with cellular valves for single cell co-culture	28
2.13	Microfluidic device to study bacterial behaviour in sub-micron channels	29
2.14	Bacterial behaviour in sub-micron constriction	30
2.15	Colonisation of structured habitats by competing bacterial populations	31
2.16	Hydrogel synthesis: from a hydrophobic polymer to a hydrogel	32
2.17	Microfluidic co-culture system for investigation of bacterial cancer targeting	33
2.18	Microfluidic co-culture system: compartments separated by PEG hydrogel barrier	34
2.19	Gel integration for microfluidic application: microturbidostat for bacterial culture	35
2.20	Microturbidostat for bacterial culture: agarose flow-solidification	36
2.21	Hydrophobic surface to confined gel area: example	38
2.22	Hydrogel malleability: a microfluidic co-culture device to simulate bladder cancer micro-environment	39
2.23	Bacterial culture microfluidic chambers separated by membrane: design	41
2.24	Microfluidic compartments separated by a membrane: synthetic community of three bacteria species	41
2.25	Microfluidic compartments separated by membrane for the study of a synthetic community of three bacteria species: results	42
2.26	Microfluidic compartments separated by a membrane: recreating blood-brain barrier physiology	43
3.1	PDMS device fabrication: flow chart	47
3.2	Lithography process by DLW	50

3.3	Overall Dilase 650 system for DLW	51
3.4	Over and under-exposure of negative photoresist	53
3.5	Focusing height optimisation	54
3.6	Photoresist profiling	56
4.1	0.5 μm thick K-CL layer: stylus profile	63
4.2	500 nm high K-CL: lithography parameters optimisation	64
4.3	2 μm thick SU-8 layer: stylus profile	65
4.4	500 nm wide line on a 2 μm high SU-8 layer	66
4.5	500 nm wide line on a 2 μm high SU-8 layer: optimised lithography parameters	67
4.6	Platform for bacterial culture: design N° 1	69
4.7	10 μm thick SU-8: spin curves for different spin speeds	70
4.8	Platform for bacterial culture: design N° 2	71
4.9	Platform for bacterial culture: design N° 3	72
4.10	Platform for bacterial culture: design N° 3 after bacteria inoculation	73
4.11	Setup for device priming	74
4.12	Platform for bacterial culture: design N° 3 - bacteria in the culture chamber	74
4.13	Double layer SU-8 mould: schematic design	76
4.14	0.5 μm thick SU-8: spin curves for different spin speeds	77
4.15	0.5 μm high SU-8 layer: lithography parameter optimisation	78
4.16	20 μm thick SU-8 layer: stylus profile	79
4.17	Double layer SU-8 mould	79
4.18	Double layer SU-8 mould: PDMS replica	80
4.19	Image processing algorithm: binary image correction	82
4.20	Image processing algorithm: flow chart and results	83
4.21	Single bacterium area estimate: first evaluation	84
4.22	Single bacterium area estimate with <i>regionprop</i> function: average values	85
4.23	Single bacterium area estimate with <i>regionprop</i> function: minimum values	86
4.24	Single bacterium area: manual and automatic estimate comparison	88
4.25	Manual and automatic counting comparison on experimental dataset	89
4.26	Experimental results: <i>E. coli</i> W3110 growth in the device	90
4.27	Bacterial reference growth curve in batch culture	90
4.28	Manual and automatic counting comparison on additional datasets	92
5.1	Device inlet modelling: geometry and setup	95
5.2	Device inlet modelling: COMSOL simulation results	96
5.3	Device inlet modelling: pressure drop versus $\frac{W_{channel}}{D_{inlet}}$	97
5.4	Microfluidic bacterial culture device modelling: velocities field	98
5.5	Double-height device for bacterial culture: COMSOL simulation results	99
6.1	Device for bacterial co-culture in monolayer chambers: proposed design	102
A.1	Dilase 650 system for DLW: lithography setup	104
A.2	KloeDesign user interface: screenshot	105
A.3	DilaseSoft user interface: screenshot	106

Acknowledgements

I would like to thank all the inspiring people I had the opportunity to share this past turbulent year with. It is also thank to each one of you that this thesis has been completed, despite everything. I can not deny that I was a little scared when I moved to the UK from Italy to start this year of study and I have to admit that this 2020 has given me plenty of reasons to feel disoriented. However, it is only thank to all of you that I never felt alone, despite the distance from my homeland.

First, I would like to thank my supervisors Dr. Steven Johnson and Dr. José Juan-Colas for the knowledge they accepted to share with me. Pepe, because this is how you like to be called and this is the nickname that best suits you and your spirit, I can never be grateful enough for trusting me, for introducing me to the “scientific research” with passion and sincerity and for supporting me until the end. Steve, having you in my supervisory panel is a priceless fortune. Your advices are precious food for thought that will guide me for years to come, I am looking forward to work with you in the future.

I would like to thank all the members of the Bio-Inspired Technologies research group in York for never making me feel “the new one”, all your advices, talks and laughters reached me loud and clear, despite the building in between our offices. Thanks Kalum for sharing with me the “drama” of the fifth non-working device of the day, you were always there for me.

A big thank you to Prof. Thomas Krauss for giving me the opportunity to receive his priceless advice and thanks to all his Photonics research group for always helping me with patience. Thanks to Dr. Giampaolo Pitruzzello because his advice has always been fundamental, after all we had the “bacteria” as “common topic”.

Last but not least, an endless thank you to my family. Fabio, because he always allows me to find his hands. My mom, my dad and my brother because they are, and they always will be, the basis that supports everything.

Author's declaration

I, Elena Mancinelli, declare that this thesis is a presentation of original work and I am the sole author. This work has not previously been presented for an award at this, or any other, University. All sources are acknowledged as References.

Where I have included the published work of others, I have made it clear to give the relevant references and all referenced work is listed in the Bibliography chapter of this thesis. Where I have collaborated with other researchers at the University of York, I have given acknowledgements in the main body of the text.

There are no relevant published papers or conference papers to include for this thesis.

Chapter 1

Introduction and aims

1.1 Background

The term *microbe* groups together all unicellular organisms with microscopic dimensions such as bacteria, fungi and protozoa but it also includes viruses, entities at the extreme border of the living world. Microbes, also called microorganisms, have been documented as the earliest life forms that appeared on Earth, around four billion years ago. Since then, they have proliferated in all environments, from ocean trenches and polar caps, to our homes and body. Although primarily known as causes of diseases, even lethal, if microbes did not exist human beings would become extinct in a short time. In fact, most of the time, our contact with them is not only harmless, but indeed also beneficial.

Microbiology is the branch of biology that guides the main research questions of the current work. Microbiology studies microorganisms with particular attention to their physical-chemical characteristics and the interactions that microbes have with the environment and with each other. Since the early years of the discipline, it was clear that microbes are highly social organisms that typically live in dense and heterogeneous communities [1], cooperating or competing to preserve and promote their growth in the group [2], [3]. This gives rise to a complex and dense network of interactions between bacteria and between the community and the environment. Understanding these interactions is critical not only for managing infectious disease but also more broadly e.g. green chemical processing and environmental remediation.

Most of the infections that affect humans are polymicrobial. For example, pulmonary infections in Cystic Fibrosis adult patients are typically associated with two principal bacterial strains: *Staphylococcus Aureus* and *Pseudomonas aeruginosa*. It has been observed that when these are detected together, the health consequences for the host are more severe [4]. Critically, these bacterial species have acquired a strong resistance to antibiotics and current therapies could soon become ineffective. Co-culture experiments confirmed a link between resistance to antibiotics and interactions between the two strains [5]–[7]. As a result, international scientific attention is focusing increasingly on cystic fibrosis not only because it is the most common genetic disease affecting Caucasian populations, currently affecting in the United Kingdom alone more than 10,500 people [8], but also because in 2017 the World Health

Organization (WHO) prioritised the development of alternative therapies for the treatment of *Pseudomonas aeruginosa* and *Staphylococcus aureus* infections respectively [9].

One of the challenges facing the development of alternative treatments is the lack of species-independent, standard co-culture protocols that are able to map interactions between bacterial species.

In laboratories, bacterial strains are typically grown and observed at the macro scale; bacteria are suspended in liquid medium inside a test tube or deposited on solid growth medium in a Petri dish. Since these techniques are simple and well documented, to date most of the attempts of realising a co-culture system have consisted of integrating them with modern analytical techniques. In this sense, common approaches include mixed co-cultures in tubes followed by genotyping or analytical phenotypic measurements to evaluate relative species abundance and growth [10], phenotypic observation of bacterial colonies cultivated on agar plates [11] or conditioned medium experiments [12]. A conditioned medium is a liquid medium where first a bacterial species is cultured, then it is filtered out from the microorganisms, enriched with additional nutrients and cultured with a second new species. While stable, these methods limit the possibility to access high resolution spatial or temporal information within an individual strain and eventually about individual bacteria or the nano-sized secondary metabolites exchanged as chemical signals [13]. Moreover, controlling the spatial organisation at the microorganism scale level may be needed to recreate the micro-patterned communities that bacteria form in natural environments [14], [15], for example to avoid any physical contacts which could result in undesired interactions between bacteria that may be difficult to trace, when characterising chemical interactions between strains. Furthermore, the growth conditions, such as carbon source, oxygen concentration, pH and temperature, are uniform across the entire culture. This is severely limiting in co-culture experiments where optimal conditions for each bacteria often differ. For example, a common issue in artificial co-cultures occurs when the faster growing species consumes the available nutrients with a rate that makes it impossible to monitor the growth of the other species.

Microfluidics is a discipline that stems from micro-fabrication to enable control over small volumes of liquid, generally less than a millilitre, inside small structures whose dimensions generally do not exceed tens of millimetres and where a series of tasks such as transport, mix and separate fluids can be fulfilled. Since the emergence of microfluidics in the early eighties, biologists, scientists that work mainly with liquid samples, have starting moving, when possible, experimental procedures and assays from lab benches into small portable microfluidic devices. The immediate benefits of this change are obvious: these devices occupy little space in the laboratory so are easy to store and working with small volumes of liquid means reducing the amount of reagents and analytes needed for the experiments with a consequent limitation of costs. Furthermore, at the micro-scale, fluids behave in a substantially different way compared to the macro-scale. In fact at this scale flow is governed by viscous forces and the effects of the momentum have little importance. A key consequence of this phenomena, widely exploited in microbiological studies, is that mixing between fluids can happen only through diffusion without physical intermixing of fluids. This allows to precisely control chemical gra-

dients at bacteria scale level and thus deepen the study of the ability of bacteria to respond to chemical stimuli revealing mechanisms impossible to observe with macro-scale experiments.

Moreover, microfluidics is increasingly providing microbiologists the possibility to isolate, so directly observe and manage, single bacteria within a culture. When microfluidic platforms are combined with tools such as membranes, hydrogels or nano-slits, they enable culturing of multiple strains that are physically separated while free to interact via molecular diffusion. These systems have already given access to information previously inaccessible. For example, the ichip [16], an array of microwells separated by a permeable membrane, allows the observation of bacteria strains otherwise uncultivable. A review of the main microfluidic culture systems is given in chapter 2.

1.2 Goals of the project

From the previous section it has emerged that new systems for artificial mixed bacterial communities are of critical interest to overcome the main limitations associated with bulk culturing procedures. Specifically, in order to control and monitor interspecies communication while allowing quantitative analysis of single species proliferation in a community, it is essential to develop a co-culture system to mimic the niche growth condition for each bacterial strain.

This project originates from the clinical interest in deepening the knowledge of polymicrobial infections affecting cystic fibrosis patients' airways. Such bacterial infections can seriously damage the lungs and develop high antimicrobial resistance. This condition can worsen, and in most cases, leads to respiratory failure and early death.

Our solution consisted of a Polydimethylsiloxane (PDMS) microfluidic platform capable of physically separating *Pseudomonas aeruginosa* and *Staphylococcus aureus*, allowing them to grow independently but exchange molecules. We aimed to design, build and characterise the platform starting from the hypothesis that chemical signalling between the two species could be affected by changes in the external conditions such as temperature and antibiotic administration and that this interaction would be reflected in the alteration of species growth rates. Nano-channel connection between independent cultures defined either through lithographic approaches or the use of hydrogels, have been proposed as possible solutions. The operating principles of both platforms are shown in figure 1.1. Briefly, bacteria, whose dimensions are in the range of few micrometers, are not expected to migrate through a channel less than $1\mu\text{m}$ wide or the network structure of an hydrogel, on the other hand nano or sub-nano sized particles should diffuse through both a nano slit and a block of hydrogel.

Research focussed initially on confirming that, after inoculating the microfluidic platform, the bacteria could survive and proliferate with a rate sufficient to monitor their growth. Once optimised growth conditions were ensured, differences between cultures performed in the PDMS platform and those performed following typical macro-scale techniques were compared.

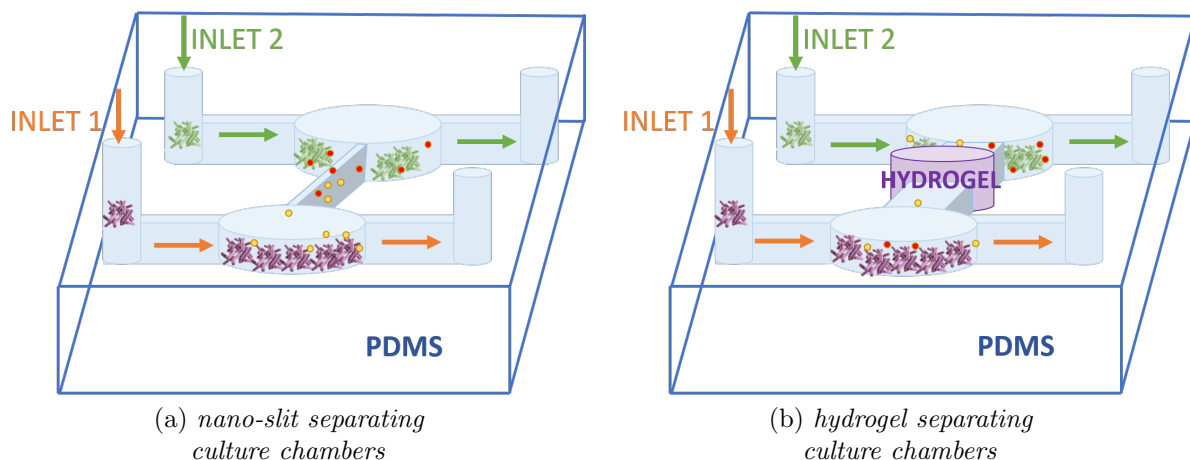


Figure 1.1: Microfluidic platform operating principles: 3D scheme. Two independent bacteria culturing chambers in PDMS separated by a nanoslit (a) and by an hydrogel (b). Working principles are the same in (a) and (b): only nano and sub-nano sized particles can diffuse from one chamber to the other. Bacteria species are respectively represented as purple and green rods, the yellow and red circles are metabolites. Colours are not real and the overall proportions do not replicate the real ones.

To evaluate the growth rate, individual bacteria were counted with image processing techniques from still images acquired with a bright-field camera mounted on a phase contrast inverted microscope. In order to be compatible with this imaging system, the microfluidic platform must:

- include a specific and well-confined area where bacteria can be cultured and observed;
- force bacteria to grow in monolayers.

In this way we are sure to focus the microscope in the correct area of the device and that one bacterium in a picture actually coincides with one bacterium only and it is not hiding others behind it. Thus, data collected from different experiments carried out in the same device, or in its identical reproductions, are comparable.

According to the project plan, conceived at the beginning of the academic year, once a device for culturing a single bacterial species was built and optimised, this would be integrated in a co-culture system in which two bacterial species would communicate exclusively via the diffusion of small signalling molecules. This would be achieved using a nano-slit connection or an hydrogel block and a limited number of experiments were performed. In the final system it would then have been necessary to observe whether and how the bacterial growth rates had changed by altering external conditions. At this point, based on the time left, there was also the prospect of thinking about a possible way of sensing the metabolites.

The outbreak of the COVID-19 pandemic and the lock-down measures taken in the United Kingdom since March 23, 2020 completely stopped all laboratory activities at the University of York. This project has been severely affected and what is presented in this thesis is the

result of an effective laboratory research period of six months, instead of the full one year period. As a result of this significantly reduced experimental research, the project aims were refocussed and this report presents experimental data collected before the lock-down, coupled with COMSOL simulations and MATLAB code for cell counting.

Therefore, a prototype of a microfluidic platform for bacterial culture remains the main outcome of this work. As a proof of its operating principles, it has been inoculated with a non-pathogenic *Escherichia coli* strain, widely used in the microbiological research, diluted in its medium. Bacteria were cultured in the PDMS platform, at room temperature, without supplying additional nutrient and monitored over a period of 12 hours.

We believe our results lay the groundwork for the design of a more complex co-culture device consisting of one replica of the culturing module for each strain to include in the study, and hydrogels to achieve the physical but not chemical separation among strains.

Chapter 2

Literature Review

2.1 Introduction

In the late 1800's, Robert Koch first highlighted the existence of a cause-effect connection between the presence of bacteria in the body and specific diseases. The observation of individual bacterial strains in pure cultures has since become a key procedure in microbiology and great efforts have been made over the past 150 years to isolate and study as many strains as possible. Despite this, since the early years of the discipline, it was clear that bacteria were social organisms that preferably live in communities [17]. The dense network of interactions between bacterial species and strains holds key information for numerous application areas, notably in healthcare, as in the case of polymicrobial pulmonary infections in Cystic fibrosis patients. For this reason, since the beginning of the 21st century, engineers, physicists and biologists have been working together to develop co-culture systems able to provide different kinds of separation between multiple species.

Lisa Goers et al. [18] have briefly listed in a review the most popular innovative methods for observing interactions between bacteria. They divide these new systems in two groups:

- microfluidic systems;
- solid support systems.

For the current literature review, I have focused on microfluidic systems as the best solution to overcome the most common problems related to conventional approaches.

2.1.1 Importance of microbiota and microbial communities study

Microbes are part of our daily life. For example, many foods and beverages widely consumed in Europe are produced or preserved through fermentation processes which are possible thanks to the action of yeasts (microorganisms that belong to fungus kingdom), or bacteria. For example, a 125-gram pot of yogurt contains around a billion live bacteria (1×10^9). Wine, beer, bread and chocolate are all products that would not exist as we know them, without microorganisms.

In addition to being present in the food we eat, microorganisms also proliferate in the oceans, the soil, in our houses, on our desks, on our skin, and even inside our body. Given their pervasiveness and diversity [19], in 2001 the term *microbiota* appeared, for the first time, to indicate the whole of microorganisms that live in a specific environment [20]. This must be intended not only as a natural habitat but also include a multicellular host organism such as plants, animals and humans.

When the multicellular host is a human, we address to the set of microbes that live in symbiosis with the host as *human microbiota*. Again, in this case, numbers are incredibly high; the human body is estimated to host, on average, about $10^{13} - 10^{15}$ bacteria. Therefore, inside our body, microbes are likely to be more numerous than human cells themselves [21]. This may sound alarming since many diseases are caused by viral, bacteria, fungal and protozoan infections. In reality, especially when it comes to bacteria, many strains permanently living inside our body are not only harmless, but actually cooperate with us to boost our immune system to fight pathogens and contribute to a proper performance of host basic metabolic cycles [22].

The close link between a human host and its associated microbiota has been confirmed by the *Human Microbiome Project* (HMP); a multidisciplinary consortium of researchers assembled in 2007 with the aim of mapping the microbiome living in and on healthy human bodies [23]. Between 2007 and 2012 scientists have been able to identify more than 10,000 species of microbial cells located in different body sites, mainly skin, mouth, nose, lower intestine and vagina [24]. This has been possible thank to the emerging techniques in the fields of DNA sequencing, big data storage and data analysis, tested with great success only a few years earlier by the Human Genome Project [25].

An outcome of the HMP research initiative has been the discovery that the healthy human microbial makeup includes potentially pathogenic microorganisms and that many infectious diseases are characterised by “dysbiosis” within the microbiome [22], [26], [27]. Dysbiosis means microbial disequilibrium, namely an alteration of numerical ratio between different microbial strains, in respect to the microbiota composition of a healthy host. It may take place at any body site and includes colonisation of commonly sterile areas. Generally, microorganisms involved in the transition from a healthy to an infected host are referred to as opportunistic [27]. These species, commonly harmless, can take advantage of unusual circumstances, such as a weakened immune system, to attack and infect the host. In this sense, an in-depth study of the human microbiota is not only important to understand its role in maintaining human life, but also to gain knowledge about potentially harmful microorganisms. Such knowledge can then become key information to synthesise new and more effective drugs with interest in infections caused by bacteria with a high rate of virulence and antibiotic resistance.

Starting from the second phase of the HMP, launched in 2012, the microbiologist community began to study changes in human microbiota in relation to three host unhealthy conditions: inflammatory bowel diseases [28], type 2 diabetes [29] and premature births [30], [31]. The following years have marked important milestones in finding relations between microbial dy-

namics and diseases status. Many studies have focused on gene sequencing of microbial composition in healthy and diseased individuals, calling their differences for attention to pursue the studies in this field [21], [22], [32]. Nevertheless, as pointed out by Verónica Lloréns-rico and Jeroen Raes [32], to date, the actual outcomes in clinical research and drugs synthesis have not had the same impact.

A factor that is slowing down and complicating research in this field is the microorganisms ability to rapidly respond to habitat perturbations. Our microbiota is an extremely dynamic community and it is thus challenging to differentiate between changes in its composition due to disease rather from changes due to diet, host lifestyle and antibiotic usage [21], [22], [32]. However, this dynamism can also benefit some aspects of medical research. The rapidity with which microbial genomes can mutate and the microorganisms ability to increase or decrease the expression of specific genes, make the microbiota a pool of efficient biomarkers for different type of diseases [21], [22] from metabolic ones [33] to autoimmune ones [34] and even for tumours [35].

When studying a community of organisms, a key step is the analysis of the interactions taking place between constituent species and strains. Among microbes this aspect is particularly relevant within the kingdom of bacteria. Bacteria synthesise a large number of metabolites as chemical signals to enable communication with the other organisms in the community and with the host [36]. To classify an interaction between organisms, its net consequences for all the populations involved must be considered. Consequences can bring advantage, disadvantage or be neutral and, with this scheme, up to few hundred different interactions states can be combined with just three species involved, as showed by Tobias Großkopf and Orkun S Soyer [37]. Therefore, the large numbers of different bacteria typical of the human microbiota, make this field of study intrinsically complicated. Each change within the microbiome must be conceived as a combined action between populations that compete or cooperate to preserve and promote their own growth in the community [2], [3].

In addition, when a pathogen invades a specific body site, it is very likely that it meets the specific microbiota where it can potentially disrupt the normally benign or symbiotic community. Under these conditions, the invasion can result in a polymicrobial infection where microbial species interact in different ways and potentially change their behaviour when the close microbial composition changes [38]. Nowadays, resources in drug research are mainly invested in developing means to attack the opportunistic pathogen mostly involved during a specific infection, ignoring the dense network of interactions with the surrounding microorganisms. Although less present or less aggressive for the host, these organisms could help the main opportunistic pathogen succeed in the invasion. The possibility of cross-protection between bacterial strains capable of synthesising enzymes to inhibit the action of specific antibiotics has already been demonstrated [12], [39].

Hence, also in the fight against antibiotic resistance, with the final aim of contributing to the synthesis of innovative and effective drugs, it is essential to study microbes within the ecological communities of which they are part.

2.1.2 Need for co-culture systems

An artificial co-culture is a laboratory system in which multiple organisms are grown simultaneously while free to interact with each-other.

Especially when studying bacteria with the aim of drug discovery, co-cultures have a fundamental advantage in respect to standard mono-cultures; the presence of more than one species in the same culture system may activate genes in the bacterial genome that are silent if such microorganisms are cultured independently and thus do not interact with different species.

In this sense, access to key information in the characterisation of polymicrobial infections is not the only contribution provided by a co-culture system in the drugs research field. In fact, culturing bacteria in a community can also push microbes to produce secondary metabolites that can turn out to be bioactive compounds to be exploited for the synthesis of new drugs [40].

In reality, studying natural or synthetic cell to cell interactions is not the only purpose of co-cultures systems. In synthetic biology these technologies are widely used to investigate microbial interactions that are not commonly observed in nature. In this way it is possible to construct and observe bacterial communities capable of fulfilling functions that individual species are unable to perform with possible applications in the environmental, industrial and medical fields [18], [41].

Moreover, as already mentioned in the section 1.1, growing one bacterial species together with others can offer more favourable conditions for the proliferation of the individual species [16], [18] therefore allowing laboratory culture of species that otherwise can not be grown.

Figure 2.1, adapted from Lisa Goers et al. [18], visually summarises main reasons for carrying out a culture experiment instead of a standard monoculture.

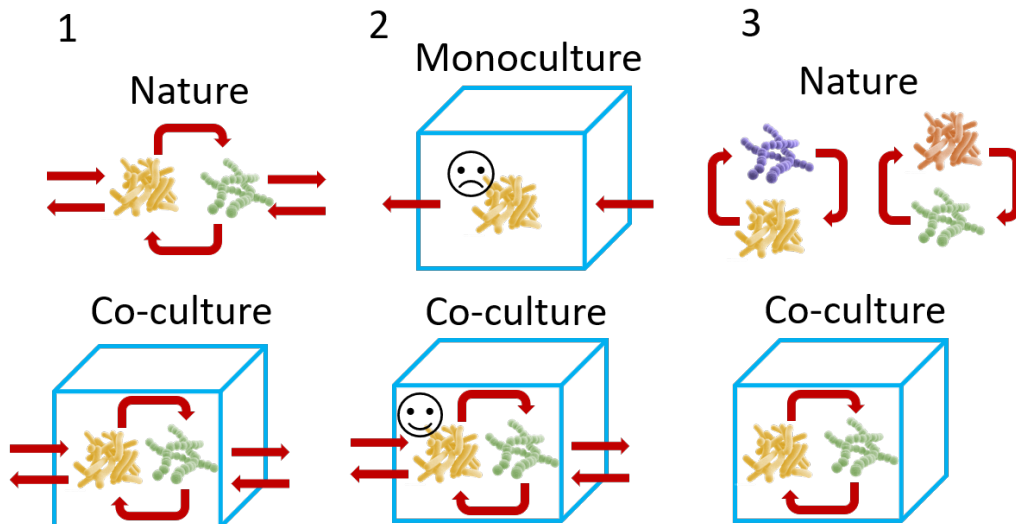


Figure 2.1: Main motivations for co-culture experiments. From left to right: three main motivations for carrying out a co-culture experiment. 1: Studying bacterial interactions happening in nature; 2: Successfully culturing species that need products of other bacteria metabolism to proliferate; 3: Allowing microbial interactions that are not possible in nature. Figure adapted from Lisa Gores et al. [18].

2.2 Microfluidics: technology for microbial co-culture systems

As already mentioned, microfluidics is the discipline that studies sub-millimetre liquid volumes (down to the femtolitres) confined in dimensions that generally do not exceed few millimetres. A microfluidic chip or platform consists of a set of micro-channels connected together in order to achieve the purpose for which the platform itself was designed. The development of microfluidics was underpinned by fabrication techniques developed for the microelectronics industry. In fact, it has been only 20 years since one of the oldest microfluidic chip ancestors [42], that innovative materials and manufacturing process, exclusively developed for microfluidic applications, started spreading. By the late 1980's, polymers replaced semiconductors and so soft-lithography was born to work these materials which are not easy to handle with standard photolithography techniques [43]. In this scenario the silicone elastomer poly(dimethylsiloxane), commonly called PDMS, has become established as particularly suitable for microfluidic applications. In respect to silicon, PDMS is less expensive, transparent so easier to couple with optical microscopy and gas permeable. This latter characteristic is an advantage also if compared to glass, the other material widely used in the field until then, and it is fundamental for biological and medical applications [43].

The context that gave birth to microfluidics was the desire to revolutionise biology and chemistry research by following the direction that electronics and computation had taken with the integrated circuit revolution [44]. In the fields of biology and chemistry, being able to reduce the size/volume at which experiments are performed brings immediate advantages such as the practicality of handling, transport and storage as well as the reduction of the volume of reagents with consequent reduction of overall cost. The possibility to integrate the microfluidic chip itself with sensors, pumps, micro valves and imaging made it possible to design real “lab-on-chip” devices.

Manoeuvring liquids at the micro-scale changes the physics of their behaviour in respect to what we observe at the macro-scale [44]. At the micro-scale, viscous phenomena prevail over inertial ones. This practically means that velocity-related motions, such as vortices, do not occur and the dominant viscous phenomena tend to keep the individual fluid streamlines constituting the flow field, parallel to each other. This type of fluid flow is known as *laminar* as opposed to the *turbulent* flow that occurs most commonly at macroscopic scale. As a result, in microfluidic chips mass transport occurs mainly by diffusion. Intermixing phenomena, happening exclusively through diffusion mechanisms, are rare and so experiments can be more easily controlled. Moreover, since devices exhibit a higher surface area to volume ratio, mass and heat transport can occur faster. This intrinsic facility to control fluid composition and temperature is of great interest in microbiology studies. In particular, considering that the scale of microfluidics devices are comparable to the size of a single bacterium and, more generally of a microorganism, this control can take place at the individual bacterium scale level. Observing the growth of a bacterial colony, individual by individual, is typically challenging with standard, macro-scale culture methods.

2.2.1 Bacterial culture in microfluidic platforms

In order to observe any microbial community, the first prerequisite that must be met is to have a system where bacteria can be inoculated and proliferate. This aspect has been widely studied and there are many examples, including review articles, in the scientific literature. Among these works, Wenting Zhou et al. [45] have recently written a review explaining recent innovations in the use of microfluidics for the study of fungi and bacteria. Zhou et al. [45] divide microfluidic devices into three large groups, according to their structure:

- devices for micro-channel culture;
- devices for micro-chamber culture;
- devices for droplet-based culture.

Microfluidic devices for micro-channel culture

Micro channel culture is probably the most common method among the aforementioned groups, largely because microfluidic channels are easy to fabricate and simple to integrate with peripheral devices for real time bacterial growth rate monitoring [45]. The basic module of a microfluidic device where bacteria are cultured in a microchannel is shown in figure 2.2.

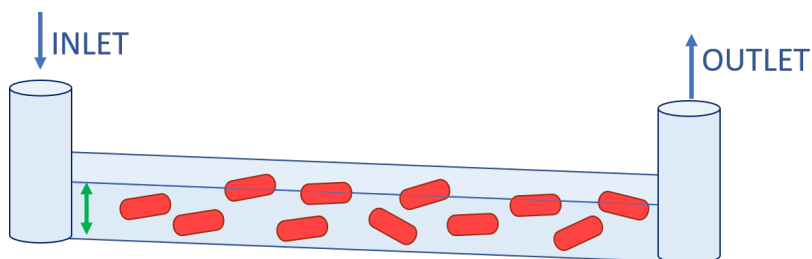


Figure 2.2: Microfluidic device for channel culture: working principle. Basic design of a device for bacteria culture in a micro-channel: bacteria are diluted in their medium and then inoculated in the channel through the inlet. Green arrow indicates the channel depth: tunable parameter to change fluid flow inside the channel.

PDMS micro-channels integrated with bacterial growth monitoring by phase contrast microscopy have been proposed as a fast tool for evaluating antimicrobial susceptibility [46]. Thanks to a high surface to volume ratio and consequent high oxygenation compared to common approaches of broth dilution and disk diffusion, Chia Hsiang Chen et al. [46] demonstrated antimicrobial susceptibility testing in just two hours instead of few days needed for standard protocols. Related results are summarised in figure 2.3. This work, as well as being an example of a successful bacterial culture experiment in microfluidic channels, demonstrates the possibility of controlling the bacterial growth rate exclusively by modifying the microfluidic channel aspect ratio (figure 2.3). Hence microfluidic approach is demonstrated to be more effective than traditional ones (e.g. Petri dish) whose small surface to volume ratio causes the oxygen flux to be only enough for low initial concentrations.

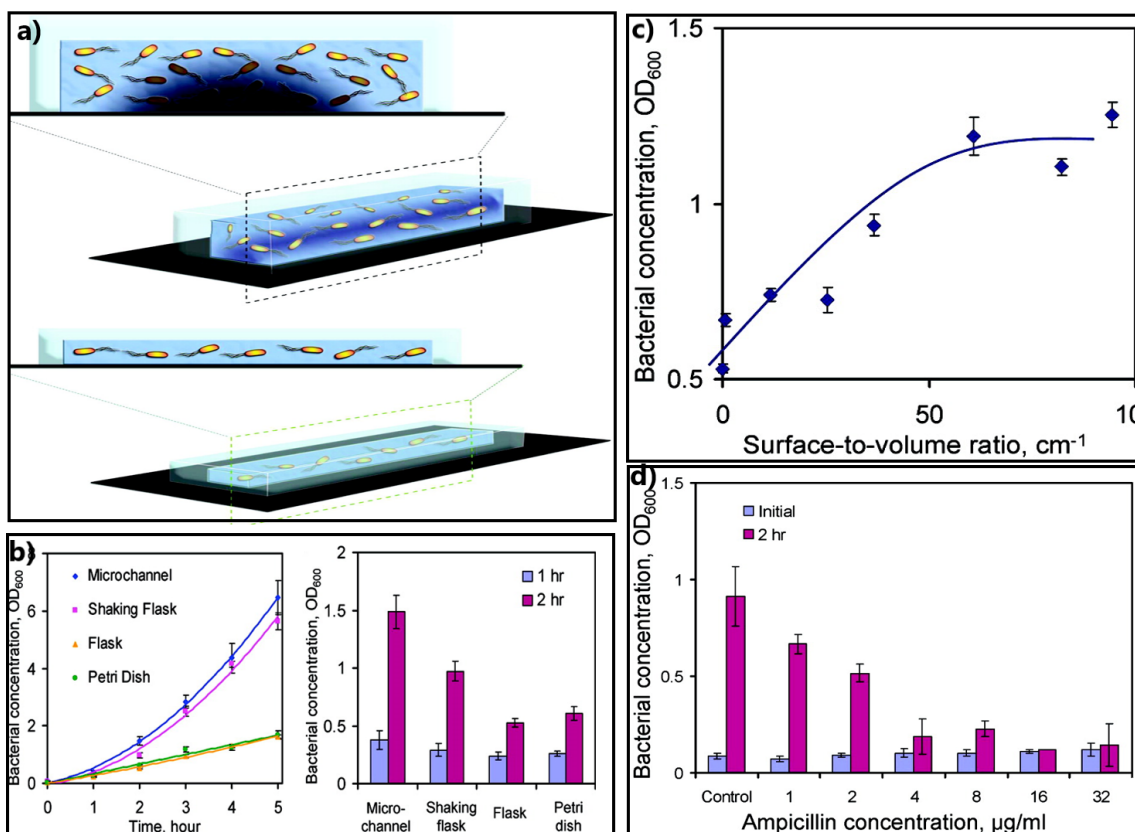


Figure 2.3: Bacterial micro-channel culture for antimicrobial susceptibility testing. a) Scheme of the device used by Chia Hsiang Chen et al.[46] for the experiments, two different channel depths are illustrated with oxygen level relatively low associated to the largest one. b) Data show a faster bacterial growth rate when microbes are cultured in microfluidic channels rather than with standard approaches. c) Graph shows an increasing in bacterial growth rate with the increasing in the surface-to-volume ratio until saturation level reach with a ratio around $60cm^{-1}$. d) Results of the Ampicillin susceptibility test on *E.coli* strain. Adapted with permission from [46]. Copyright 2010 American Chemical Society.

If the growth channel is reduced to the size of a single bacterium, *E. coli* can be constricted to grow only in the micro-channel direction. This principle is used in the device known as mother-machine. This was first introduced in 2010 [47] to allow bacterial division to be monitored at the single microorganism level. It is commonly used for rod shaped bacteria and is composed of a series of parallel, dead-end growth channels where the so called pole mother cell is localised. This design, shown in figure 2.4, can be used for a series of single cell studies such as cell growth and division observation or genetic analysis [48].

The mother machine is a clear example of the ability of microfluidic platforms to impose confinement to a bacterial colony to overcome the limits of common culturing approaches. For example, the exponential growth on agarose pads leads to complete covering by bacteria, making it hard if not impossible to extract the growth rate of a single microbe and gene expression information. This can be overcome by micro patterning the pad as shown in figure 2.5 [49]. A mother-machine like design, addressed as the *single cell chemostat*, allowed Jeffrey R. Moffitt et al. [49] to address innovative biological questions at the single bacterium level,

within a community, coupling the agarose pad culture together with a time-lapse imaging. Thanks to the micro pattern, bacteria are forced to grow in monolayers in an environment where nutrient consumption can be controlled.

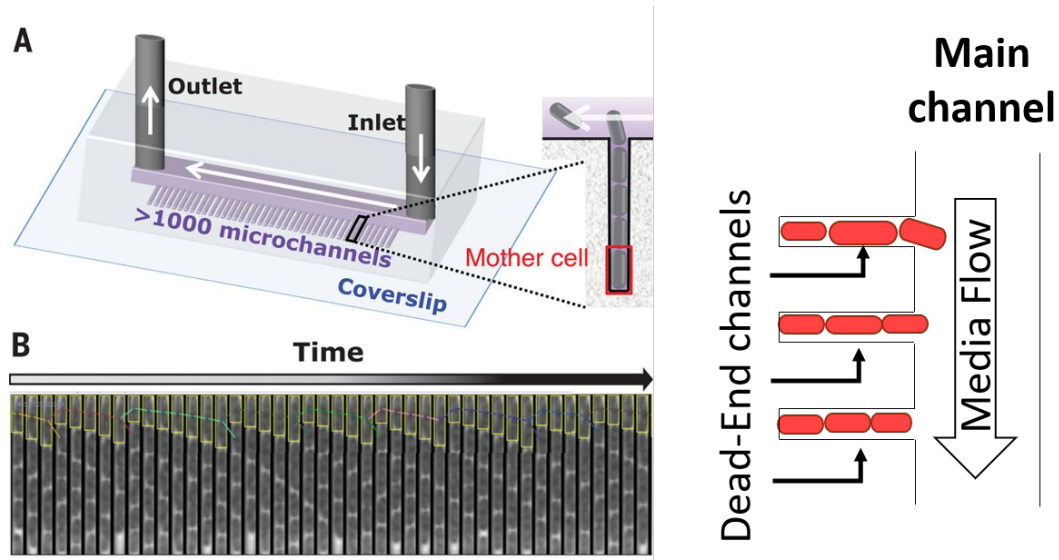


Figure 2.4: Mother machine microfluidic chip. Mother machine design and working principle: the mother cell divides and pushes daughter cells along the dead-end microchannels: once the open end is reached, the daughter cells end up in a wider channel to be “washed” away. Medium is flushed through the central channel. B shows Phase-contrast images of one microchannel over time during an experiment carried out by Lydia Rober et al. [50]. A and B adapted from [50]. Reprinted with permission from AAAS.

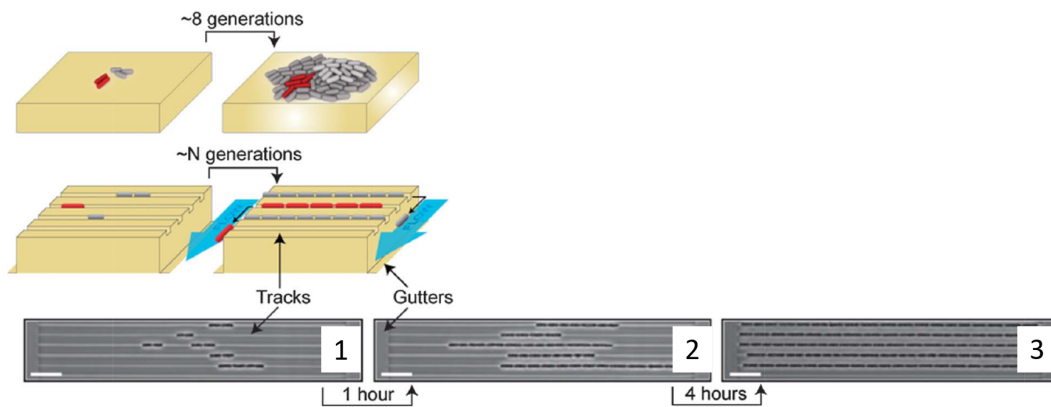


Figure 2.5: Micro-patterned agarose pad. Top row: schematic representation of what happens if bacteria are cultured in a common agarose pad, because of multiple bacterial layers, nutrient consumption and not uniform growth, the data collected after 8 generation are not useful; Middle row: micro-pattern agarose pad overcomes main limitation of the more common straight pad so measurements can be carried out without time limits; bottom line: phase contrast images of *E. coli* cultured in a micro-patterned agarose pad, scale bar are $10\mu m$. Figure adapted from [49].

Microfluidic devices for micro-chamber culture

Culturing bacteria in a micro-chamber gives more stability to the experiments [45]. In a basic design (figure 2.6), a micro-chamber is generally connected to the fresh medium source through micro-channels. This changing in shape from the inlet to the chamber causes fluid flow to slow down where the minimum flow velocity is reached inside the chamber. In a device having a shape like the one shown in figure 2.6, the considerable lowering of flow velocity in the central chamber, with respect to the remaining parts of the device, makes it preferential for bacteria to settle, proliferate and give rise to colonies in this zone.

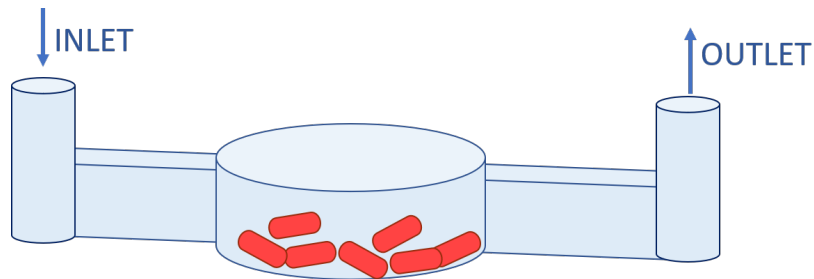


Figure 2.6: Microfluidic device for chamber culture: working principle. Basic design of a device for bacteria culture in a micro-chamber: bacteria are diluted in their medium and then inoculated in the chamber through the inlet. The micro-chamber is connected to the inlet through a narrow micro-channel.

Specific designs can further help to maintain the average flow rate in the bacterial culture chamber. For example Xiao-Yan Zhang et al. [51] used a microfluidic device consisting of an octagonal chamber surrounded by a microfluidic ring to study real-time initial biofilm formation and the effect of antibiotic on the process. The interposing of a ring-shaped microchannel around the chamber (see figure 2.7) permits biofilm growth to be studied under constant flow without altering steady culture conditions in the chamber. Flow is needed to supply nutrients and wash away both metabolites and bacteria that do not adhere to the glass substrate underneath the PDMS device. In this design, the fluid flow velocity can be changed and the consequent biofilm formation process studied in relation to this variation [51].

The characterisation of the biofilm formation process at the microscopic level and in real time is a key step to fully understand some serious infections, however common macro-scale approaches, such as shake flasks, are unable to address such questions. This is particularly challenging with those microorganisms, such as *E. coli*, whose natural ease of propulsion prevents their adhesion to a substrate. Large microfluidic chip area helps bacteria to adhere to the walls allowing for easier biofilm formation [51].

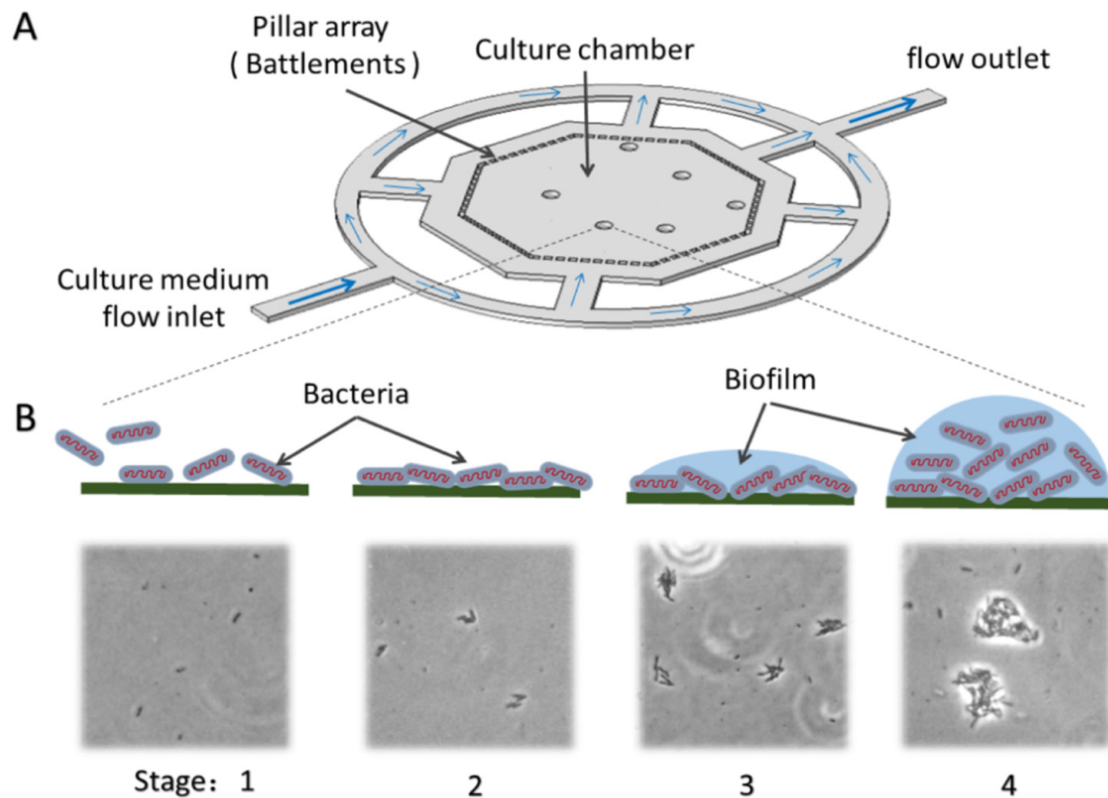


Figure 2.7: Bacterial micro-chamber culture for biofilm formation analysis. Microfluidic chambers for biofilm study. A: Schematic design of the device used by Xiao-Yan Zhang et al. [51]; little circles inside the octagonal chamber are PDMS micro pillars to prevent gas bubbles from entering in the device. B and C shows respectively schematic drawings and real acquired pictures from inverse microscope to explain biofilm formation process. Stage 1: bacteria poorly adhere on the glass substrate, stage 2: bacteria irreversible adhere to the glass substrate, stage 3: monolayer biofilm formation and secretion of substances for biofilm structure, stage 4: biofilm is formed and mature. *E.coli* is the bacterial species under investigation. Figure from [51].

Generally, when designing a device similar to the one shown in figure 2.6, the first requirement to meet it is that bacteria preferably colonise and proliferate in the central culture chamber. With motile organisms this means reducing the potential for bacteria to swim out of the chamber once bacteria are inoculated through the inlet. This can be achieved by taking advantage of gravity; if the culture chamber is lower than the inlet-outlet connection, gravity pulls the bacteria to the bottom of the well, making it more likely they will remain located within the well. One way to achieve this difference in heights is by fabricating the device from two layers of PDMS, one above the other. In this case the top part should include a channel for inoculating bacteria and supplying media, and the bottom should include the culture chamber as shown in figure 2.8. Commonly, in this case, the culture chambers are addressed as *culture wells*.

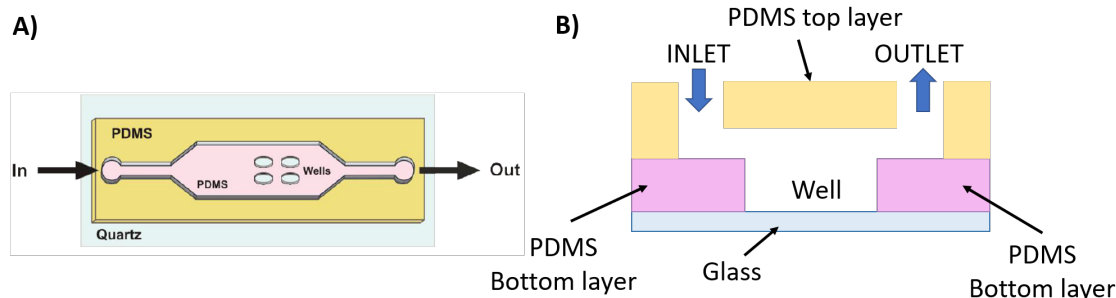


Figure 2.8: PDMS double layer microfluidic device for chamber culture: working principle. Schematic design of a double height microfluidic device for bacteria culture in wells: two layers of PDMS are positioned one above the other. A: top view of a device with 4 culture wells; B: cross section view of one well. Top PDMS layer is represented in yellow, bottom PDMS layer represented in pink. A adapted from [52]: supplementary information.

Xiaofei Yuan et al. [52] used a two layer PDMS microfluidic device to build a culturing platform to study the effect of $532 - nm$ laser irradiation at the single bacterial cell level. In fact, this wavelength belongs to the range used in Raman spectroscopy, an emerging label-free technique that use vibrational microspectroscopy as a rapid method for structurally and molecularly characterising a biological sample. Generally, it is considered a non destructive technique but laser irradiation could have effects on bacterial cells. In the aforementioned work [52] these effects are evaluated at the single cell level thanks to a microfluidic device specifically designed for the purpose and based on two layer PDMS culturing wells structure shown in figure 2.9. The device allowed changes in the growth rate at the single bacterial cell level to be monitored while increasing the irradiation dose revealing that bacteria stop dividing beyond a specific value. Such value of irradiation dose is indicated as “destruction threshold” and it is different for different bacterial strains. Thus, Raman spectroscopy should be ideally conducted below this threshold finding a good compromise between a good signal-to-noise ratio of the Raman signal and the effect of radiations on bacterial cells. Such effects increase if the irradiation dose increases and include the reduction of the growth rate and the extension of the lag time [52]. This experiment is impossible using common bacteria culture systems where the overall growth of the bacterial colonies hides the proliferation trend of the individual bacterium preventing a dynamic and real time study.

As for microchannel culture devices, the dimensions of a microfluidic chamber can also be reduced to few micrometres in order to match the single bacteria scale. By taking advantage of this possibility Fabai Wu et al. [53] could study how the expression of specific membrane proteins varies when bacteria, while growing, are forced to change their shape, adapting to that of the micro-chambers (see figure 2.10).

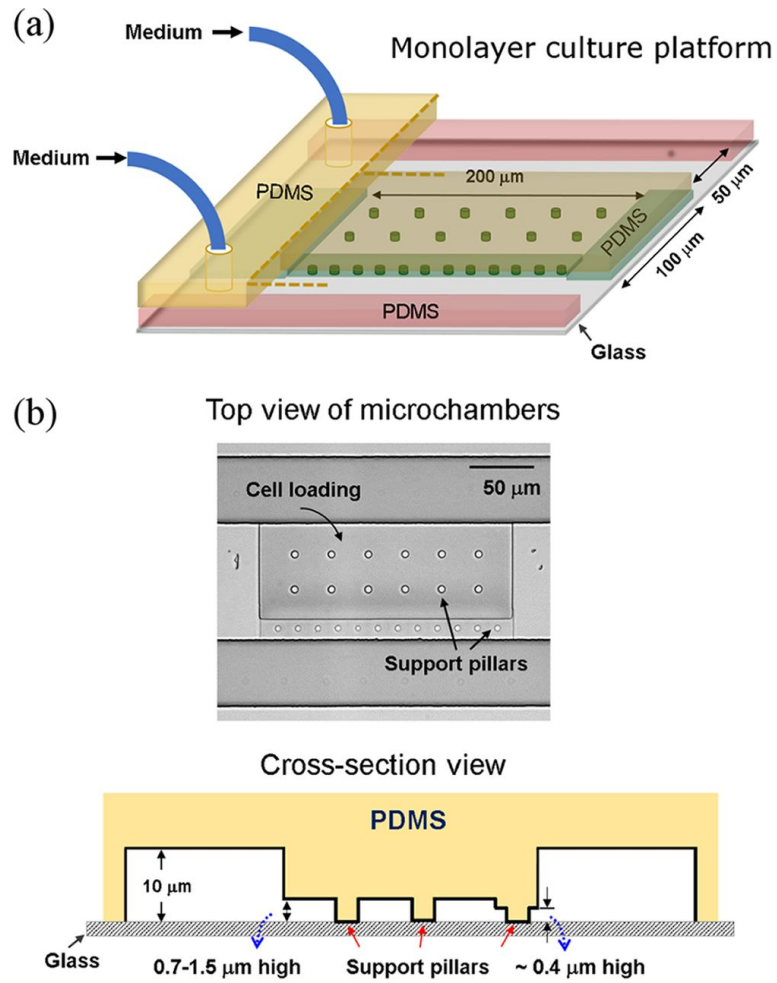


Figure 2.9: Bacterial micro-wells culture in a two layer PDMS device. Schematic design of the device used by Xiaofei Yuan et al. [52]: yellow PDMS is the top layer where the two channels are imprinted, the central green part is the lower PDMS layer used for bacterial culture (a). Top and cross-section view of the device (b). Figure reported from [52].

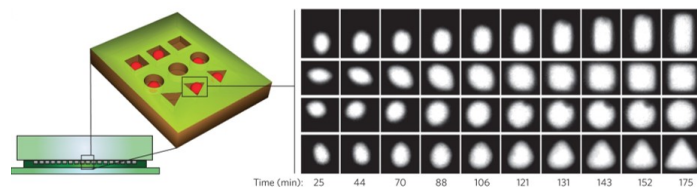


Figure 2.10: Single bacterium micro-chamber culture. Schematic structure of the device for single bacterial cells culture (left): microscope cover-glass (bottom), PDMS micro-chambers (middle) and an agarose pad (top). Right: fluorescence images of bacteria growing into defined shapes. Adapted by permission from [53], Copyright ©2015 Springer Nature.

Microfluidic devices for droplet-based culture

Using microfluidic channels and taking advantage of physical properties at the interface of two immiscible liquids, it is now possible to encapsulate single or few bacteria in a single fluid droplet [45]. Performing this type of culture allows the design of very high-throughput devices in which cells can be interrogated one at a time. For example, specific drug molecules can be incubated with individual bacteria to specifically observe how their phenotype and gene expression change. In general, compared to micro-channel or micro-chamber culture devices, droplet-based microfluidic systems require a more complex fabrication protocol. In addition to standard steps, it is necessary to establish which method of droplet formation is the most suitable and how to handle the single droplet for the specific application. In droplet-based microfluidic cell culture, nutrients availability is intrinsically limited by the maximum volume contained in a single drop. Moreover, with the final aim of studying microbial interactions, this type of microfluidic culture technique does not give easy access to information about the local micro-environment. For all these reasons, a droplet-based microfluidic device is not strictly necessary and, indeed, is not suitable for the purpose of the current work so a more traditional and standardised design has been adopted. Please refer to the review written by Minjeong Jang et al. [54] and the specific application of James Q. Boedicker [55] for additional information regarding this topic.

2.2.2 Microfluidic co-culture systems

When designing a microfluidic device for mixed bacteria co-culture there are two key decisions to take before starting its fabrication process:

1. which bacterial culture module is the most appropriate for the study;
2. how to separate the bacterial culture modules to answer the main research questions.

The previous section provided an overview of the most common approaches to culture bacteria in a microfluidic device. The next sections will review the methods most documented in literature to accomplish separation between species when cultured together in the same overall co-culture system.

Figure 2.11 gives a schematic overview of the main solutions to integrate a co-culture method in a microfluidic device. All the methods illustrated in figure 2.11 are based on dimensional filtering. Unlike bacteria whose size is in the range of a few micrometers, chemical signalling between microbes happens via diffusion of small metabolites whose dimensions do not exceed hundreds of nanometres and which can flow through nano-sized channels or the nano-sized links of a net.

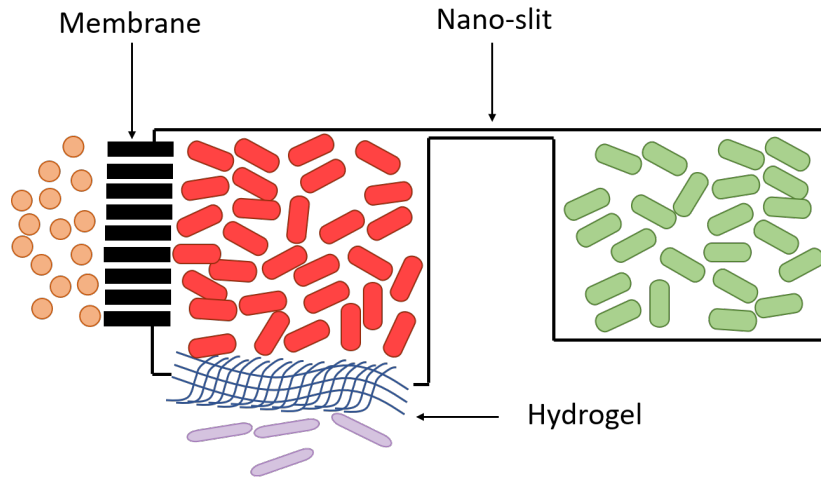


Figure 2.11: Common approaches for microfluidic co-culture systems: review. Considering a micro-chamber bacterial culture (populated by red rod-shaped bacteria in figure), in a mixed culture system consisting of two microbial species, it can be separated from the additional microfluidic culture module through: a membrane (left), a nano-slit connection (right), a hydrogel (bottom). Adapted with permission, from [56]; permission conveyed through Copyright Clearance Center, Inc.

Fluid channel connection between compartments

Starting from a microfluidic culture module, either based on a micro-channel or on a micro-chamber, the most immediate way to convert it in a co-culture system is to include a second microfluidic culture module separated by a slit of a size small enough to prevent the passage of bacteria. This solution is described as “the most immediate” because the concept itself is easy to design and should not require additional instrumentation compared to what is needed for mono-microbial culture. In reality, as shown in chapter 4, when working with nano-metric dimensions we often operate close to the resolution limit of the machines used to fabricate the devices as well as in a range where material responses to physical manipulations (such as photoresist light-sensitivity) may not reflect our expectations. Probably for this reason this co-culture system is more commonly used for mixed culture of eukaryotic cells. In fact, their bigger dimensions ($10 - 100 \mu m$), their inclination to adhere to the substrate instead of swimming in liquid medium and their poor ability to adapt to hostile environments make it easier to keep them out of a specific microfluidic compartment simply introducing a narrowing in the device.

These properties of eukaryotic cells have allowed Jean-Philippe Frimat et al. [57] to build a microfluidic array of cell traps for the simultaneous co-culture of single cells that is based on the principle of two microfluidic compartments separated by a narrow channel. Once the cells have been suspended and inoculated into the microfluidic device, shown in part 1 of figure 2.12, the fluid flow can take two different paths, both, in principle, connected with the rest of the device; one straight path along which cell traps (device narrowings) are positioned and one serpentine path free from traps. Naturally, liquids take the path with the lowest resistance to the flow (step A of part 2 in figure 2.12). In this case, this is the straight channel. Hence, flowing through the linear path, the suspended spherical cell (purple dot in the part 2 of figure

2.12) is trapped at the first device narrowing (step B of part 2 in figure 2.12). At this point the cell adheres to the substrate, flattening (lilac in part 2 of figure 2.12) and lowering again the resistance to the fluid flow in the linear path (step C of part 2 in figure 2.12). Hence, when other suspended spherical cells are inoculated from the opposite side of the device, the differences in resistance to the fluid are similar to the initial ones. This second group of cells will behave like those inoculated first, and for any path narrowings, at this point a single cell co-culture should have settled (step D of part 2 in figure 2.12).

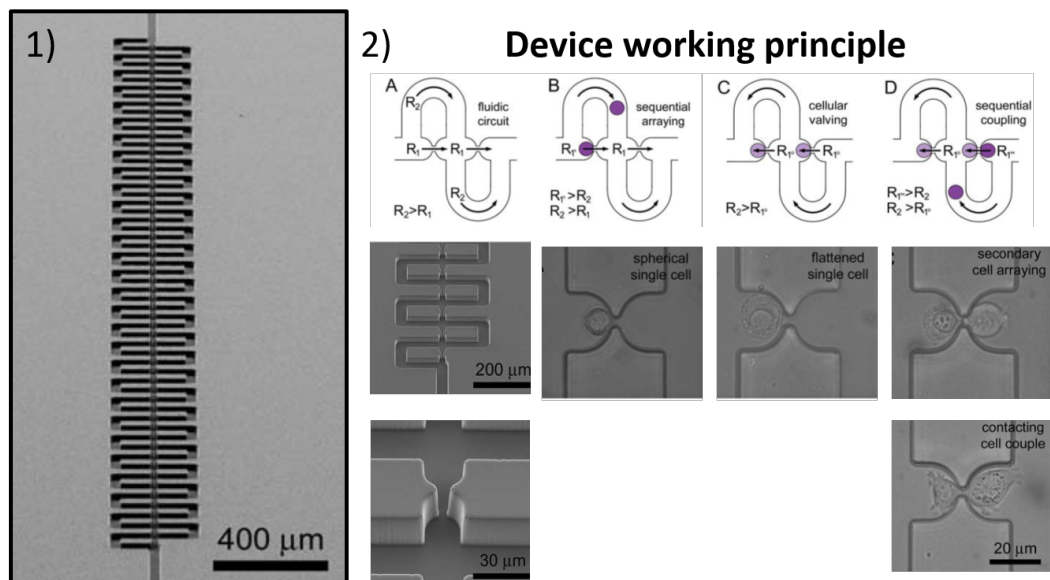


Figure 2.12: Microfluidic array with cellular valves for single cell co-culture. 1) SEM image of the overall serpentine device; 2) Device working principle: schematic representation and SEM (A) or phase contrast images (B-D) of the respective step. Step A: initial empty device configuration; Step B: spherical suspended cells (in purple) are inoculated. Step C: cells in traps flatten (in lilac); Step D: second spherical cells are introduced through flow reversal to settle a single cell coupling. Adapted from [57].

In the aforementioned example, narrowing the channel to create a cup shape (part 2 in figure 2.12) with a diameter from 1 to 2.5 times the cells diameter is sufficient to trap cells and prevent them from moving forward. Then, a small aperture (smaller than the cell diameter) at the tip of the trap allows contact with a cell coming from the opposite side of the aperture (part 2 in figure 2.12). Operating this type of device between two bacterial cells would be difficult and there are two main reasons for this:

1. bacterial adhesion to a substrate may not alter their shape sufficiently to reverse the resistances to fluid flow in the path;
2. bacterial capability to change their shape to adapt to the most extreme habitats (see figure 2.10 and reference [53]) allows them to swim or proliferate through very small gaps.

Regarding this second point, it has been demonstrated [58] that *E.coli* do not undergo any changes in motility when swimming in a microchannel wider than $1.1 \mu m$, only $0.8 \mu m$ bigger

than bacterial diameter. Hence, to physically isolate two bacterial species, a trap of the same dimensions of the cells may not be small enough in the case of bacteria. To study motility and growth of a pair of bacterial species, representative for Gram-positive and Gram-negative bacteria, respectively *Escherichia coli* and *Bacillus subtilis*, Jaan Männik et al. [58] designed a rigid microfluidic device in which a “loading channel” is connected to a “feeding channel” through parallel paths. In each path micro-chambers alternate with micro-channels of decreasing width, starting from $3\ \mu\text{m}$ (figure 2.13).

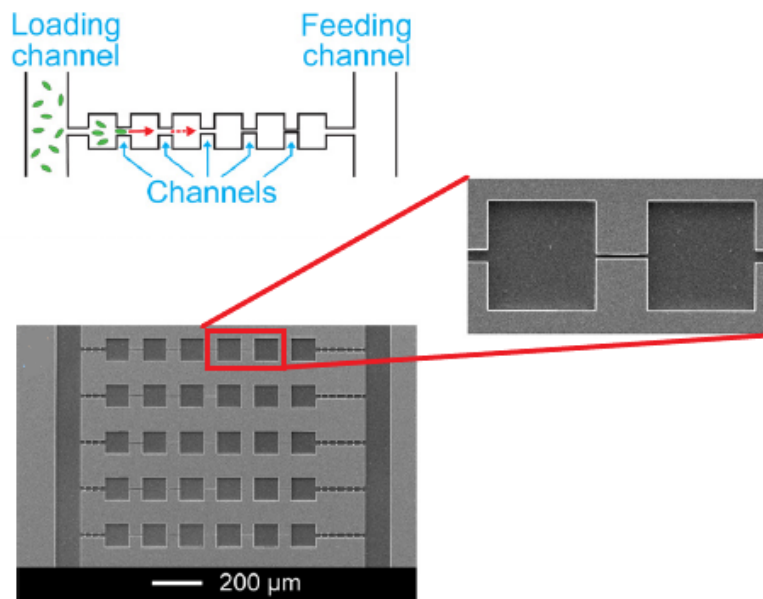


Figure 2.13: Microfluidic device to study bacterial behaviour in sub-micron channels. Schematic representation and SEM image of the silicon device used for study bacterial mobility and growth in sub-micron constrictions. Adapted from [58].

They showed that, considering \bar{D} as the average bacteria diameter, directly calculated as a part of the experiment, and W as the channel width, normal flagellar-induced motility is still possible for $W/\bar{D} \sim 1.25$, around 25 – 40% wider than bacteria diameter for both species (results for *E.coli* shown in figure 2.14). For lower W to \bar{D} ratios, the behaviours of *Escherichia coli* and *Bacillus subtilis* differ, probably due to differences in membrane composition and thickness. For ratios down to $W/\bar{D} \sim 0.5$, *E. coli* showed the ability to enter rigid sub-micron sized channels by subsequent cellular divisions starting from the channel entrance and greatly changing their shape (figure 2.14 panels D-L), while *B. subtilis* could not proliferate in micro-constrictions for ratios lower than $W/\bar{D} \sim 1$.

Therefore, preventing physical contact between bacterial species while allowing chemical communication via metabolite diffusion within a co-culture device, is feasible only provided that the nano-slit is smaller and thinner than the bacterial diameter. In reality, as widely illustrated, within a limit, bacterium may still be able to overcome the separation by proliferating

within the nano-channel. Nevertheless it is worth noticing that this ability depends on bacterial species involved, is a fairly slow process (5 hours to proliferate through a $50 \mu\text{m}$ long channel) and furthermore it is not certain that it will be exercised without adequate stimulus (in the example [58] given by the difference in concentration of nutrients).

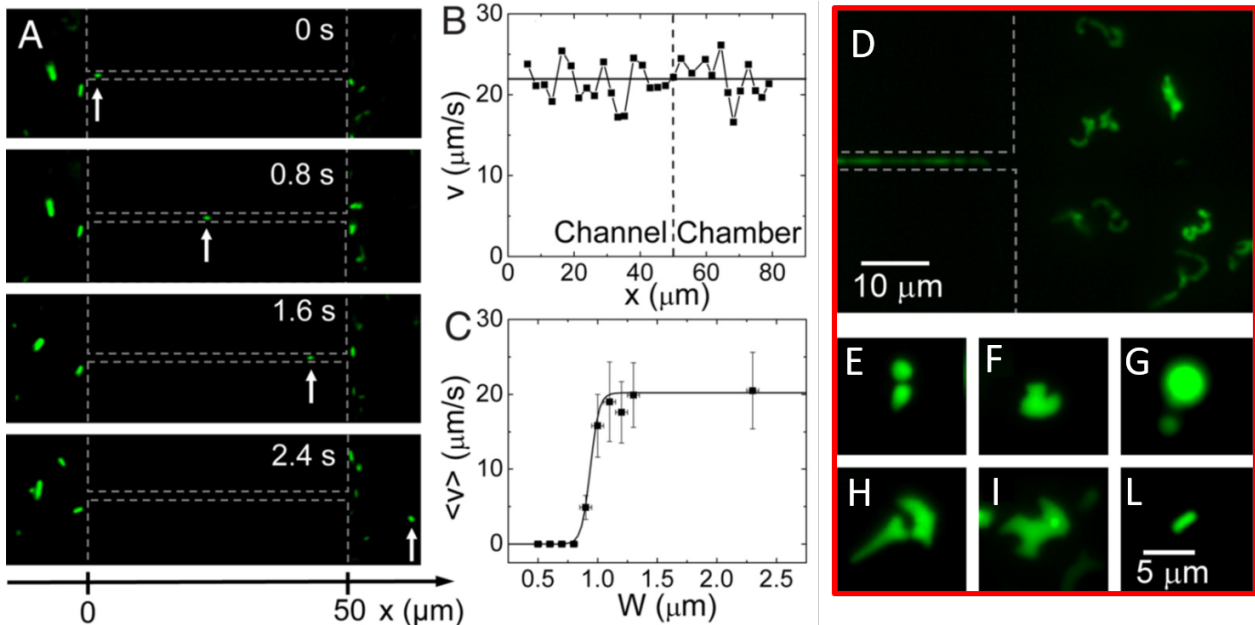


Figure 2.14: Bacterial behaviour in sub-micron constriction. A: *E.coli* bacterium (pointed by the white arrow) swimming in a channel $1.2 \mu\text{m}$ wide from left to right chamber. B: Bacterium swimming velocity versus bacterium distance along the channel (from left to right chamber: see x coordinates at the bottom panel in A). Velocity remain stable and comparable to the one in the chambers. C: Average swimming velocity versus channel width. D: *E.coli* bacteria showing abnormal shapes after growing in a $0.6 \mu\text{m}$ channel for 5 hours. Figures adapted from [58].

While possible in principle, examples of bacterial co-culture devices using this design are few in number. Among these the study conducted by Simon van Vliet et al. [59] starting from the results previously illustrated [58] showed that when two identical, but differentially and neutrally labelled, *E. coli* strains invade and colonise a micro-patterned habitat from opposite sides, their progress within the device and the collision between them are regulated by chemical interactions, among other factors, rather than physical interaction. In fact, in one of the 5 versions of the device, all contributing to the observation of the same phenomena, they inoculated the two strains into independent paths connected exclusively by small channels $200 \text{nm} \times 15 \mu\text{m} \times 15 \mu\text{m}$. Giving the fact that channels depth ($200 \mu\text{m}$) is less than half of the *E. coli* average diameter, no bacteria were able to swim through them. Figure 2.15 shows that the two bacterial fronts avoid to get too close even if physically separated, just like in all other devices where physical contact is instead allowed.

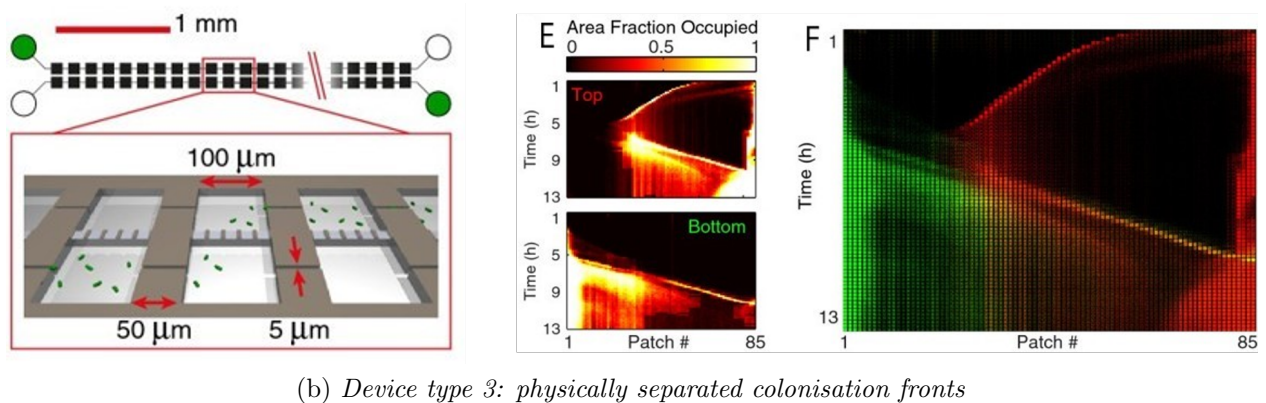
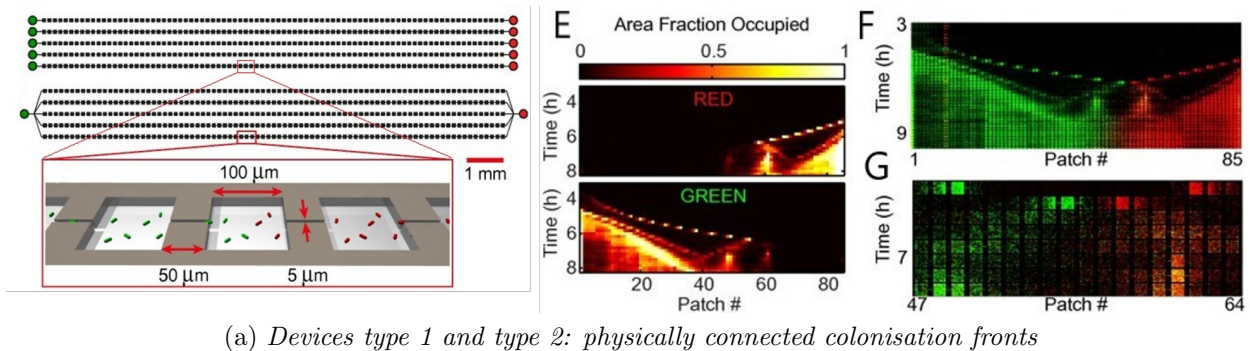


Figure 2.15: Colonisation of structured habitats by competing bacterial populations. **Panel (a)**: Device type 1 (top schematic representation) and device type 2 (bottom schematic representation) for studying bacterial colonisation phenomena. Enlargement shows the structure of three central patches (squares with side $100\ \mu\text{m}$). Area fraction calculated for green and red labelled strains, colonisation wave collision at $t = 6\ \text{h}$ in device type 1 (E), Kymograph of fluorescence intensity for the collision shown in E (F) and its enlargement (G). **Panel (b)**: device type 3 for studying bacterial colonisation phenomena (top-left schematic representation). As shown in the enlargement patches are connected through nano-sized channels where bacteria are too big to flow through. Area fraction calculated for green (bottom) and red (top) labelled strains (E), Kymograph of fluorescence intensity for the collision shown in E (F). In both panel (a) and panel (b) Kymograph of fluorescence intensity shows the two opposite fronts avoid overtaking each other after the collision. This demonstrates that this behaviour is due to chemical signalling between strains, unique type of interaction possible in the device shown in panel (b). Figures adapted from [59].

Compartments separated by hydrogels

Hydrogels are colloids composed of polymer chains dispersed in water. Water content in hydrogels account for up to 99% of their composition making them perfect substitutes for living tissue and they are used widely for growing cell cultures in laboratories as well as for tissue engineering. Moreover, starting from 1960s, thanks to their high biocompatibility, hydrogels have been widely used in the medical field in soft contact lenses, breast implants and specific treatments of burns and wounds. Chemical or physical cross-linking between polymers of hydrophilic monomers, gives hydrogels the ability to swell and incorporate such a big amount of water. In figure 2.16 the hydrogel structure resulting from different types of cross linking, and the cross linking process itself are briefly illustrated.

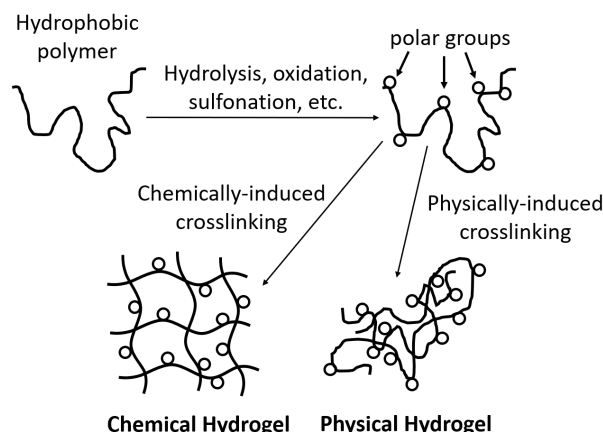


Figure 2.16: Hydrogel synthesis: from a hydrophobic polymer to a hydrogel. Polar groups are added to hydrophobic polymer chains through hydrolysis, oxidation, sulphonation or other process so resulting chains are water soluble. Cross linking can then be induced chemically or physically. In chemical hydrogels, also called *permanent*, cross-linking between polymer chains happens through covalent bonding and chemical reactions while in physical or *reversible* gels temporary connections are physically induced through ionic interaction, hydrogen bonding, thermo-induced gelation, complementary binding and hydrophobic interactions. In chemical hydrogel the final network is easier to control in term of mesh size of the net due to its more regular structure. Figures adapted from [60].

The network structure associated with hydrogels (see figure 2.16) can be used to selectively filter substances. For example, a hydrogel can allow diffusion of nanometre metabolites while preventing movement of micrometre bacteria. Thanks to their composition and working principles, hydrogels can be easily integrated in a microfluidic device. In fact, they can be inoculated in a microfluidic chip while still at the initial liquid phase and they can be cross linked once already inside the device. The great advantage of such procedure is that to include hydrogels in a microfluidic platform, the main device fabrication steps are not altered in respect to common protocols.

The use of hydrogel barriers in co-culture microfluidic platforms is a common practice in eukaryotic cell studies. Eukaryotic cells can exchange nutrients and molecules by diffusion through collagen, which simulates extracellular matrices, making it necessary to have this protein inside the channel used as a separation between two microfluidic compartments for cell culture. Collagen gel can constitute an extra physical separation between culturing compartments in the microfluidic device. This is, indeed, the case of the device designed by Jung Woo Hong [61] in which collagen gel is not only an extra separation component but, thanks to its presence, passive valves are established to separate a central bacterial culturing channel from two eukaryotic cell culturing chambers (panel (a) in figure 2.17). Results showed the tendency of facultative anaerobic bacteria, free to swim in the canal, to preferentially head towards the exit of the collagen connection to the chamber where cancer cells are located. Hence, this experiment demonstrated the possibility to target cancer cells using facultative anaerobic bacteria that move by chemotaxis towards biochemical compounds produced by cancer cell metabolism (panel (b) in figure 2.17).

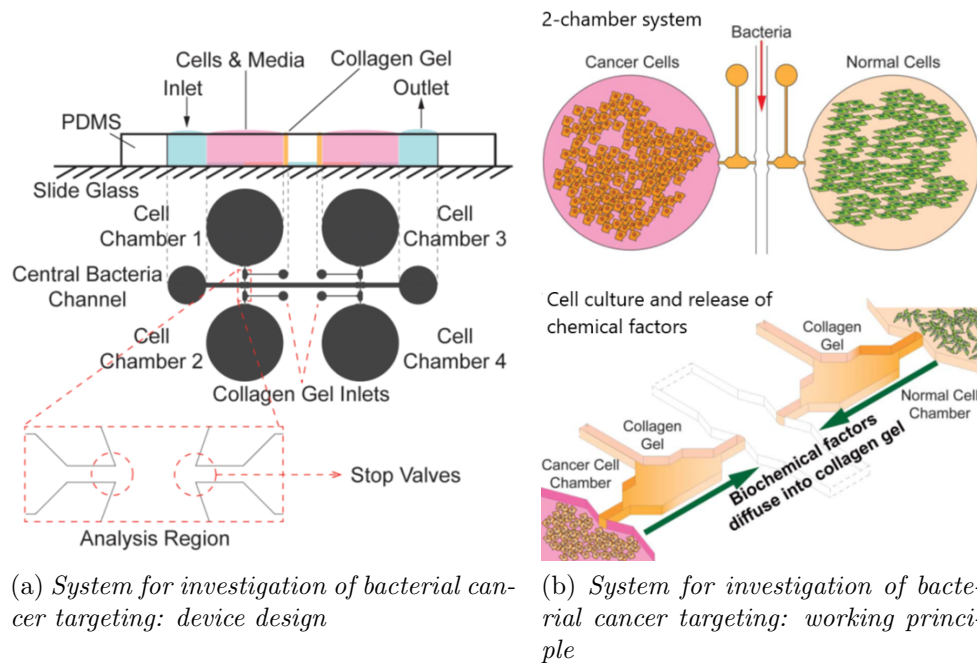


Figure 2.17: Microfluidic co-culture system for investigation of bacterial cancer targeting. Microfluidic device design: 4 independent cell cultures compartments connected through small channel filled with collagen to a central channel where bacteria are inoculated (a). Device working principle: in separated microfluidic compartments normal cells and cancer cells are respectively cultured, molecules produced by the cells. Bacteria are free to swim in the channel: experiments show that they tend to preferentially accumulate in the exit of the chamber where cancer cells are cultured. Figures adapted from [61].

Collagen gel is an example of *natural hydrogels* whose main drawback is the lack of reproducibility [60]. This is intrinsically due to their natural origin, mainly from animal organs. On the other side *synthetic hydrogels* are cheaper and easier to control but are not always biocompatible and harder to synthesise. Among *natural hydrogels* it is worth citing agar, widely used as cell culture substrate in laboratories, but also materials such as alginates studied as possible means for the delivery of small chemical drugs, wound dressing and human tissue regeneration [62]. While the most common *synthetic hydrogels* are PVA (polyvinyl alcohol) and PVP (polyvinylpyrrolidone).

A common method to trigger polymerisation in a hydrogel is through UV light. Here, a photo-initiator is added to the initial solution from which the hydrogel will originate. In this way when the solution is exposed to a source of light in a specific wavelength range, bonding between photo-initiator and polymer chains is modified and the formation of free radicals starts the cross linking process. Photo-polymerisation can easily be performed directly inside a microfluidic device in which two compartments for bacterial culture are designed to be separated by a hydrogel barrier. All that is needed is a precursor solution, a UV lamp and a region of the device intended for the insertion of the hydrogel *“in situ”*.

Dipali Patel et al. [63] have demonstrated a two-layer co-culture microfluidic device (see figure 2.18, A and B) in which a central micro-channel filled with a photo-polymerised

poly(ethyleneglycol) (PEG) hydrogel is used as physical barrier between two groups of melanoma cells (figure 2.18, B); drug resistance melanoma cells and drug sensitive melanoma cells.

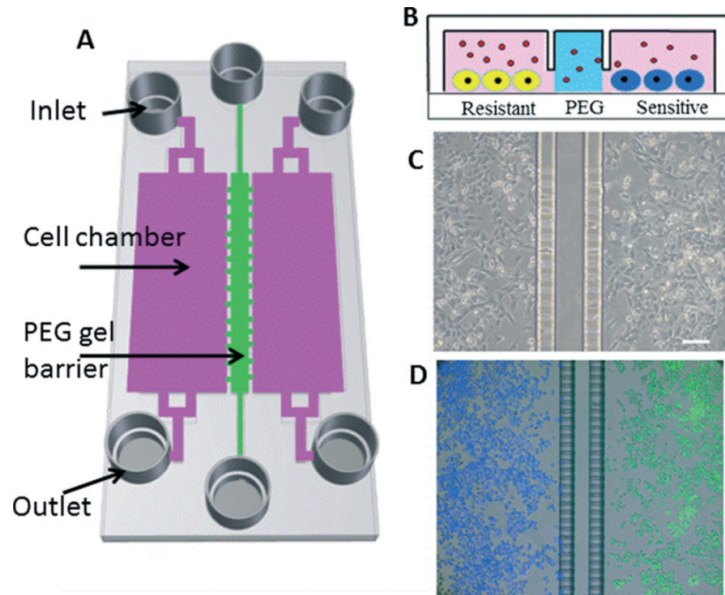


Figure 2.18: Microfluidic co-culture system: compartments separated by PEG hydrogel barrier. (A) schematic representation of the microfluidic device composed by a double layer of PDMS: the bottom layer is composed by $10\ \mu\text{m}$ high grooves that separate the cells culture chambers from the central PEG channel, the top layer comprised 2 chambers $8 \times 1.8 \times 0.075\ \text{mm}$ (*length* \times *width* \times *height*) (in purple) and a central channel $8 \times 0.1 \times 0.075\ \text{mm}$ (*length* \times *width* \times *height*) (in green); (B) cross sectional schematic representation of the device and its working principle whit two types of melanoma cells in close proximity. (C) Brightfield image of two different types of cells cultured after day 1. Scale bar is set at $100\ \mu\text{m}$. (D) Same types of cells of panel B labelled in green and in blue after being seeded in different chambers, image acquired after $48\ \text{h}$. Phenotypically the two cell group are identical except for vemurafenib resistance. Reproduced from [63]; permission conveyed through Copyright Clearance Center, Inc.

The chip (figure 2.18) aimed to study the role of cell cross-talk and paracrine exchange in the context of tumour cells resistance to treatments. The design overcomes some of the issues commonly faced when using transwell systems and conditioned medium co-culture systems, such as the large quantity of medium volume needed, and the consequent high dilution of secreted metabolites.

Furthermore, the central channel with the hydrogel was added to a previous design in which the connection between the two compartments for cell culture was conceived exclusively through microchannels that should have allowed only the diffusion of small metabolites but that could not prevent the passage of highly migratory melanoma cells.

In addition to photo-polymerisation, methods for gel-microfluidics integration include also soft-lithography and flow-solidification techniques. Particularly, this latter overcomes the limitations occurring when sealing hydrogel with other materials, for example features collapsing or the lack of tightness that can cause leaking when inoculating the device [64].

The automatic microturbidostat for bacterial culture built by Xianjia Luo et al. [65] is a device that successfully integrates a hydrogel in a microfluidic platform through flow-solidification. The overall system (shown in panel a of figure 2.19) constituted a two layer PDMS bacterial culture device that includes pneumatic valves and a hydrogel filter (shown in panel b of figure 2.19), an inverted microscope and a PC connected to the valves controllers and a CDC camera. Here, the hydrogel is used to confine bacteria within the chamber. By dividing the nutrient channel from the bacterial culture chamber, the bacteria move from the inlet port to the areas with the highest nutrient concentration and thus settle in the chamber. Critically, the hydrogel prevents bacteria from entering the nutrient channel but allows the nutrients to diffuse from the nutrients channel to the culture chamber.

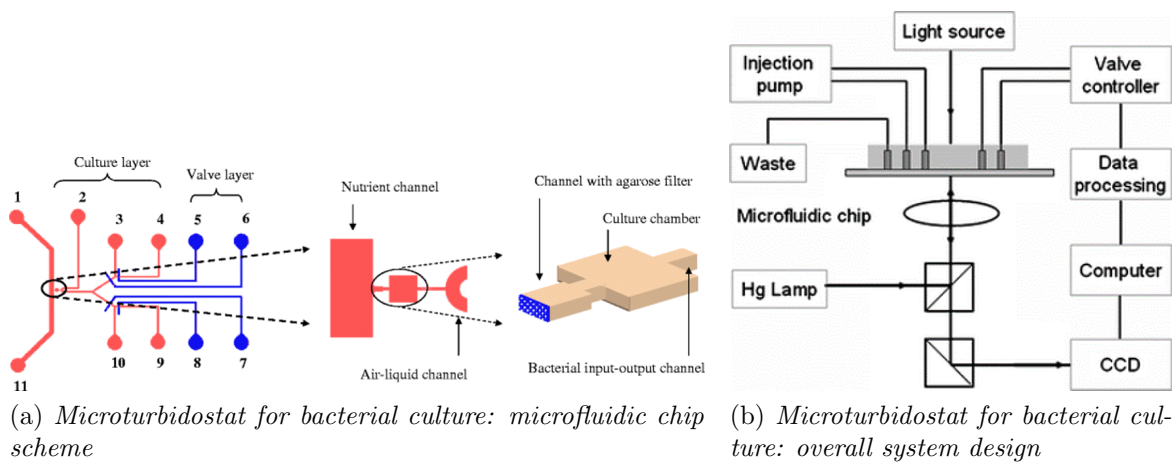


Figure 2.19: Gel integration for microfluidic application: microturbidostat for bacterial culture. Microfluidic chip schematic design (a). Left panel (a):two layer PDMS device. The bottom layer (red) includes the bacteria culturing chamber and the nutrient channel, the top layer (blue) includes the pneumatic valves channels. Central panel (a): zoom on culture chamber left and right connections. Right panel (a): three dimensional structure of the culture chamber and its connections. Overall microturbidostat system design (b): the signal from the fluorescent labelled bacteria in the culture chamber is collected by the CDC camera and analysed by a MATLAB program that give the order to the valve controllers; ultimately the valves control the switch of the input-output bacterial channel. Figures adapted with permission from [65].

The work reported by Xianjia Luo et al. [65] is interesting for the techniques used to integrate the hydrogel filter in the microfluidic chip. To successfully complete such integration, whose main steps are listed below and briefly summarised in figure 2.20, the connection channel between the nutrients channel, through which the gel-solution is inoculated, and the culture chamber must have a specific conformation. Specifically, its width must decrease with a specific ratio to allow the flow resistance to stop the agarose solution. In this specific example [65], the width of this connection channel changes from $50 \mu m$ to $30 \mu m$ and at the chamber entrance it has an aperture of $20 \mu m$. The main steps followed by Xianjia Luo et al. [65] to complete the flow-solidification are the following (see figure 2.20):

1. the PDMS device is left at room temperature for few days to render the surface hydrophobic;
2. the agarose solution at 80°C is inoculated inside the device through the nutrients channel;
3. the agarose solution stops in the middle of the connection channel due to flow resistance;
4. air is injected in the nutrients channel to remove agarose solution;
5. the device is left at room temperature for 10 minutes to allow the hydrogel to solidify;
6. filtered deionised water is inoculated in the device through the nutrient channel to hydrate the hydrogel.

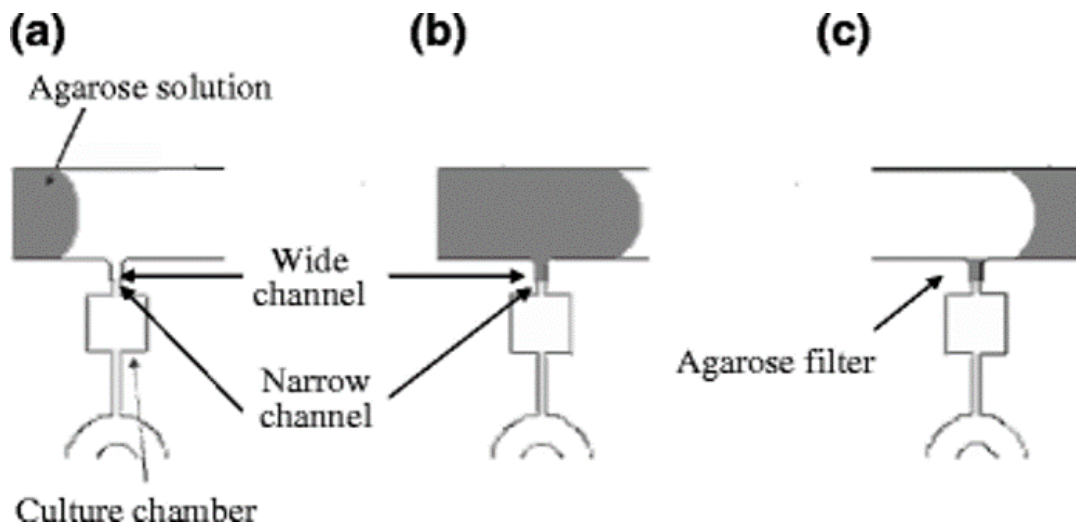


Figure 2.20: Microturbidostat for bacterial culture: agarose flow-solidification. (a) Agarose solution is inoculated at 80°C in the nutrient channel; (b) Agarose solution stops in the part of the connection channel with the intermediate width value ($30\ \mu\text{m}$); (c) Agarose solution is removed from the nutrient channel by air inoculation but it remains in the connection channel where, after cooling down to room temperature, a hydrogel filter is formed. Figure reproduced with permission from [65].

In general, there are numerous examples in the literature of microfluidic devices that use hydrogel barriers to study cancer biology, cancer immunology and cancer therapy [66]. In contrast, this type of microfluidic system for co-culture of bacterial communities is less well developed. Even the example just described [65] does not use a hydrogel as a barrier between two bacterial species. Despite this, it remains an important confirmation of the ability of these gels to allow the diffusion of nano-metric molecules and prevent the passage of microorganisms.

By exploiting the change in flow resistance inside a PDMS device, whose surface is hydrophobic, hydrogels can be integrated in a wide range of microfluidic platforms. Generally, small channels are connected to a wider central channel through which the hydrogel is inoculated in the device. Therefore, thanks to a change in the resistance to the fluid flow, a fish-bone

hydrogel structure (see figure 2.21) is created. In order to strictly confine the hydrogel in such a structure, the parameter to control is the difference between fluid pressure inside the main channel, where the hydrogel is inserted, and that in its branches, where the hydrogel is supposed to stop flowing. The height and the width (w_1 in panel e of figure 2.21) of the main channel, the height and the width (w_2 in panel e of figure 2.21) of the small branches and the surface tension of the hydrogel are therefore critical parameters to tune. Refer to figure 2.21 for an example of the aforementioned type of gel-microfluidics integration. In the device shown in figure 2.21 the gel barrier separates a central cell culture chamber from two lateral sensing channels where bead-based biosensors can be used to detect specific molecules secreted by the cells in the adjacent culture chamber [67]. In the device shown in figure 2.21 the hydrogel, after being confined into the microfluidic platform, has been exposed, together with the entire chip, to UV light in order to be polymerised.

Scientific literature confirms that many hydrogels are not toxic to cells, that nutrients and growth factors can easily diffuse through hydrogels and that, thanks to their optical transparency, it is also possible to observe the diffusion of fluorescent molecules inside the gels. Moreover, hydrogels are relatively easy to obtain, inexpensive and their high malleability makes them adaptable to different designs. As evidence of this last statement, in the microfluidic device shown and briefly described in figure 2.22, a hydrogel is inoculated both inside U-shaped channels and inside straight channels and perform both the function of barrier between different cell cultures and between the nutrient channels and the cell culture chambers themselves [68].

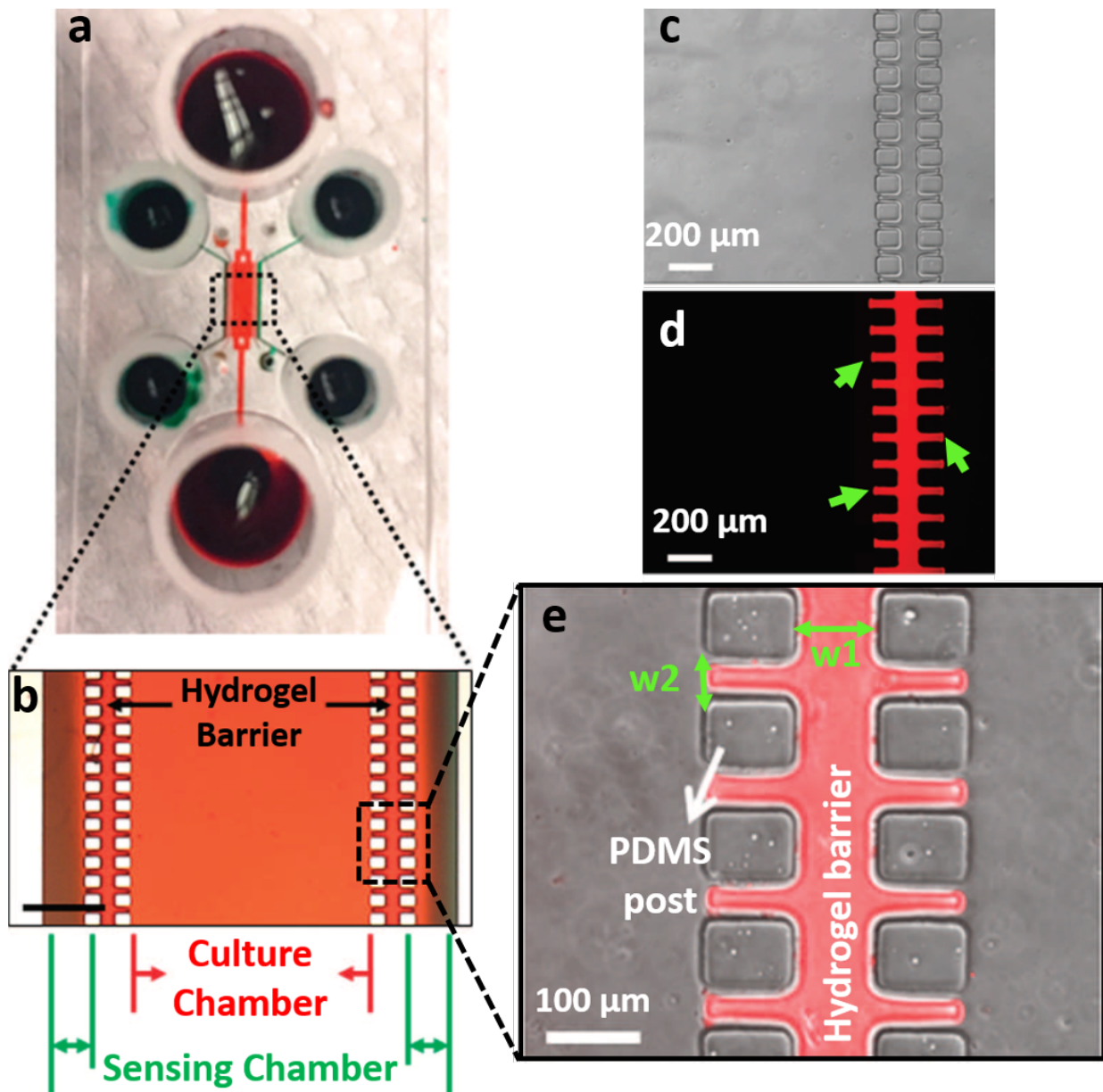


Figure 2.21: Hydrophobic surface to confined gel area: example. Picture of the overall design of the device built by Kyung Jin Son et al. [67]: red area includes the inlet-outlet ports for the cells and the central cell culture chamber, green area includes the sensing channel for the bead-based biosensors (a). Microscopic image of the central part of the device built by Kyung Jin Son et al. [67]. Scale bar = $500\ \mu\text{m}$ (b). Bright field image of the hydrogel barrier (c). Fluorescent image of the hydrogel barrier; green arrows point the hydrogel-air interface (d). Merged bright field and fluorescent image of the hydrogel barrier; w1 and w2 respectively indicate the main channel width and the small branches width: parameters to be tuned to confined the hydrogel exclusively between the chamber and the channel. Figures adapted from [67].

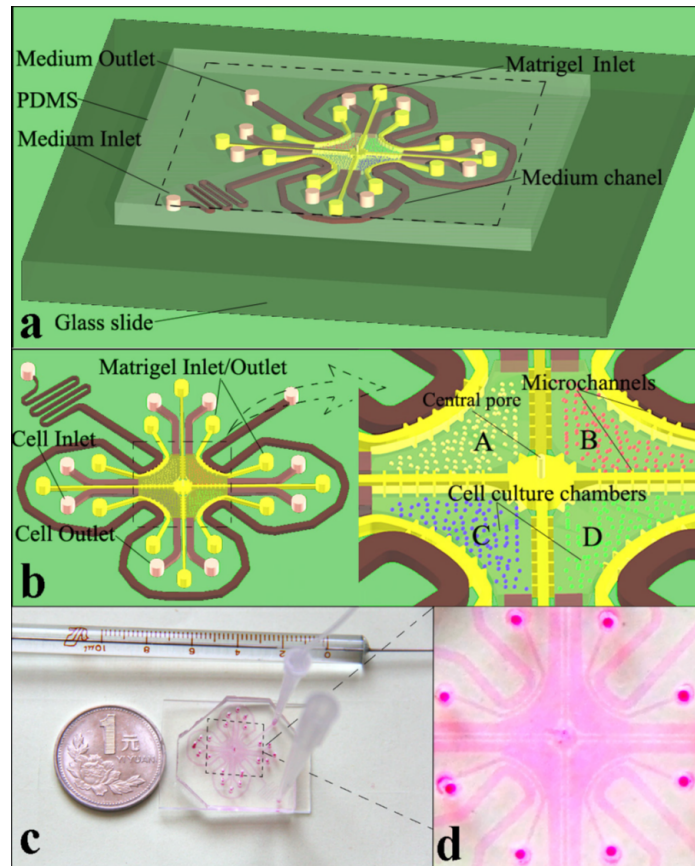


Figure 2.22: Hydrogel malleability: a microfluidic co-culture device to simulate bladder cancer micro-environment. Overall schematic design of the device (a). Magnification of the central area of the device: the external medium channel supplies nutrients to the four cell chambers (A,B,C,D), each chamber has its inlet and outlet port to inoculate the cells, yellow U-shape structure and central cross indicates the areas filled with the hydrogel. The structures filled with gel permit the diffusion of small molecule between different compartments of the device thanks to a set of micro-channels (b). Microfluidic device connected to the perfusion equipment (c). Microscopic image of the device filled with food colouring (d). Figures reported from [67].

Compartments separated by membrane

The term *membrane* can be interchanged with *semi-permeable barrier* and this definition immediately clarifies their function. A membrane is generally positioned between two homogeneous phases allowing the diffusion of specific molecules or particles between them. This passage is generally driven by some kind of force such as concentration gradient, pressure difference, changes in temperature, electric force and so on [69]. Depending on their morphology, membranes can be divided in two different types:

- dense membranes;
- porous membranes.

The main difference between the two groups is the size of the molecules that they are intended to separate. The first group potentially includes all dense materials when they are used to separate small molecules (e.g. ions). Such molecules are so small that they can pass

through the material itself. Thus, as highlighted in the review written by J. de Jong, RGH Lammertink and M. Wessling [70], all materials can act as membranes, but what often makes them unusable for this purpose is their low permeability or selectivity. On the other side, when using porous membranes, mass diffusion between the opposite sides of a membrane happens through openings in the structure called *pores* through which bigger and complex molecules (e.g. signalling molecules exchanged between bacterial cells) can pass. For the purpose of this literature review, each time reference is made to a *membrane*, unless otherwise specified, it is meant a *porous membrane*.

The entire previous section (section 2.2.2) has been dedicated to a specific type of membranes of particular interest for the completing of the current work: hydrogel membranes.

When integrated in microfluidic platform, membranes are mainly used for chemical reagents detection, gas detection, cell culture, drug screening and the design of microreactors. Despite their widespread use, especially for chemical and biological applications, their integration with microfluidic devices still presents some difficulties. A membrane can either be purchased individually and subsequently integrated into a microfluidic platform, it can be fabricated during the general manufacturing process of the device, it can be prepared in situ or the whole chip, depending on the material it is made of, can work as a membrane. For example, one can think of PDMS as being a dense membrane that allows the diffusion of oxygen into microfluidic devices.

If the membrane serves as a barrier in a device for the co-culture of different bacterial species, it should ideally allow the diffusion of nano-metric molecules and prevent the passage of micro-metric bacteria, therefore the diameter of the pores must be in the order of hundreds of nanometres. This dimensional range complicates the fabrication of the membrane itself and requires expensive lithography instrumentation. Therefore, commercially available membranes, already tested and functioning, can be purchased. In the literature, porous polymers are frequently reported as components of membranes used for mass transport.

When the specific design requires two or more compartments separated by a semi-permeable membrane, the most common way to manufacture the microfluidic platform is to stratify and separate several layers of PDMS with a membrane. Figure 2.23 shows a scheme of a typical stratified PDMS device with two compartments for bacteria culture separated by a semipermeable membrane. This design, typical not only for co-culture devices but also for organ on chips, requires:

- precise alignment of PDMS layers;
- reliable bonding between layers i.e. different membrane materials, PDMS and glass parts of the device.

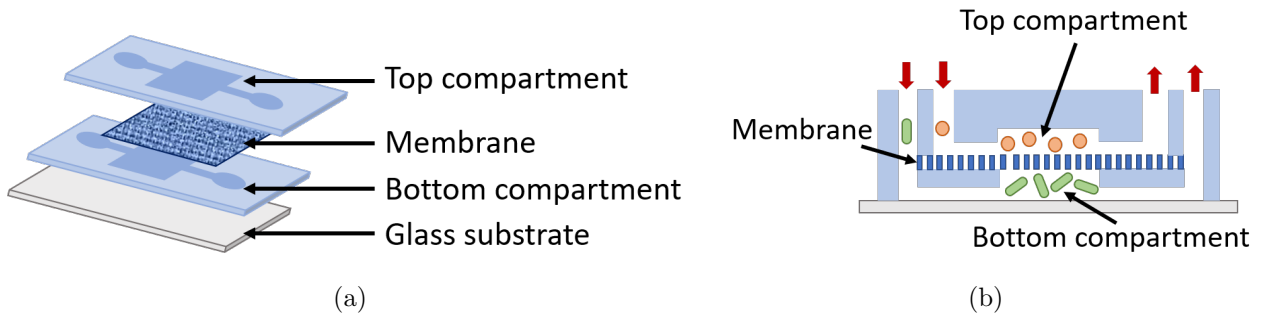


Figure 2.23: Bacterial culture microfluidic chambers separated by membrane: design. Schematic (a) and cross-sectional schematic (b) illustration of a two layers device for bacterial co-culture: two culturing chambers are separated by a semi-permeable membrane. In panel b spatial arrangement of the bacteria in the device is also shown and red arrows indicate the inlet and outlet ports of the device.

A microfluidic device that allows growth of different bacterial species with communication through the exchange of molecules through a semi-permeable membrane, has been demonstrated by a design such of that of Hyun Jung Kim e al. [41]. Here, a single upper PDMS layer containing isolated culture wells is separated from a bottom channel by a polycarbonate membrane allowing chemical communication. The overall design and working principles are briefly illustrated in figure 2.24.

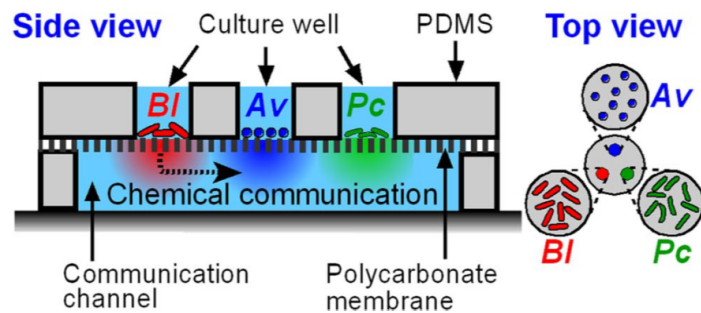
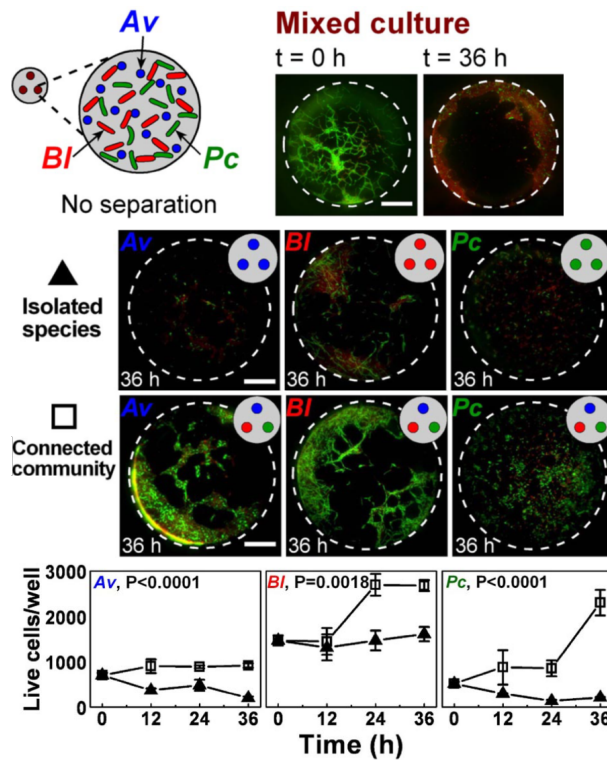
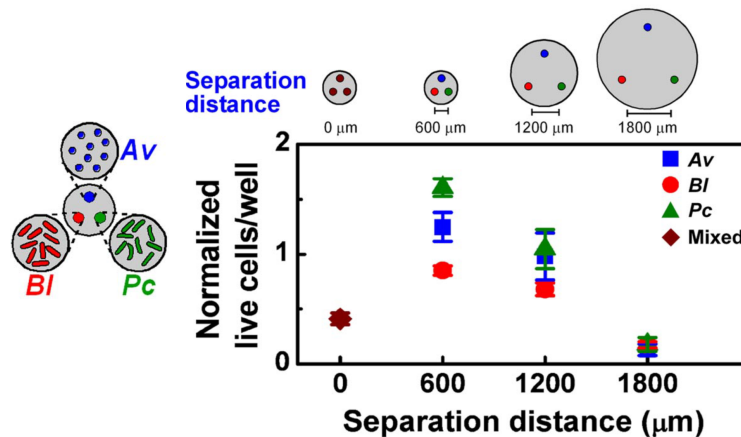


Figure 2.24: Microfluidic compartments separated by membrane: synthetic community of three bacteria species. Cross sectional view of the device designed by Hyun Jung Kim e al. [41]. In the device three wild-type soil bacterial species are co-cultured: *Bacillus licheniformis* (BI), *Azotobacter vinelandii* (Av) and *Paenibacillus curdlanolyticus* (Pc). The micro-environment is maintained stable by imposing spatial structure: three culture wells in the top layer and a chemical communication channel in the bottom layer. Figure reported from [41].

In the device (figure 2.24) three soil bacteria species, between which there is no evidence of reciprocal interaction in nature, are forced to grow in close proximity but without physical contact [41]. The results, in terms of living bacteria after culture, are summarised in figure 2.25.



(a) Synthetic community with and without communication among the species



(b) Synthetic community at different degree of separation

Figure 2.25: Microfluidic compartments separated by a membrane for the study of a synthetic community of three bacteria species: results. Panel (a). Living bacteria are marked in green and dead bacteria are marked in red. Top line shows that no living bacteria are detected after 36 hours when the three species are grown in a mixed culture. Second, third and bottom line compare results in term of living cells after a 36 hours cultivation inside the device in condition of single isolated species (same species in all the wells) and of connected community (different species in different wells). Both experiments are conducted in condition of poor nutrient medium and under antibiotic pressure. Scale bars are at $50 \mu\text{m}$. Graphs compare the number of live bacteria over time in devices containing all three species: isolated species (closed triangles) and connected community (closed triangles). As visible from the graphs only when the three species are let communicate through molecules diffusion bacterial populations in individual wells do not decrease. Panel (b) shows that when cultivated as a connected community, populations growth over time is visible only for specific values of distance between culturing wells. Figures adapted from [41].

The experiment demonstrated that only when all the three species are cultured together, the population (number of living cells) of each species grows continuously over 36 hours in low nutrient medium conditions and under antibiotic pressure. These experimental results were used subsequently to build a mathematical model linking the degree of separation between the wells and bacterial proliferation in the device.

The most common application of membrane based microfluidic culture systems are those used for the design of organ on chip devices that aim to simulate the function of the basal membrane. Figure 2.26 shows the chip built by Jacquelyn A. Brown et al. [71] that reproduces the complex structure of the Blood Brain Barrier; the structure that drives the exchange of nutrients between capillaries and the brain.

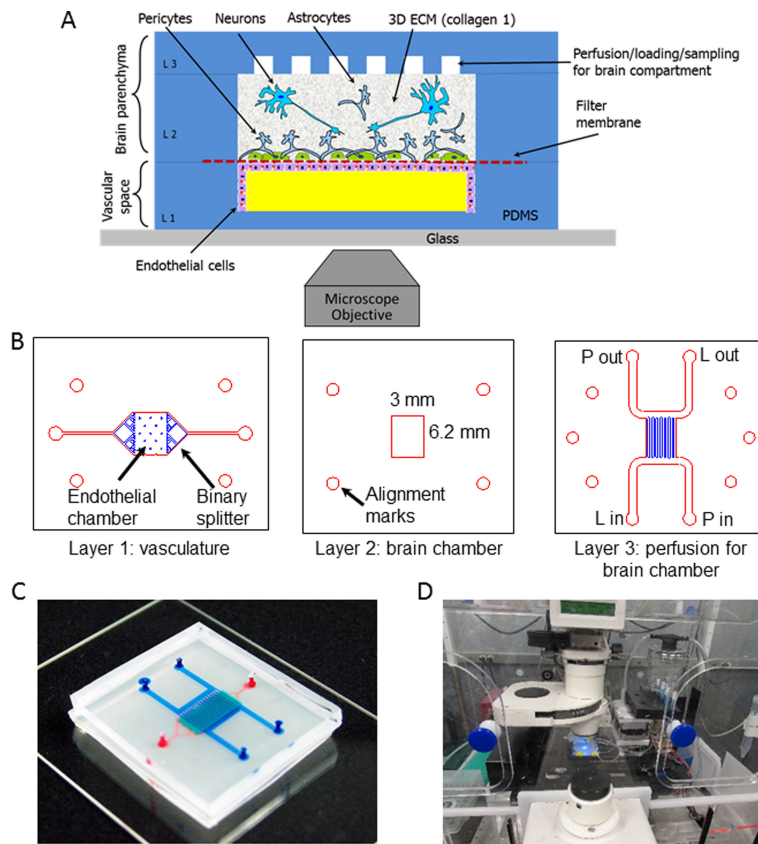


Figure 2.26: Microfluidic compartments separated by a membrane: recreating blood-brain barrier physiology. A: schematic view of the device and cell disposition in the chip. Bottom layer recreates the vascular lumen (vascular space) and its endothelial tissue, middle layer simulates the brain compartment: astrocytes and pericytes directly on the other side of the filter membrane and neurons in the upper part. (B) three photolithography masks used for the device fabrication. (C) Real picture of the assembled device. (D) Chip and its perfusion system on an incubated microscope stage. Reprinted from [71], with the permission of AIP Publishing.

In general, the design of the chips reflects that shown in panel a of figure 2.23, the principal challenge in the fabrication process is the method used to integrate the membrane, a step widely discussed by the scientific community [72], [73]. The lack of a standard protocol

means that there is a real chance of failure with any of the techniques known today. For example, plasma oxidation and thermal bonding may leave small cracks upon integration that can cause leaks through the membrane while the use of PDMS prepolymer layer to glue the membrane into the device can cause the erroneous occlusion of features. Any changes made to the most common procedures in order to improve their performance can be taken into account depending on the application of the final device but, overall, they add steps to the manufacturing process.

As a common rule, we try to avoid complicating the fabrication of the device, for this reason the use of a membrane has not been taken into consideration in constructing the device which is the object of the current work. With the ultimate goal of sensing specific secondary metabolites, known to be exchanged between the bacterial species making up the community to be studied (see previous chapter 1), the difficulty of integrating any type of sensor to detect the passage of molecules through a membrane that is no more than a few tens of micrometers thick makes culture systems based on hydrogel barriers (section 2.2.2) or on connection via nano-slits (section 2.2.2) more appropriate for this study.

2.3 Conclusions

During the current century, the massive presence of microorganisms on our planet and inside our body has been fully confirmed. Starting from this discovery microbiologists could prove that microbes occupy their habitats maintaining a high population density thus constituting communities in which different species interact with each other.

Studying and decoding such interactions is important not only to fully harvest the potential enclosed in the microbial world but also to better understand the evolution of many dangerous infections known to be poly-microbial. This can lead, in the end, to the synthesis of new effective drugs capable of overcoming major shortcomings of today's common treatments. First of all antibiotic resistance, a major issue, for example, in the treatment of poly-microbial infections of cystic fibrosis patient lungs.

When studying microbes you are forced to deal with a micro-metre dimensional range, difficult to directly access with traditional bacterial culture protocols followed in laboratories. Particularly, if observing different species at the same time, a stable coexistence and a defined micro-spatial control are needed. The birth of microfluidics has responded to these needs. This discipline, by definition, operates with micro, nano or even pico-litre volumes of liquids, suitable for the observation of individual bacteria.

While microbiology has been strongly revolutionised by the use of PDMS microfluidic devices for bacteria culturing, the scientific literature lacks examples of co-culture microfluidic systems for the study of bacteria. In terms of microfluidic platforms for microbial culturing, PDMS-based monolayer growth chambers allow control of the micro-environment with a single-cell resolution keeping an appropriate fluid dynamics. To convert the aforementioned

growth chamber into a co-culture microfluidic system, other identical culturing modules can be added to the overall design. Each module can host a different bacterial species composing the community under investigation. According to the degree of contact required between different species, culture chamber modules can be separated through a nano-slit, a block of hydrogel or a semipermeable porous membrane. All these technologies permit the exchange of metabolites between bacterial species but prevent physical contact.

Table 2.1 briefly compares these approaches. As already mentioned, porous semipermeable membranes have not be considered as possible barriers between the microfluidic culture compartments for our application. This choice is mainly due to the complexity of their integration in microfluidic devices. In fact, from a first analysis, given the fabrication techniques used, described in the next chapter, the construction of nano-channels and above all the use of hydrogels has been evaluated more appropriate techniques.

Microfluidic co-culture system	Pros	Cons
Compartments separated by nano-slits	<ul style="list-style-type: none"> • Small molecules diffusion; • no additional fabrication steps; • easy to design; • no additional materials; • easy sensors integration; • no toxic for cells. 	<ul style="list-style-type: none"> • sub-micron features; • high-resolution fabrication; • high fluid flow resistance; • bacteria can swim trough nano-openings.
Compartments separated by hydrogels	<ul style="list-style-type: none"> • Small molecules diffusion; • gel optical clearness; • malleable gel integration; • precise gel integration; • easy <i>in-situ</i> polymerisation; • relatively inexpensive; • possible gel functionalization; • easy sensors integration; • no toxic for cells. 	<ul style="list-style-type: none"> • gel polymerisation; • diffusion assessment often needed beforehand; • rare use for bacterial co-culture; • cells may get trapped.
Compartments separated by membranes	<ul style="list-style-type: none"> • Small molecules diffusion; • relatively inexpensive; • commercial membranes variety; • possible membrane functionalization. 	<ul style="list-style-type: none"> • complex "<i>in situ</i>" fabrication methods; • complex integration of commercial membranes; • complex integration of sensors.

Table 2.1: List of advantages and disadvantages of different microfluidic co-culture systems. With *membranes* we intend *porous membrane*.

Chapter 3

Materials and methods

This chapter describes the protocol followed to build the microfluidic platform for the co-culture of two physically separated bacterial species. As already mentioned in chapter 1, the final outcome, in terms of fully completed devices, is a module for single bacterial species culture. To obtain a chip that meets our requirements, several designs were tried. For each attempt, referred to as “*strategy*”, fabrication steps are described below along with optimised parameters. I note, optimisation of these parameters is described in chapter 4. To fabricate a single device, a silicon substrate covered with micro-metre scale photoresist features, defined with a Direct Laser Writing (DLW) lithography process served as the mould for PDMS casting. After the casting step, the PDMS is cured at 60 °C over the mould in a plastic Petri dish overnight. Once cured, the PDMS block is cut and bonded to a glass slide to enclose the imprinted design. The final microfluidic device looks like the bottom panel in figure 3.1.

Figure 3.1 visually summarises the fabrication process which can be divided in two main parts:

1. **Mould preparation** (substrate preparation, spin-coating, exposure, development in figure 3.1);
2. **PDMS replication moulding** (PDMS pouring, PDMS peeling-off, PDMS cutting, PDMS-glass bonding in figure 3.1).

The next section gives an overview of the process followed to fabricate a sealed microfluidic device made of PDMS that incorporates microstructures.

Since most of the optimisation was focussed on the first part of the fabrication procedure and especially the “exposure step”, before proceeding with the technical details, strategy by strategy the exposure technique applied is described.

The final sections of the chapter are dedicated to the preparation of the bacterial culture and the experimental setup.

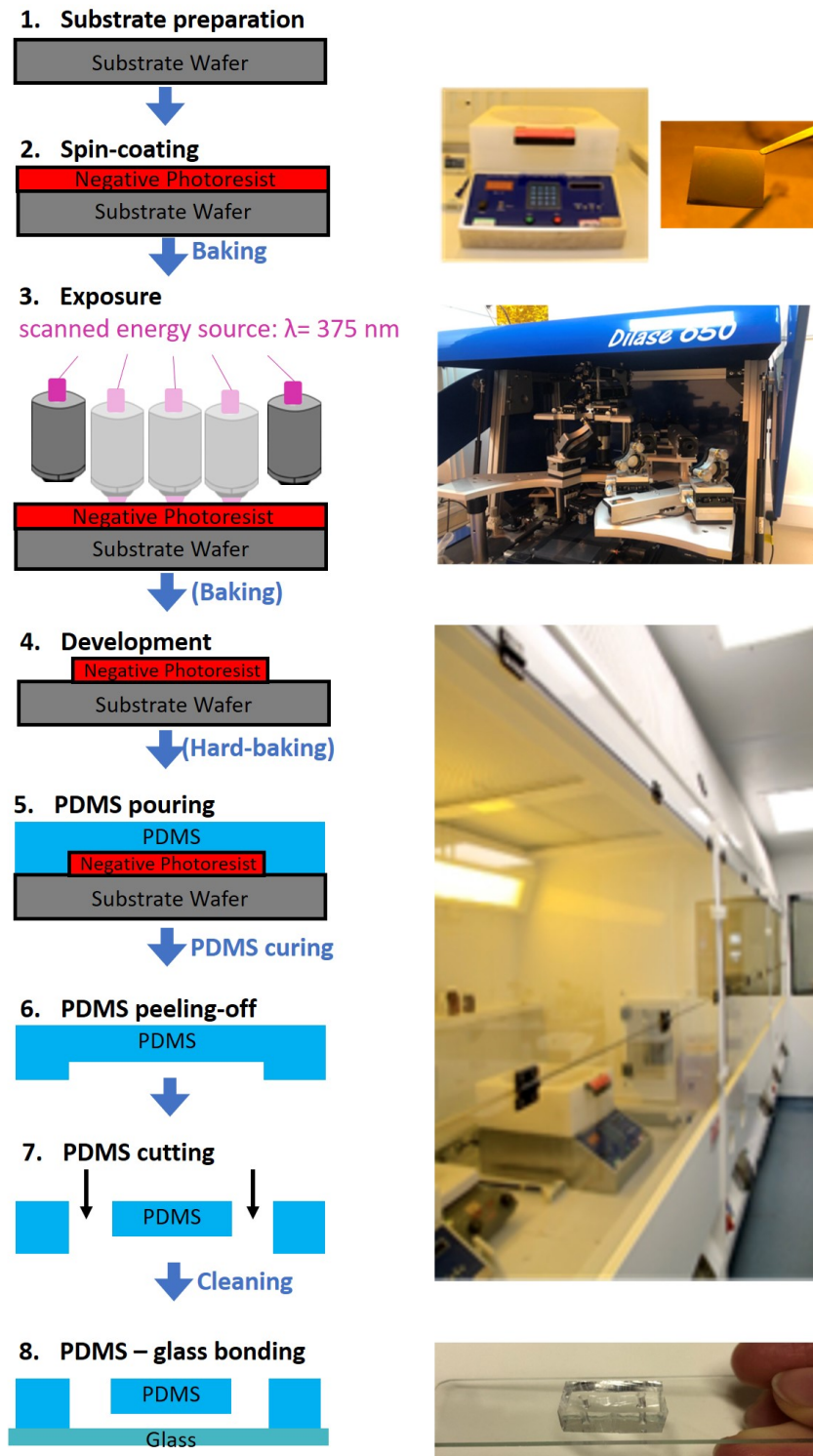


Figure 3.1: PDMS device fabrication: flow chart. The process starts from a silicon substrate (top left) and ends with the complete final device in PDMS (bottom left). The flow chart refers to a fabrication protocol that uses a negative photoresist and DLW lithography as exposure technique. Steps in brackets are not always required and my protocol only includes them with one of the two photoresist used. The Right column: real pictures of the spinning coater and a coated Si wafer, DLW system used for the exposure, clean room environment where the main fabrication steps are carried out and a final assembled device.

3.1 Fabrication of a sealed microfluidic PDMS device

The first big part of the fabrication process is the fabrication of a master containing the features to be reproduced in the final PDMS device. As master I used a flat silicon surface covered with patterned negative photoresist.

A photoresist is a light-sensitive material that can be degraded (*positive photoresist*) or strengthened (*negative photoresist*) when exposed to light in a specific range of wavelengths. Such range varies according to the photoresist used. Upon the exposure, the desired features are obtained by applying a solvent (*developer*) on the surface. In the case of *negative photoresists*, the *developer* dissolves the not-exposed, thus not-strengthened, regions, while in the case of *positive photoresists*, it dissolves the exposed, thus degraded, regions. I used two different negative-tone photoresists: K-CL (KLOE SA) that is photosensitive for wavelengths between 325 nm and 405 nm and SU-8 (MicroChem Corp.) whose photosensitive is maximum for a 365 nm wavelength.

K-CL photoresists are resins obtained by sol-gel processing from organo-mineral precursors. Their organic network gives them photosensitive properties while the mineral network improves their mechanical and thermal properties. After the first attempts to fabricate a mould made of K-CL, having encountered issues in its adhesion to the silicon substrate (see section 4.1.1), I changed photoresist, opting for a mould made of SU-8 whose use for microfluidic applications is widely documented.

SU-8 photoresists are obtained by dissolving A Novolac epoxy in an organic solvent, commonly gamma-butyrolactone or cyclopentanone, with the addition of a specific photo-initiator that, when exposed to UV light, triggers the formation of an acid that protonates some epoxy rings, causing their opening. Upon a post exposure baking (PEB) that sufficiently heats the photoresist, the protonated epoxy rings react with the neutral ones and thus start the cross-linking process which makes the exposed regions less soluble when treated with the developer. The PEB (marked between step 3 and step 4 in figure 3.1) is not required with K-CL photoresists since their cross-linking is completed at room temperature.

Both K-CL and SU-8 photoresists are composed by an organic solvent dissolving an epoxy resin and their solvent content is a fundamental parameter to tune the thickness of the final photoresist layer. Aiming to build a microfluidic device suitable for a bacterial monolayer culture, the thickness of the photoresist layer must be controlled to assure it is thinner than $1\ \mu\text{m}$. As indicated at step 2 of figure 3.1, the photoresist is deposited by spin coating: a drop of photoresist is applied with a 1 ml syringe at the centre of the silicon substrate that is then rotated in the spin coater at specific speed. Therefore, the photoresist is spread thanks to centrifugal force. The final thickness of the photoresist layer is related to:

1. the spinning speed;
2. the viscosity of the photoresist.

Overall, the photoresist layer is thinner for higher spinning speeds and lower viscosities that are in turn proportional to the solvent content of the mixture of the photoresist. K-CL 010 is the less viscous K-CL available for sale. With K-CL 010 a layer down to $2\ \mu\text{m}$ thick can be fabricated for spinning speeds higher than $2500\ \text{rpm}$. Lower viscosities can be achieved further diluting the mixture with ethanol (ETH). Also SU-8 photoresists are available for sale at different degrees of viscosity. SU-8 2050 and SU-8 2000.5 were respectively the most and the least viscosity mixtures available in the lab but intermediate viscosities were achieved by mixing.

With both photoresists, for a successful exposure, it is crucial to evaporate most of the solvent content right after the spin-coating step (soft baking step marked between step 2 and 3 in figure 3.1) and, to be sure to remove extra solvent pockets, a final optional hard-baking step can be added after the development. The hard-baking ensures total cross-linking, improves resist adhesion with the silicon surface and increases the thermal, chemical and physical stability of the structures.

After the hard-baking step, the mould is ready so the PDMS mixture can be prepared to start the second big part of the fabrication protocol: the PDMS replica moulding. PDMS is a silicon-based organic polymer that thanks to its biocompatibility, permeability to oxygen, low cost, mechanical and optical proprieties is widely used for the prototyping of microfluidic devices. Furthermore, PDMS is relatively easy to fabricate. Liquid PDMS prepolymer is mixed with a curing agent whose percentage in the mixture can be varied to tuned the mechanical properties of the final PDMS layer. Overall, the stiffness of the PDMS device increases with higher percentages of curing agent.

The liquid PDMS mixture is poured onto the mould and then cured at 60°C overnight. Once solidified, the PDMS is peeled off from the mould (step 6 in figure 3.1) and inlet/outlet ports are punched through the polymer block. The PDMS device can now be sealed to an appropriate substrate such as a cleaned glass slide.

A strong permanent bonding between the PDMS layer and the glass slide can be achieved by plasma bonding. Treating PDMS surface with an oxygen plasma causes its oxidation by generating silanol terminations that, upon contact with the glass surface and with the application of a light pressure, enable the formation of irreversible covalent bonds between oxygen and silicon.

3.2 Experimental techniques: Direct Laser Writing

When performing lithography by DLW, a collimated then focussed laser beam at a specific wavelength is directed by a set of lenses and mirrors towards a substrate coated with a negative-tone or positive-tone photoresist. The laser beam is appropriately corrected through a sequence of wave-plate, polariser and beam splitter. At the end, a quarter-wave plate is placed before an objective lens with high numerical aperture. Focusing the beam using such

objective lens, the intensity at the focal plane can reach values up to a few orders of magnitude higher than the nominal laser beam power at that point. If the focal plane is located inside the photoresist layer, this high intensity causes chemical changes in a small volume confined by an iso-intensity level where a chemical threshold for a photo-polymerisation reaction is exceeded. During the polymerisation process, monomers are linked together to form long polymer chains that are then in turn linked with each other to form macro structures. Hence, the wavelength of the laser source must be compatible with the processing wavelength range of the photoresist. After positioning the focal plane at an appropriate depth inside the photoresist, an exposure by DLW consists of the movement of the stage holding the sample. Here, the sample position is scanned in respect to the focusing spot while the laser turns on and off and remains immobile. The desired pattern is therefore imprinted in the photoresist. Figure 3.2 shows a schematic representation of the lithography writing process carried out via DLW.

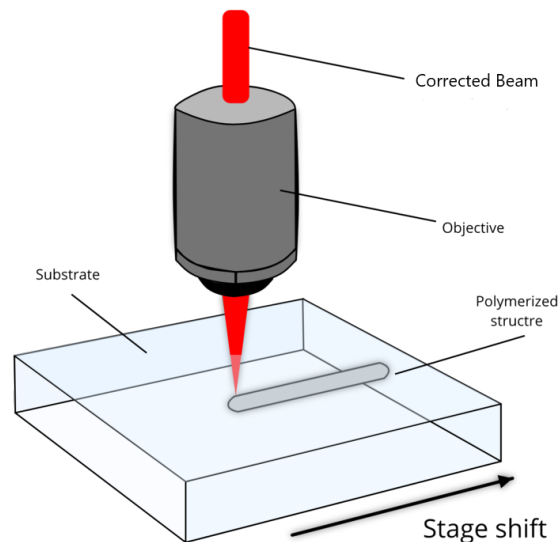


Figure 3.2: Lithography process by DLW. Schematic of the lithography writing process carried out by DLW. Detail of the laser beam focusing inside the sample after being corrected and collimated by optic components along the path. Figure adapted from [74].

For the fabrication process described in the current work, the all-in-one equipment used to perform DLW lithography is the *Dilase 650* system by KLOE SA. The overall system and its main components are represented in figure 3.3. Table 3.1 summarizes the characteristic of the lithography setup components.

In addition to the physical equipment, the system is provided with two integrated software: *KloeDesign* to draw or import the design file and *DilaseSoft* that directly communicates with the *Dilase 650* equipment. For the experiments described in chapter 4 the models for the exposures were all created using *KloeDesign*. Refer to appendix A for more details on the overall *Dilase 650* system for DLW lithography.

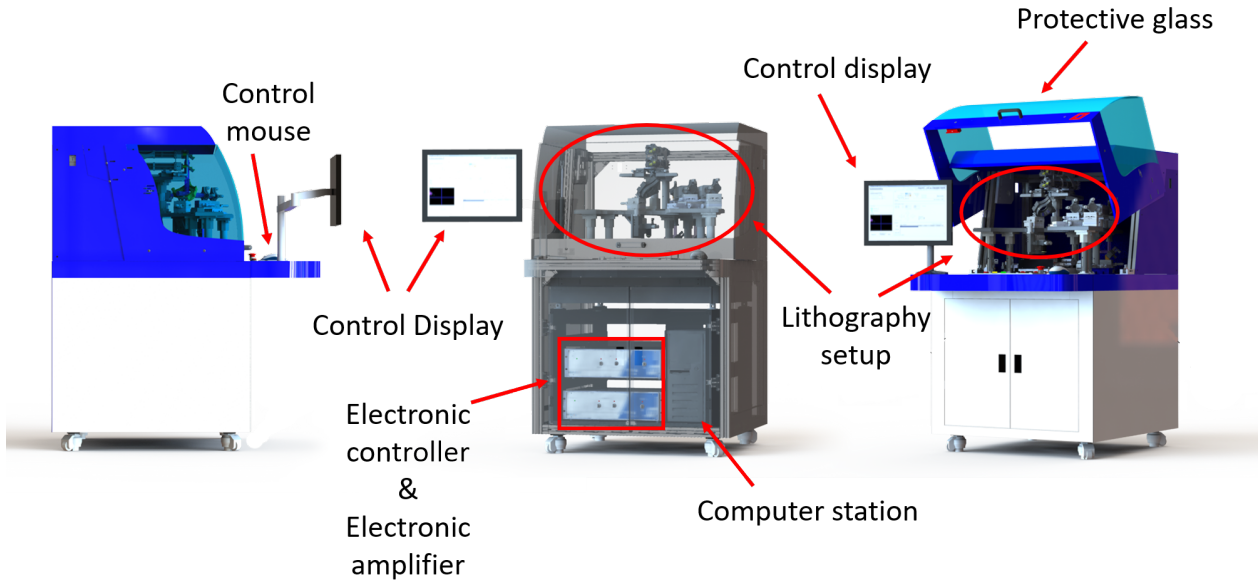


Figure 3.3: Overall Dilase 650 system for DLW. The system is shown as it appears to the user. Cover elements are visible in all the panels from left to right: protective metallic cover boxes and glasses, control display, mouse and keyboard connected to the computer station. Electronic controller and amplifier are visible in the central panel. Lithography setup is indicated in the central and right panel. Figure adapted from [75].

Motorised Stage	
Travel range	100 mm × 100 mm to 150 mm × 150 mm
Type	Linear motor
Maximum writing speed	500 mm/s
2 UV laser sources	
Type	Diode laser
Laser wavelength	375 nm
Nominal power	70 mW
Laser optical line 1 - 0.5 μm optical tube	
Laser spot size after focusing	0.5 μm to 2 μm (±250nm)
Laser optical line 2 - 10 μm optical tube	
Laser spot size after focusing	10 μm to 100 μm (±250 nm)

Table 3.1: Dilase-650 specifications.

3.2.1 Focusing height and dynamic lithography parameters

Each “*.LWO” file imported to the *DilaseSoft* software requires the user to indicate three parameters for the exposure (see figure A.3 in appendix A). The tuning of these parameters and their optimisation is fundamental to have a satisfactory match between the designed pattern and its realisation in the photoresist.

The parameters are:

1. **dynamic lithography parameters** including **writing speed** and **laser power** (referred to as “modulation” in the *DilaseSoft* interface) whose optimisation is important to avoid to over or under exposure of the photoresist. Refer to table 3.2 for a brief physical description of the lithography parameters;
2. **focusing height** whose optimisation is important to obtain the smallest possible laser width and the best quality of pattern transfer. At the optimum focusing height, the photoresist layer is imprinted by parallel laser beam rays so the pattern resulting is straight and the nominal size correspond to an actual optical line. Refer to table 3.2 and figure 3.5 for a brief physical description.

DLW: over-exposure and under-exposure

The combination of the values of writing speed and laser power is critical to evaluate the total *dose* of UV radiation incident on the photoresist when exposed by DLW lithography. Specifically, *dose* is the product of UV light intensity (laser power per unit area) and exposure time (time taken to expose a certain photoresist area at a certain writing speed). The dose of radiation required for the correct transfer of the designed pattern varies according to the photoresist composition and the thickness of its layer on top of the substrate. Overall, without changing the photoresist, the dose required for a correct exposure is higher for thicker photoresist layers. The physics of the exposure can also affect the realisation of the pattern. For example, changes in the lithography setup or in the optical properties of the substrate underneath the photoresist may alter the actual dose received by the photoresist. With an highly reflective substrate the total dose received by the photoresist is generally higher compare to the dose received with the same lithography setting, by the same thickness of the same photoresist lying on an absorptive substrate. In fact, in the first case, the photoresist may also be exposed by additional reflected radiation. Generally the regions that are particularly altered when exposed to non-finely optimized doses are the edges of the pattern. In fact, when the dose is too high (over-exposure), light scattered and diffracted in the photoresist layer may be enough to expose the side of the edge that in the original pattern is supposed to remain “dark”. In negative photoresists, the cross-linking process may be triggered in regions that should be dissolved after development, resulting in structures larger than desired and a loss of sharpness of corners thus preventing the realization of small features (see figure 3.4). Instead, if a negative photoresist is severely under-exposed the cross-linking may not be trigger at all and the pattern may not be transferred or, in less severe cases, structures may result thinner than desired (see figure 3.4). Frequently, with negative photoresists, under-exposed small features are so thin and mechanically unstable that, before the hard-baking step, they can be partially moved (example in figure 3.4). From strategy to strategy, the optimization of the radiation dose was carried out by varying the lithography parameters (writing speed and laser power), adjusted, from time to time, after confronting the exposed pattern, observed under the optical microscope, with the designed one.

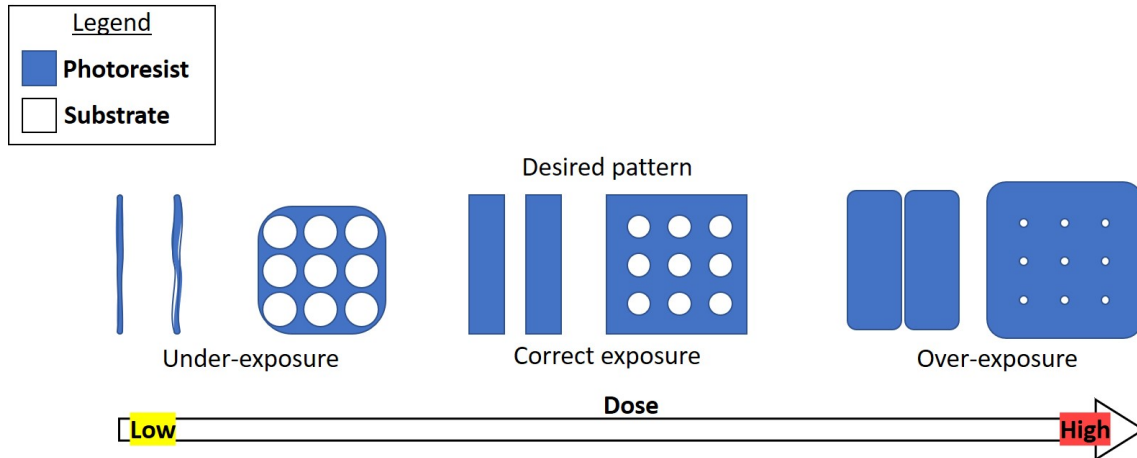


Figure 3.4: Over and under-exposure of negative photoresist. Comparison between lithography exposures of the same pattern in a negative photoresist at different radiation doses. The three schematic representations show how features appear on the photoresist after development. Only the central representation reproduces correctly the desired pattern so the associated exposure is marked as “correct”. When the pattern is exposed with doses of radiation lower than that associated with the “correct exposure”, it appears as in the left representation; when the pattern is exposed with doses of radiation higher than that associated with the “correct exposure”, it appears as in the right representation.

Variable	Physical significance	Given as	Range for laser stability	Very low value	Very high value
Modulation	beam power at focusing lens output directly proportional to radiation dose	percentage of total power (100% = 70 mW)	close to 50%	underexposure	overexposure
Speed	writing speed inversely proportional to radiation dose	stage speed [mm/s]	lowest values	<ul style="list-style-type: none"> overexposure; long exposure. 	underexposure
Focusing height	distance focusing head - sample plane	focusing head z coordinate z=0: maximum distance [mm]	NA	<ul style="list-style-type: none"> focus below sample plane; converging beam hitting the sample; bad quality. 	<ul style="list-style-type: none"> focus above sample plane; diverging beam hitting the sample; bad quality.

Table 3.2: Dynamic lithography parameters and focusing height description. Their optimisation is a key step for the success of the exposure.

Protocol to optimise the focusing height

The *focusing height* (figure 3.5) must be optimised for every substrate using a standard protocol that includes writing an array of identical files while varying the dynamic lithography settings.

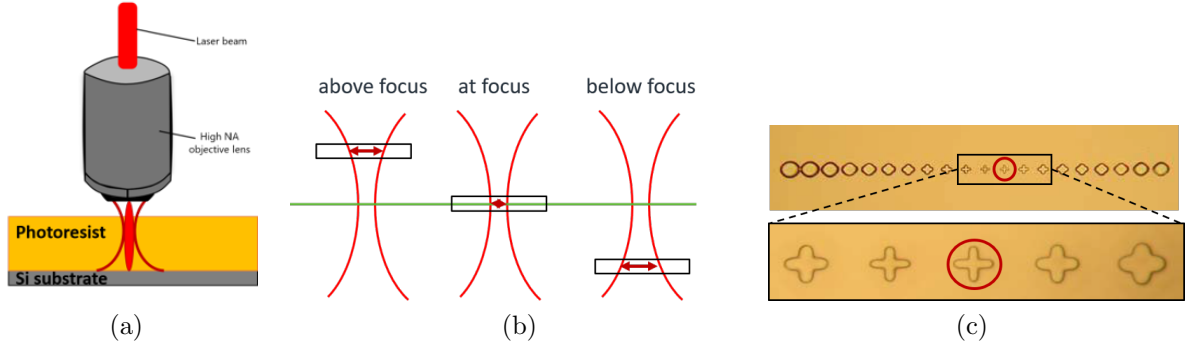


Figure 3.5: Focusing height optimisation. Schematic representation of a DLW beam correctly focused inside the photoresist (a). Focusing height smaller than the optimal: laser beam is propagated with convergent rays through the photoresist, the imprinted pattern is wider than the nominal one and it is not straight (left of panel (b)). Focusing height bigger than the optimal: laser beam is propagated with divergent rays through the photoresist, the imprinted pattern is wider than the nominal one and it is not straight (right of panel (b)). At the optimal focus height laser beam is propagated with parallel rays: the imprinted pattern is straight and its size correspond to the nominal one (middle of panel (b)). Example of microscope observation of a DLW test for focusing height optimisation: same pattern is exposed at fixed power and writing speed while the z coordinate of the focusing head is varied. Only the pattern in the red circle is well focused and correctly reproduces the cross design (c). Panel (c) adapted from [76].

As long as the lithography dynamic settings (laser power and writing speed) does not change, and unless the lithography setup is substantially modified, the optimisation protocol remains valid and should not need to be repeated, so even the optimal focusing height should not vary. After loading the sample, the *display system* (see figure A.1 in appendix A) and the visualisation panel in the *DilaseSoft* user interface (see figure A.3 in appendix A) are used to focus the objective lens on top of the photoresist. When a satisfactory focus is reached, the z coordinate of the focusing head in this condition is noted. So the optimisation protocol starts from this value that at each exposure it is modified by a value indicated as Δz until the imprinted pattern best reproduce the design one. Once the optimised height is found, all the exposures with the same conditions can be completed inserting as “focusing head z coordinate” (see figure A.3 in appendix A) a value corresponding to:

$$z_{focusingHead} = z_{topPhotoresist} + \Delta z_{optimised}$$

In the previous equation, the value $z_{topPhotoresist}$, that corresponds to the z coordinate at which the focusing head provides the best focus the objective lens on top of the photoresist, must be found for each new exposure but generally it should not change substantially, while the value $\Delta z_{optimised}$ once optimised is left unchanged for exposures with the same conditions (same photoresist, laser power and writing speed). Panel (c) in figure 3.5 shows a microscopic representation of a Δz optimisation test.

In the following sections the optimised Δz has been indicated for each strategy.

3.3 Mould preparation

The photoresist used here were the K-CL 010 by KLOE SA, SU-8 2000.5 from MicroChem Corp. and SU-8 2050 by MicroChem Corp. Both K-CL and SU-8 are negative-tone photoresists with a near UV processing wavelength. To obtain a layer of photoresist of the desired height it was necessary to dilute the KC-L with ethanol or, for some strategies, to mix the two SU-8 2000.5 and SU-8 2050. The dilution ratios are indicated each time.

3.3.1 Silicon substrate preparation

A 0.5 mm thick Silicon (Si) wafer has been used as substrate for all the strategies described below. Wafer dimensions never exceed 2 cm × 2 cm. Steps for their preparation were identical for all the strategies and are listed below.

1. **Piranha Cleaning:** 10 min immersion in a solution of sulphuric acid and hydrogen peroxide with a 7 : 3 ratio ($H_2(SO)_4 : H_2O_2$), after the immersion the Si wafer is rinsed in deionised water;
2. **Sonication in Acetone:** rinsing for few minutes in Acetone (ACE) in an ultrasonic bath at 50 kHz;
3. **Sonication in Isopropyl alcohol:** rinsing for few minutes in Isopropyl alcohol (IPA) in an ultrasonic bath at 50 kHz;

3.3.2 Coating and exposure

Following the *substrate preparation* step, for all the strategies listed below, the photoresist is spun on top of the pretreated Si wafer. A strategy indicates a specific photoresist used at a specific height.

Photoresist height was confirmed using a DektakXT Stylus Profiler provided by Bruker Corporation. The photoresist profile was checked by running the stylus of the profiler above areas of discontinuity of the photoresist layer, using the top of the photoresist and the bare silicon wafer surface as reference levels. This operation is performed indistinctly by running the stylus over a scratch on the surface of the photoresist which reaches the surface of the silicon wafer, or across an area of the wafer left uncoated. This latter procedure requires part of the silicon wafer to remain uncoated with photoresist. This was achieved by covering part of the wafer with tape before the spin coating step. The profiling technique is summarised schematically in figure 3.6.

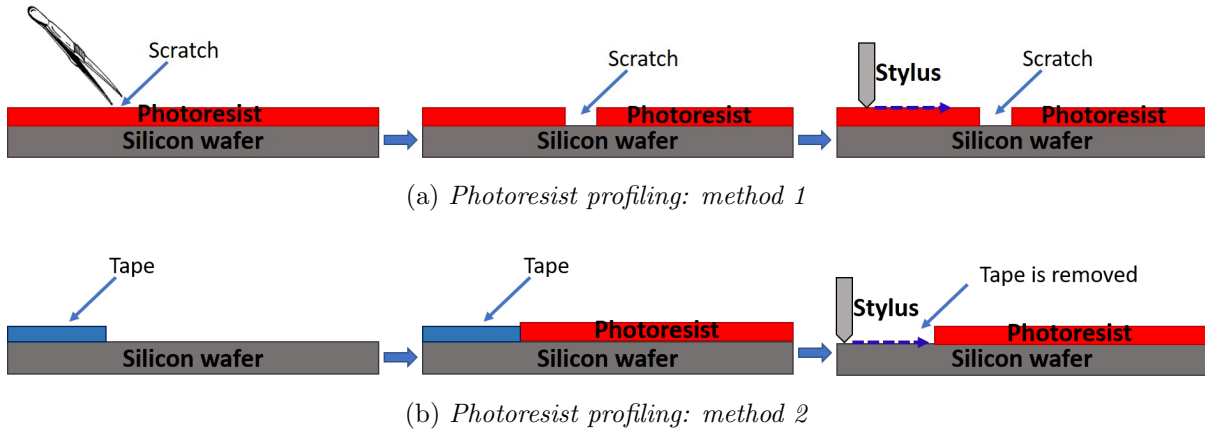


Figure 3.6: Photoresist profiling. Method 1: after the spin coating step, the photoresist layer is scratched until the bare wafer is revealed and the stylus scans across the scratch (a). Method 2: an area of the silicon wafer is left uncoated and the stylus scans across such area. Violet dotted arrow points towards the direction of the stylus scanning (top right and bottom right images).

When the spinning protocol for a specific photoresist height was not available, the photoresist film thickness at various spinning speeds was evaluated using the DektakXT Stylus Profiler and the relative graphs (thickness versus spinning speed) are shown in the next chapter (chapter 4).

For the exposure step with all the strategies the following setup and parameters are left unchanged as stated below.

- **Filling parameters** in *KloeDesign* (see figure A.2 in appendix A):
 1. **spot size** of $0.5 \mu m$;
 2. **overlap rate** of 0% ;
- **Neutral density filter** mounted on *Kloe 650*: NE513A provided by Thorlabs, Inc. (Optical Density: 1.3, Transmission: 5%);
- **Focusing objective lens** mounted on *Kloe 650*: UPLFLN40X provided by Olympus corporation (magnification: $40X$, Numerical Aperture: 0.75, Working distance $0.51 mm$);
- **Optical line**: $0.5 \mu m$ laser spot.

Strategy 1: 500 nm high K-CL

To obtain a $\simeq 500\text{ nm}$ ($0.5\ \mu\text{m}$) high K-CL layer, K-CL 010 photoresist was diluted with ethanol (ETH) following the volume ratio $KCL : ETH \rightarrow 1 : 2$. Table 3.3 lists the parameters used to fabricate a $\simeq 500\text{ nm}$ high K-CL mould imprinted by *Dilase 650* system for DLW lithography.

Spin Coating	Pre Exp. Bake	Exposure			Post Exp. Bake	Dev.	Hard Bake
		Mod.	Speed	Δz			
2500 rpm - 1 min	60°C - 5 min	95%	10 mm/s	+5 μm	NA	2 min in Butanol rinse in Butanol	NA

Table 3.3: Fabrication parameters for a $\simeq 500\text{ nm}$ high K-CL photoresist layer. For the KCL post exposure baking and hard baking are not required.

Strategy 2: 2 μm high SU-8

To obtain a $\simeq 2\ \mu\text{m}$ high SU-8 layer, SU-8 2050 photoresist was diluted with SU-8 2000.5 following the weight ratio $SU8\ 2050 : SU8\ 2000.5 \rightarrow 2 : 7$. Table 3.4 lists the parameters used to fabricate a $\simeq 2\ \mu\text{m}$ high SU-8 mould imprinted by *Dilase 650* system for DLW lithography.

Spin Coating	Pre Exp. Bake	Exposure			Post Exp. Bake	Dev.	Hard Bake
		Mod.	Speed	Δz			
500 rpm - 10 s	65°C - 2 min	70%	0.5 mm/s	+2 μm	65°C - 2 min	2 min in EC solvent rinse in IPA	180°C > 2 h
1500 rpm - 10 s	95°C - 6 min				95°C - 6 min		
3000 rpm - 1 min	65°C - 2 min				65°C - 2 min		

Table 3.4: Fabrication parameters for a $\simeq 2\ \mu\text{m}$ high SU-CL photoresist layer. The three steps indicated for the “Spin Coating”, “Pre Exposure Bake” and “Post Exposure Bake” are sequential.

Strategy 3: 10 μm high SU-8

To obtain a $\simeq 10\ \mu\text{m}$ high SU-8 layer, SU-8 2050 photoresist was diluted with SU-8 2000.5 following the weight ratio $SU8\ 2050 : SU8\ 2000.5 \rightarrow 6 : 2$. Table 3.5 lists the parameters used to fabricate a $\simeq 10\ \mu\text{m}$ high SU-8 mould imprinted by *Dilase 650* system for DLW lithography.

Spin Coating	Pre Exp. Bake	Exposure			Post Exp. Bake	Dev.	Hard Bake
		Mod.	Speed	Δz			
500 rpm - 10 s	65°C - 2 min	83%	3 mm/s	+2 μm	65°C - 2 min	6 min in EC solvent rinse in IPA	180°C > 2 h
3000 rpm - 1 min	95°C - 6 min				95°C - 6 min		
	65°C - 2 min				65°C - 2 min		

Table 3.5: Fabrication parameters for a $\simeq 10\ \mu\text{m}$ high SU-CL photoresist layer. Steps indicated for the “Spin Coating”, “Pre Exposure Bake” and “Post Exposure Bake” are sequential.

Strategy 4: double layer SU-8

To obtain a double layer of SU-8 photoresist, two SU-8 moulds were fabricated sequentially one on top of the other. The bottom layer is a $\simeq 800\text{ nm}$ ($0.8\ \mu\text{m}$) high SU-8 layer obtained by spin coating and DLW SU-8 2000.5 photoresist following parameters in table 3.6.

Spin Coating	Pre Exp. Bake	Exposure			Post Exp. Bake	Dev.	Hard Bake
		Mod.	Speed	Δz			
500 rpm - 15 s 6000 rpm - 30 s	65°C - 2 min 95°C - 6 min 65°C - 2 min	40%	1.5 mm/s	+1 μm	65°C - 2 min 95°C - 6 min 65°C - 2 min	2 min in EC solvent rinse in IPA	180°C > 2 h

Table 3.6: Fabrication parameters for a $\simeq 800\text{ nm}$ high SU-CL photoresist layer. Steps indicated for the “Spin Coating”, “Pre Exposure Bake” and “Post Exposure Bake” are sequential.

To precisely align the two layers, when imprinting the bottom one by DLW, three crosses that act as alignment markers were exposed in addition to the desired pattern. The crosses were respectively positioned at the bottom left corner of the sample, at the top left corner of the sample and on the bottom right corner of the sample, centred at points of known coordinates with respect to the sides of the silicon wafer. Coordinates are known from the *KloeDesign* software. Before exposing the second layer, translation and angular compensation can be applied with respect of the three markers completing a “three point alignment” procedure.

The top layer is a $\simeq 20\ \mu\text{m}$ high SU-8 layer obtained by spin coating and DLW SU-8 2050 photoresist following parameters in table 3.7.

Spin Coating	Pre Exp. Bake	Exposure			Post Exp. Bake	Dev.	Hard Bake
		Mod.	Speed	Δz			
500 rpm - 10 s 2000 rpm - 30 s 5000 rpm - 1 min	65°C - 3 min 95°C - 9 min 65°C - 3 min	50%	4 mm/s	+15 μm	65°C - 2 min 95°C - 10 min 65°C - 2 min	6 min in EC solvent rinse in IPA	180°C > 2 h

Table 3.7: Fabrication parameters for a $\simeq 20\ \mu\text{m}$ high SU-CL photoresist layer. Steps indicated for the “Spin Coating”, “Pre Exposure Bake” and “Post Exposure Bake” are sequential.

3.4 PDMS replication moulding, PDMS cutting and PDMS-glass bonding

Once the mould is ready, PDMS is prepared in order to be poured on top of the silicon-photoresist mould. The entire replication moulding process from the PDMS preparation to the PDMS-glass bonding step (figure 3.1) is described below.

1. PDMS prepolymer and curing agent (*Sylgard 184*, Dow Corning Co.,UK) are mixed following the volume ratio $PDMS_{prepolymer} : curing\ agent \rightarrow 10 : 1.3$ or $PDMS_{prepolymer} : curing\ agent \rightarrow 7 : 1$. Increasing the curing agent content in the mixture contributes to increase the stiffness of the final PDMS device, so the ratio was first changed from 10 : 1.3 to 7 : 1 to prevent the collapse of small PDMS features after their enclosure at the PDMS-glass bonding step. In the end, this issue was fixed changing the priming procedure (see chapter 4 for reference) and it has been observed that the two different ratios $PDMS_{prepolymer} : curing\ agent$ can be used indiscriminately;
2. the PDMS mixture is stirred for few minutes, until opaque;
3. the PDMS mixture is degassed for $\simeq 20 - 25\ min$ under slight vacuum (10 mbar), until bubbles disappear;
4. the mould is placed in a Petri dish (diameter: $\simeq 60\ mm$, height: $\simeq 15\ mm$) and the PDMS mixture is poured in it to create a layer just under 1 cm high;
5. the PDMS mixture is left at $60^\circ C$ for at least 6 hours;
6. the PDMS slab is carefully peeled off from the mould and cut into a single chip with a scalpel;
7. inlets and outlets are punched with a 2 mm diameter hole-puncher;
8. the PDMS chip and a glass microscope slide are cleaned:
 - PDMS: 5 min sonication in IPA at 50 kHz, 5 min sonication in DI water at 50 kHz;
 - glass slide: 10 min immersion in piranha solution ($(H_2(SO)_4 : H_2O_2) \rightarrow 7 : 3$), rinsing in DI water, 5 min sonication in ACE at 50 kHz, 5 min sonication in IPA at 50 kHz;
9. oxygen plasma bonding:
 - (a) glass slide plasma oxidation: $Power = 20\ W, Time = 2\ min, oxygen\ flowrate = 5\ sccm$);
 - (b) PDMS plasma oxidation: $Power = 100\ W, Time = 2\ sec, oxygen\ flowrate = 5\ sccm$);
 - (c) PDMS chip is placed onto the glass slide.
10. the PDMS-glass device is left at $60^\circ C$ for at least 4 h.

3.5 Double layer PDMS device

Following the protocol reported by Xiaofei Yuan et al [52], a two layer PDMS device has been also attempted to build a micro-well for bacterial culturing. To fabricate a micro well as the one shown in figure 2.8 we started without changing the dimensions for the bottom layer of the device used by Xiaofei Yuan et. al [52] and using a protocol already tested for the top layer

To fabricate the bottom PDMS layer the first three steps listed in previous section 3.4 are repeated. Then to obtain a $250\ \mu\text{m}$ high PDMS layer, the PDMS mixture is spun on top of a $2\ \text{cm} \times 2\ \text{cm}$ Si wafer at $380\ \text{rpm}$ for $30\ \text{s}$. After this the PDMS is cured at 60°C for at least $6\ \text{hours}$ and after this time the thin layer is peeled off from the Si wafer. After peeling it, it is punched to create the culturing well using a $1\ \text{mm}$ diameter hole-puncher. Once punched the PDMS is cleaned following step 8 of section 3.4 and bounded to a glass microscope slide by Oxygen plasma treatment followed by thermal bonding (step 9 and 10 section 3.4).

For the top layer, a $\simeq 20\ \mu\text{m}$ high PDMS chamber has been fabricated through replica moulding process of a SU-8 2050 mould coated and imprinted by DLW lithography using parameters listed in table 3.7. Then the mould has been used for PDMS replica moulding repeating steps from 1 to 8 (only the one concerning the PDMS treatment) illustrated in section 3.4. The top layer was subsequently bounded to the bottom layer (thin PDMS layer-glass) by oxygen plasma followed by thermal bonding (steps 8-9 section 3.4).

3.6 Sample preparation, device loading, experimental setup and post-processing

Materials and protocols listed in the current section are kept identical for all the experiments summarised in chapter 4. Two bacterial strains were alternated during the experiments: *E.coli* w3110 and *E.coli* Mg1655. With the final aim of testing a microfluidic device for bacterial culture the use of one strain rather than the other does not make any difference.

Preparation of the Bacterial Culture

From an agar plate containing the living desired bacteria strain, one colony is inoculated into $5\ \text{ml}$ of Lysogeny broth (sterilised solution of *Tryptone* : $10\ \text{g/l}$ and *NaCl* : $10\ \text{g/l}$ and *Yeast extract* : $5\ \text{g/l}$ in DI water) in a $50\ \text{ml}$ tube and incubated overnight at 37°C in static conditions. The following day the desired concentration of bacteria to be inoculated into the microfluidic device is transferred in a smaller tube (generally a $1.5\ \text{ml}$ tube). With the strains used, the initial optical density at $600\ \text{nm}$ (OD_{600}), measured with a spectrometer, is kept between 0.5 and 1.

Device priming and seeding of Bacterial Cells

The device priming step consists in the filling of the device with the medium (Lysogeny broth) necessary for the competition of the bacterial growth experiment inside the microfluidic device.

To prime the device the inlet is connected through a microfluidic plastic tube (inner diameter: 0.8 mm , outer diameter: 2.4 mm , wall thickness: 0.8 mm) to a syringe-pump loaded with a 1 ml syringe containing Lysogeny broth. Connection between the syringe and the tube is guaranteed by $1 - 100\ \mu\text{l}$ standard Eppendorf pipette tip. The Lysogeny broth is flushed into the device at $10\ \mu\text{l}/\text{min}$ for few minutes, the process is checked in real time under a microscope. The device filled with Lysogeny broth is loaded with $10\ \mu\text{l}$ bacteria solution ($OD_{600} = 0.5 - 1$). Bacteria solution is inoculated with a micro-pipette directly inside the device, once bacteria are distributed within the device it is left to settle for $\simeq 20\text{ min}$ before starting the observation.

Experimental setup

Once inoculated the device is observed for 12 h with Nikon Ti2-U phase contrast and inverted microscope using a $20\times$ objective. The microscope is provided by a motorised stage (Thorlabs, Inc.) to hold the sample. Images are collected every 3 min by a bright field camera mounted on the microscope system (Point Grey blackfly USB3). The overall setup is connected to a computer system where the main parameters for the acquisition are controlled by *Micro-manager* software.

Image processing and modelling

Image processing on the acquired pictures is completed using MATLAB programming language (version: MATLAB 9.7 - R2019b) by MathWorks with a custom-written script. Physical modelling of the microfluidic devices was performed using COMSOL Multiphysics 5.5 and mainly consisted of simulations of the fluid flow in geometries reproducing the actual designs tested with considerations on possible optimisation of the bacterial culture module.

Chapter 4

Preliminary results and discussion

This chapter presents the results of experimental research into the fabrication and characterisation of a microfluidic device for bacterial culturing. As stated in chapter 1, the period of experimental work was severely curtailed (to c. 6 months) due to access restrictions as a result of the COVID-19 pandemic. This chapter includes a discussion on:

1. Optimised protocols for fabrication of PDMS microfluidic devices using mask-less lithography technique;
2. The successful growth of a single strain of bacteria inoculated in the PDMS microfluidic system, for a period of 12 hours;
3. A simple but generic MATLAB script to automate cell counting within a microfluidic culturing device.

Informed by these initial experiments, the chapter concludes with the presentation of an optimised prototype microfluidic device capable of bacterial culture.

4.1 Microfluidic compartments separated by nano-channel

Initial research focussed on a microfluidic device for bacterial mixed co-culture consisting of two culturing compartments connected through a channel that was sufficiently small to prevent bacteria from moving between compartments but large enough to allow metabolite exchange via diffusion (panel a of figure 1.1). From the scientific literature, it is known that such physical but not chemical separation is possible if the channel between culture chambers is sufficiently smaller than the diameter of the bacteria involved (see section 2.2.2). The diameter of most bacteria, including *E. coli*, *P. Aeruginosa* and *S. Aureus* is generally larger than $0.5\ \mu\text{m}$. This is equivalent to the resolution limit of the *Dilase 650* system used for Direct Laser Writing (DLW) (figure 3.5). Research thus focussed initially on optimising the protocol for fabrication of a $0.5\ \mu\text{m}$ wide channel. This was achieved via a dose trial in which an array of repeating patterns was exposed while the exposure parameters (laser power, writing speed and focusing head position) were varied. In this case a single laser trajectory line was chosen as the design to be repeated with different lithography parameters.

4.1.1 K-CL: DLW parameters optimisation

Research started initially with the K-CL photoresist, that has been designed specifically for use with the *Dilase 650*. The protocol summarised in table 3.3 was developed for use with a K-CL layer of $\simeq 500\text{ nm}$ thick. The thickness of the K-CL layer was confirmed by the profile of the photoresist analysed with the DektakXT Stylus Profiler. The resulting profile is shown in figure 4.1.

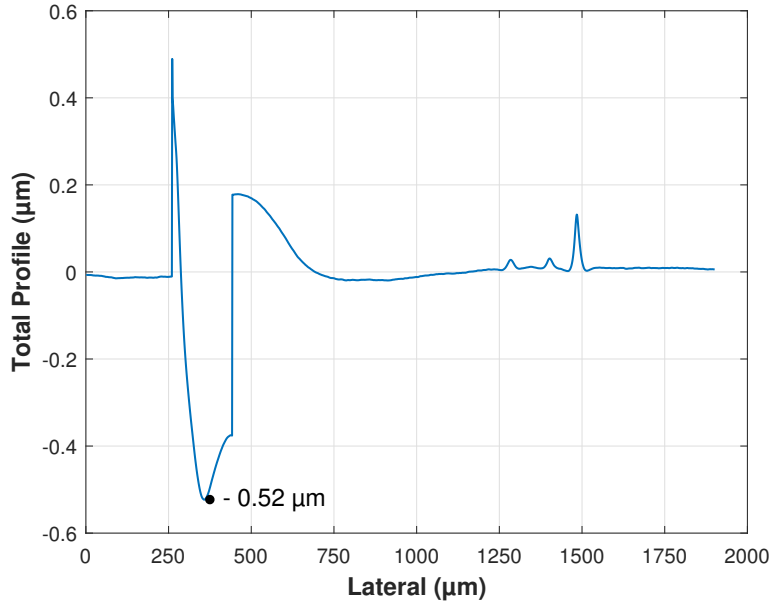


Figure 4.1: $0.5\ \mu\text{m}$ thick K-CL layer: stylus profile. Exported data from the DektakXT Stylus Profiler: the $0\ \mu\text{m}$ value for the “Total profile” corresponds to the top surface of the photoresist layer, near the scratch the profile shows an accumulation of material (positive peak), the negative peak corresponds to the surface of the silicon wafer. The absolute value of the negative peak is representative of the height of the photoresist layer. Bigger negative peak is marked in the graph (point at $\simeq -0.5\ \mu\text{m}$).

After confirming a layer thickness of 500 nm , the deposition parameters (spin speed, time and pre-bake) were left unchanged for all subsequent lithography optimisation tests. I note, a 500 nm high PDMS chamber generated from such a K-CL mould would ultimately be suitable as a monolayer growth chamber for bacterial culturing.

The dose trial was performed using a *Laser power* = 95% while the writing speeds varied as *Writing speed* between $[10 - 15 - 20]\text{ mm/s}$. The Δz was also varied between $[-10 - -5 - 0 - +5 - +10]\ \mu\text{m}$ to be sure to expose as close to the focus plane. The value of the z coordinate of the focusing head, before the Δz adjustment during exposure was $z_{\text{focusing head}} = 5.3476 \pm 0.0026\ \text{mm}$.

From the dose trial, a single line was observed with dimensions comparable to the designed line (figure 4.2). The parameters used for the exposure shown in figure 4.2 are the given in table 3.3.

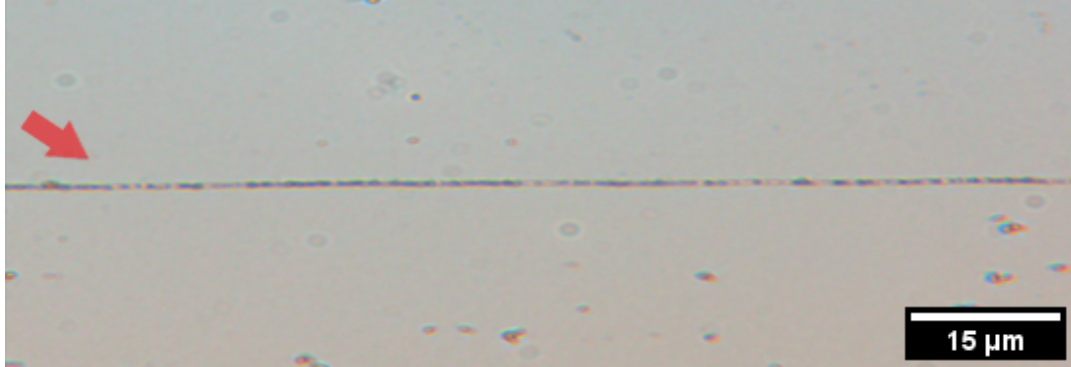


Figure 4.2: 500 nm high K-CL: lithography parameters optimisation. The figure shows a microscopic image of a 500 nm high K-CL mould patterned by DLW with *Dilase 650* at *Laser power* = 95%, *Writing speed* = 10 mm/s, $\Delta z = +5$ nm. The imprinted pattern reproduces a feature attributable to a $\simeq 500$ nm wide line slightly underexposed underdeveloped. The red arrow points to the imprinted feature.

I note, this line (figure 4.2) remains slightly underexposed/ underdeveloped and further optimisation of the lithography would be required to improve the fidelity of this feature. However, following further dose trials, it was observed that the photoresist adhered poorly to the silicon wafer, in fact a slight pressure with metal tweezers was sufficient to detach the photoresist from the silicon substrate, and thus it is unsuitable for subsequent replication moulding steps. Poor adhesion was observed even following the inclusion of a hard baking step at 100°C recommended as “optional” in the K-CL data-sheet. For this reason it was decided to change the photoresist and start working with SU-8, widely used in microfluidic applications including the fabrication of PDMS devices via replica moulding.

4.1.2 SU-8: DLW parameters optimisation

To optimise the parameters for the exposure of a $\simeq 500$ nm wide line into a SU-8 layer, I started by testing the feasibility of a stable exposure close to the nominal smallest laser size spot. A coating protocol for a $\simeq 2$ μm thick SU-8 layer was followed (table 3.4). The height of the photoresist layer was checked with the DektakXT Stylus Profiler, following method N°1 of figure 3.6. The resulting profile is shown in figure 4.3.

Optimisation of the lithography parameters was carried out by exposing single lines 100 μm long using the 500 nm wide laser line. Four values of *laser power* were combined with three values of writing speed and five values of Δz . The values are listed below.

- **Laser power:** 50% – 60% – 70% – 80 %;
- **Writing speed:** 0.5 mm/s – 1 mm/s – 1.5 mm/s;
- **Δz :** -2 μm – -1 μm – 0 μm – +1 μm – +2 μm.

The value of the z coordinate of the focusing head, before the Δz adjustment was $z_{focusing\ head} = 5.3431 \pm 0.0023$ mm.

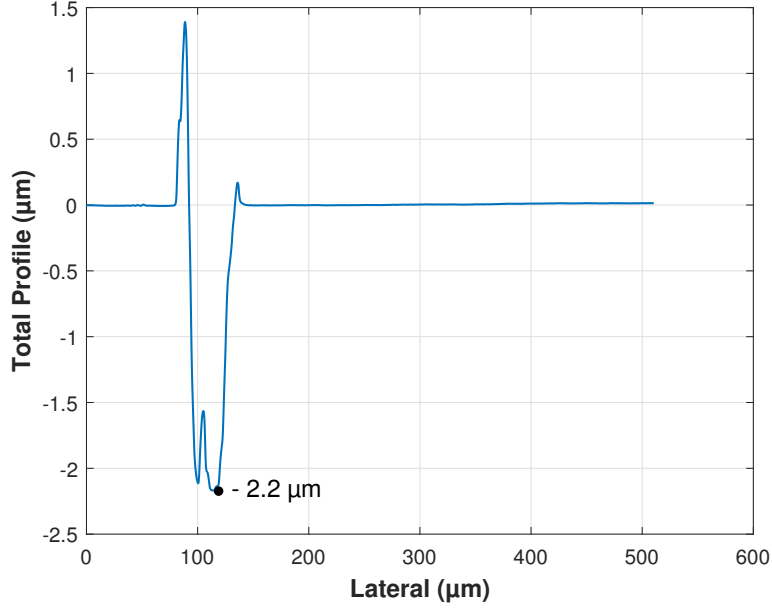


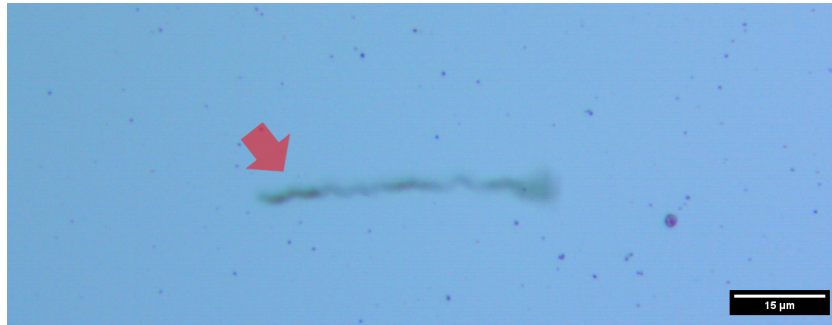
Figure 4.3: $2\ \mu\text{m}$ thick SU-8 layer: stylus profile. Exported data from the DektakXT Stylus Profiler: the $0\ \mu\text{m}$ value for the “Total profile” corresponds to the top surface of the photoresist layer, near the scratch the profile shows an accumulation of material (positive peak), the negative peak corresponds to the surface of the silicon wafer. The absolute value of the negative peak is representative of the height of the photoresist layer. Bigger negative peak is marked in the graph (point at $\simeq -2\ \mu\text{m}$).

Features written at minimum laser power ($Laser\ Power = 50\%$) and maximum writing speed ($Writing\ Speed = 1.5\ \text{mm/s}$), corresponding to the lowest dose, did not appear after the development. Features written at the maximum laser power ($Laser\ Power = 80\%$) and minimum speed ($Writing\ Speed = 0.5\ \text{mm/s}$) were all evident after development however showing an overall instability; the lines do not appear straight but wavy. Table 4.1 summarises the results of the optimisation test.

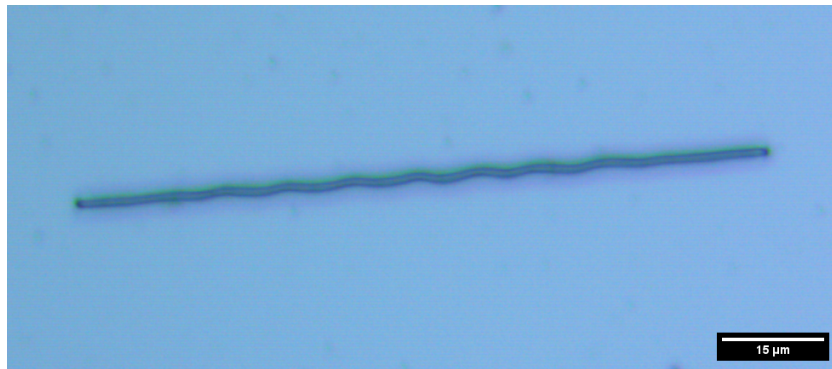
		Laser Power			
		50%	60%	70%	80%
Writing Speed [mm/s]	1.5	No features	Not all features	Not all features	Not all features
	1	Under-exposed wavy	Under-exposed wavy	Under-exposed wavy	All features but wavy
	0.5	All features but wavy			

Table 4.1: Results of the tests for the optimisation of the DLW lithography parameters for a $2\ \mu\text{m}$ thick SU-8 photoresist layer. Each box summarises the results for all the Δz values at that specific combination of “Laser Power” and “Writing Speed”. For higher speed values all the tests appeared highly under-exposed with some features not even imprinted (red boxes), for intermediate speed values features were imprinted but sometimes appeared highly underexposed (yellow boxes) while for lower speed values all the tests showed imprinted features. Overall, all the tests showed wavy features instead of straight lines.

Figure 4.4 compares a heavily underexposed feature and a properly exposed one. Both exposures correspond to a single laser line at 500 nm size spot, when the dose is far below the threshold needed to imprint the photoresist the exposed pattern does not appear after development.



(a) Power: 50%, Speed: 1 mm/s, Δz : +2 μm



(b) Power: 80%, Speed: 0.5 mm/s, Δz : +2 μm

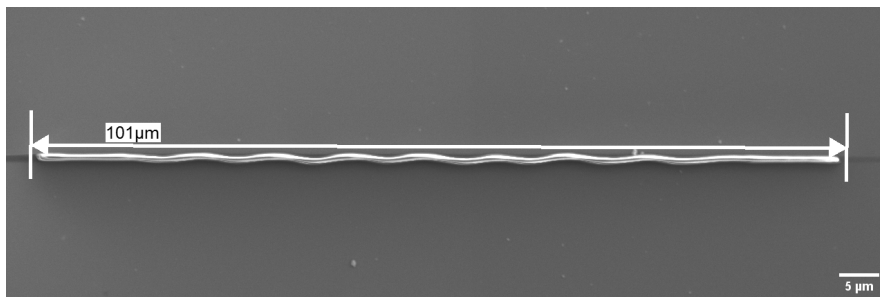
Figure 4.4: Nominally 500 nm wide line on a $2\text{ }\mu\text{m}$ high SU-8 layer (actual width $1\text{ }\mu\text{m}$). Microscopic images of a $2\text{ }\mu\text{m}$ high SU-8 mould imprinted by DLW with *Dilase 650*: two exposures with the same Δz at low dose (a) and sufficient dose (b). As already mentioned, even when imprinted with a sufficient dose, features appear wavy rather than straight. The red arrow in panel a points toward the feature.

The optimised exposure conditions corresponded to a *Laser Power* = 70%, *Writing Speed* = 0.5 mm/s and $\Delta z = +2\text{ }\mu\text{m}$ (figure 4.5). Therefore these parameters constitute a good protocol for the exposures of $2\text{ }\mu\text{m}$ high SU-8 layers. However, even at these optimal conditions, none of the features had a width smaller than $1\text{ }\mu\text{m}$.

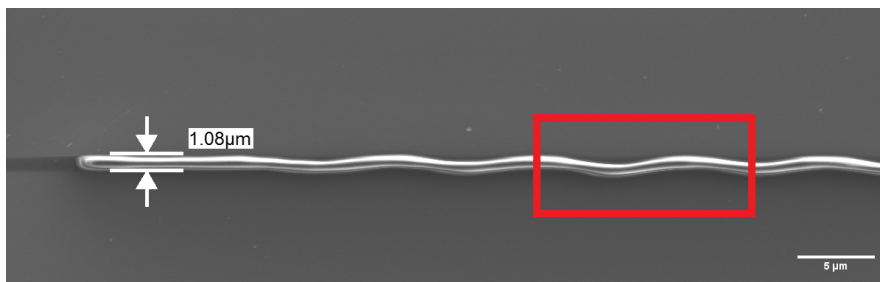
For all the following exposures with the same substrate conditions, this set of lithography parameters was used and it confirmed to be a good combination. Nevertheless, SEM images of the pattern exposed with such lithography parameters (figure 4.5) confirmed that a line of width less than $1\text{ }\mu\text{m}$ is hard or even impossible to define.



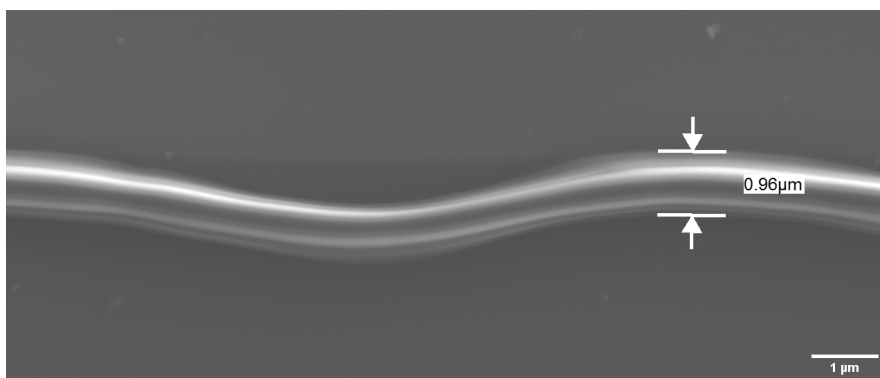
(a) *Microscopic Image*



(b) *SEM image: length marker*



(c) *SEM image: width marker in point N° 1*



(d) *SEM image: zoom and width marker in point N° 2*

Figure 4.5: 500 nm wide line on a 2 μm high SU-8 layer: optimised lithography parameters. Microscopic image of the pattern after development (a). SEM images of the pattern exposed at Laser Power: 70%, Writing Speed: 0.5 mm/s and Δz : +2 μm. Representation of the whole pattern (b), zoom on one end of the line and width indication (c). Panel d shows a zoom on a wavy portion of the line (red box in panel c) with relative width indication.

As already mentioned the result of this optimisation process is not fully satisfactory for two main reasons:

1. the smallest line width was twice the nominal focal spot of the *Dilase 650* Laser optical line 1 (table 3.1);
2. lines appear wavy instead of straight as designed.

The first issue is mainly due to the intrinsic difficulty in exposing a pattern whose dimensions are close to the resolution limit of the *Dilase 650* DLW system. The *Dilase 650* manufacturer recommends that such dimensions can generally be reached by exposing the speciality K-CL photoresist, however adhesion problems inhibited the use of this resist (section 4.1.1). In any case, the closer the design gets to the resolution limit, the more precise the optical alignment must be. Even with perfect alignment, There are a number of other factors that need to be optimised and controlled precisely in order to reach the resolution limit. For example, the uniformity of the photoresist layer can not be easily controlled while spin-coating the SU-8 on top of the silicon wafer. In such circumstances, exposing only few nanometres above or below the focusing plane can strongly impact the exposure. High aspect ratios also play a crucial role in determining the smallest possible feature, but with UV exposure of SU-8, aspect ratios up to 20 have already been achieved in 2002 [77] so imprinting a $0.5\ \mu\text{m}$ wide line in a $2\ \mu\text{m}$ high SU-8 layer should be possible.

The undulations of the imprinted SU-8 lines may be related to a combination of factors including the structural stability of such a thin, long feature and the instability of the direct laser writer, potentially at the level of the stage holding the sample. While shortening the line would have not compromised the operating principle of the final device, time limitations prevented research to confirm this.

4.2 Microfluidic module for bacterial culture

While studying the best solution to separate two bacterial culture compartments within a microfluidic device, I also started working on the design of a simple device consisting of a single growth chamber to investigate bacterial culturing in a microfluidic device. Specifically, this investigation would confirm whether it was possible to inoculate a single bacterial species into a microfabricated PDMS microfluidic device and to culture the bacteria for a period of time long enough to permit the analysis of the growth rate.

4.2.1 First design: back-pressure and priming difficulties

Initial devices were fabricated using the optimised protocol for a $2\ \mu\text{m}$ high SU-8 mould that in the end means having PDMS features $2\ \mu\text{m}$ high. Although this height is not small enough to allow a monolayer growth of the bacteria, it was decided to postpone the optimisation of new spinning and exposure protocols for a lower SU-8 layer in favour of confirming that bacterial growth was not severely compromised inside the microfluidic device.

The first design attempted is shown in figure 4.6. This consists of a central $2\ \mu\text{m}$ high culture chamber with a diameter of $200\ \mu\text{m}$ that is connected to fluidic input and output ports through two channels $10\ \mu\text{m}$ wide, $2\ \mu\text{m}$ high and $1.4\ \text{mm}$ long. The protocol used to fabricate the SU-8 mould for this platform is summarised in table 3.4.

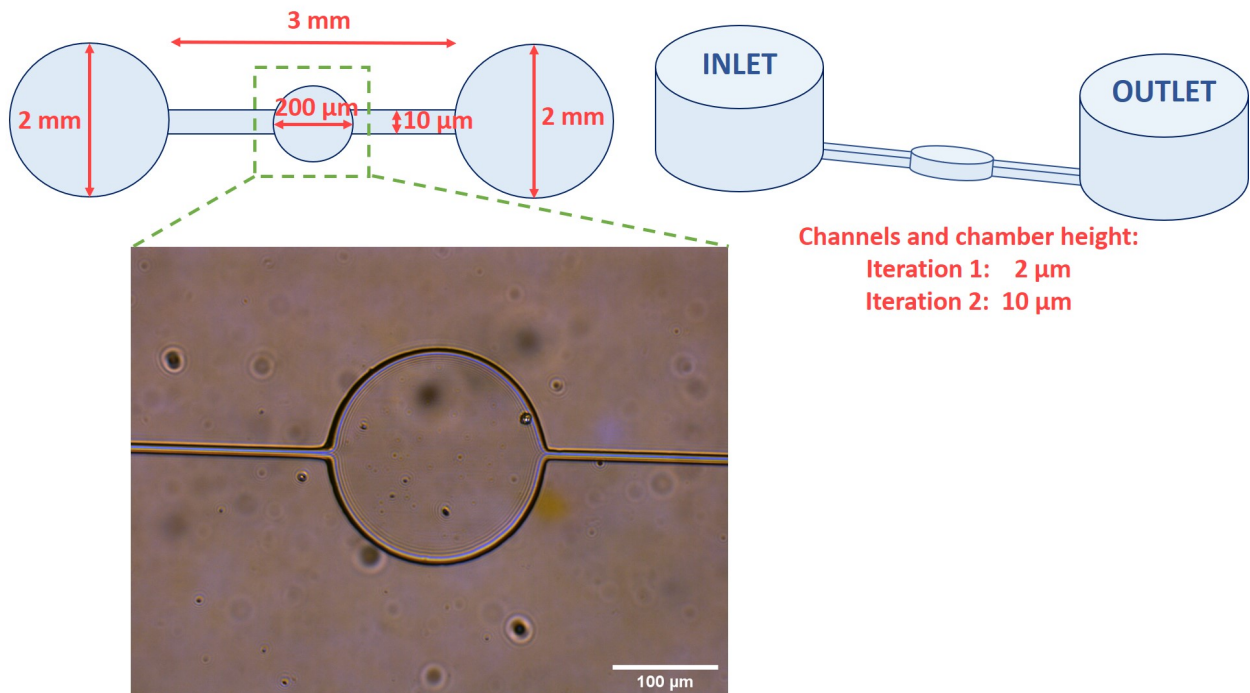


Figure 4.6: Platform for bacterial culture: design N° 1. Top: schematic structure of the platform design and relative dimensions (left), schematic 3D representation of the PDMS device (right). Two heights are indicated since the experiment has been attempted twice increasing the height to promote platform priming. Bottom: microscopic image of the central chamber in the PDMS device.

Before employing the protocol described in chapter 3, a range of other priming methods were attempted without success; including (in chronological order):

1. direct syringe injection;
2. direct micropipette injection;
3. direct syringe injection applying pressure at the outlet with an absorbing pad;
4. direct micropipette injection in combination with an absorbing pad at the outlet port;

A possible explanation for the failure of each of these approaches is that the constriction between the inlet port and channel results in a significant drop in pressure leading to a reduced rate flow. In order to reduce this pressure drop, I firstly investigated increasing the height of the channel and growth chamber. A device of identical geometry was fabricated but now using a $\simeq 10\ \mu\text{m}$ deep channel, as shown in figure 4.6. The following subsection discusses the optimisation of the spinning protocol for a $10\ \mu\text{m}$ thick SU-8 layer.

10 μm thick SU-8 layer: spin-coating optimisation

After mixing and magnetically stirring overnight two parts of SU-8 2000.5 with six of SU-8 2050, a range of spin speeds from 3000 rpm to 5000 rpm were tested. The thickness of each SU8 layer was measured using a Dektak Stylus Profiler following method 2 of figure 3.6. Results of the spin-coating process are summarised in the graph of figure 4.7. Based on these results, a spin speed of 3000 rpm was found to result in an SU8 layer of thickness $9.91 \pm 0.04 \mu\text{m}$.

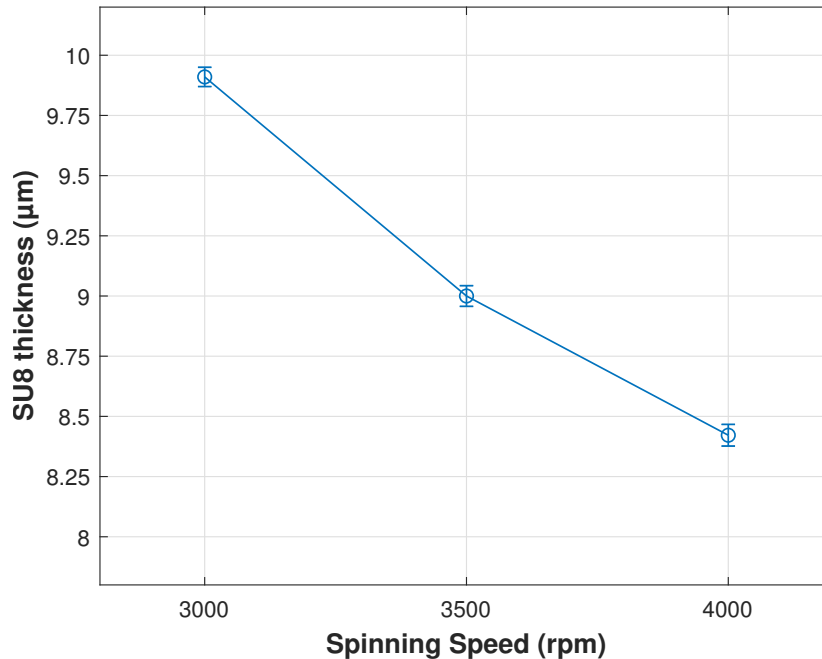


Figure 4.7: 10 μm thick SU-8: spin curves for different spin speeds. The higher the spin speed, the thinner the film, as expected. Each test consists of two spinning steps: the first is kept at the same speed for all the tests while values in the graph refer to the second spinning step. First step is at 500 rpm for 10 s for all the tests. The duration of the second step is 1 min for all the tests. Error bars refer to the standard error over five different locations across the sample being scanned by the stylus profiler.

While a microfluidic device with increased channel height was successfully fabricated, it was again not possible to flood the device with Lysogeny broth.

4.2.2 Second design: back-pressure and priming difficulties

Keeping in mind that the issue with the priming may be caused by a high back-pressure preventing the liquid from entering the channel, I next tried to resolve the problem again using 10 μm high channels but with an alternative geometry at the input/ output ports. Specifically, rather than an abrupt change in width at the interface between the input/output ports and the flow channels, a device was fabricated that gradually reduced the physical channel size as shown in the schematic of figure 4.8. Here, the diameter of the inlet and outlet ports (2 mm) was tapered symmetrically at a rate of $\simeq 60 \mu\text{m}/\mu\text{m}$ until it matched the 10 μm width of the channel.

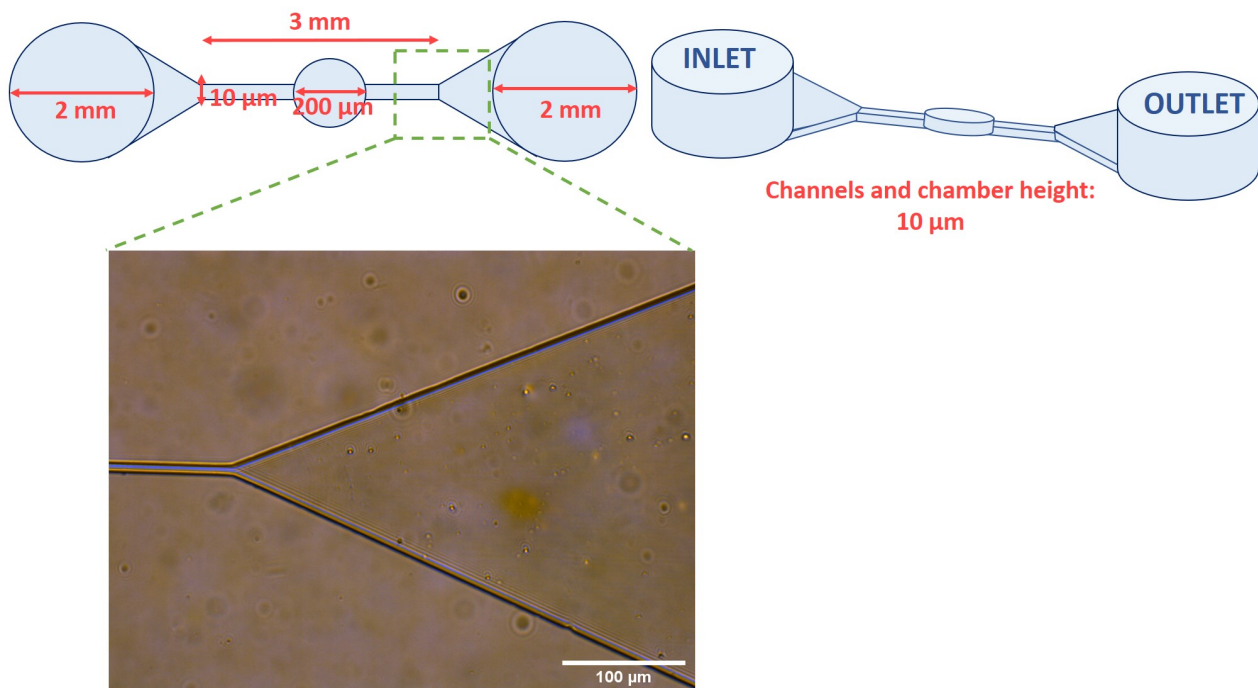


Figure 4.8: Platform for bacterial culture: design N° 2. Top: schematic structure of the platform design and relative dimensions (left), schematic 3D representation of the PDMS device (right). This design as been tested only with $10\ \mu\text{m}$ high structures. Bottom: microscopic image of the outlet/inlet structure in the PDMS device.

Unfortunately, again the design shown in figure 4.8 could still not be primed with Lysogeny broth.

At this point, instead of further raising the height of the microfluidic structure, which ideally must be reduced to achieve a mono-layer bacterial culture, the geometry of the design was further modified to reduce the pressure drop between the inlet/outlet ports and the connection channel to the culture chamber.

4.2.3 Third design: clogging and difficulties in the specific localisation of bacteria within the device

The third design attempted for the bacterial culture microfluidic module is shown in figure 4.9. To minimise the resistance to the fluid flow from the inlet through the channel, the channel dimensions have been increased. The channel is $2\ \text{mm}$ wide and $2.5\ \text{mm}$ long before again tapering to the central culturing chamber where it enters with an aperture of $\simeq 10\ \mu\text{m}$.

Research focused initially on a device with a channel height of $10\ \mu\text{m}$ that was successfully primed with Lysogeny broth through a direct syringe injection method. Having demonstrated priming, a second device of identical geometry but with a reduced channel height ($2\ \mu\text{m}$) was also fabricated, that is more suitable for culturing of a bacterial monolayer. Again, this

reduced thickness device was successfully primed with Lysogeny broth through a direct syringe injection method, allowing inoculation with *E. coli* w3110.

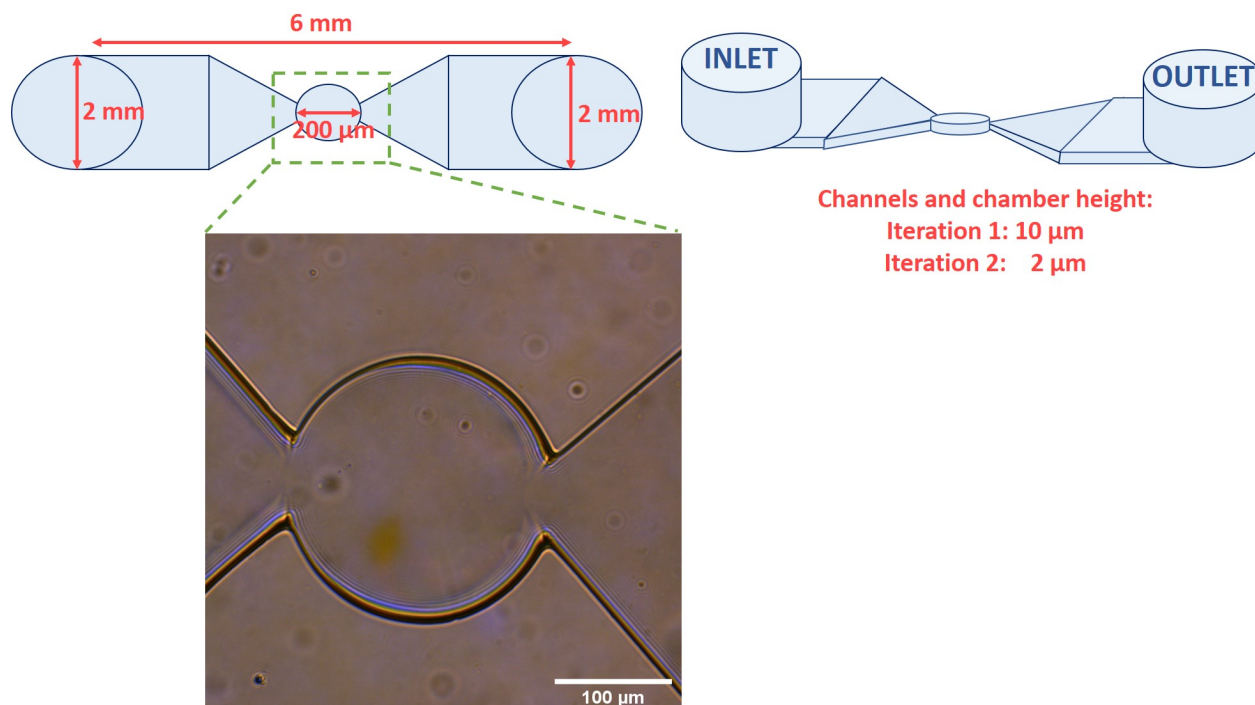
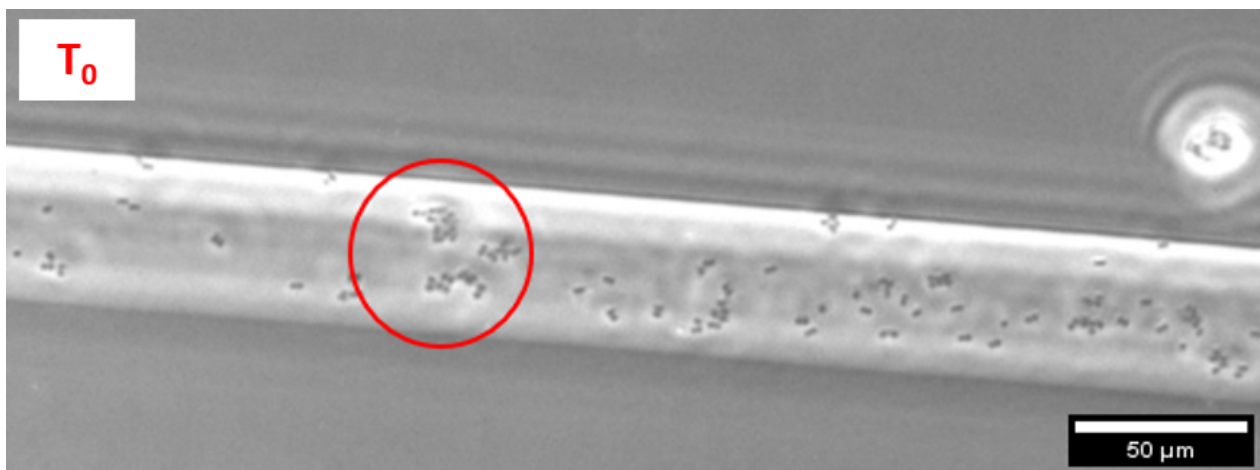


Figure 4.9: Platform for bacterial culture: design N° 3. Top: schematic structure of the platform design and relative dimensions (left), three dimensional schematic representation of the PDMS device (right). Two heights are indicated since the experiment has been attempted twice: once successfully primed the $10\ \mu\text{m}$ high platform the height has been reduced to $2\ \mu\text{m}$ to verify that the priming issue was effectively solved exclusively by the design change. Bottom: microscopic image of the central chamber in the PDMS device.

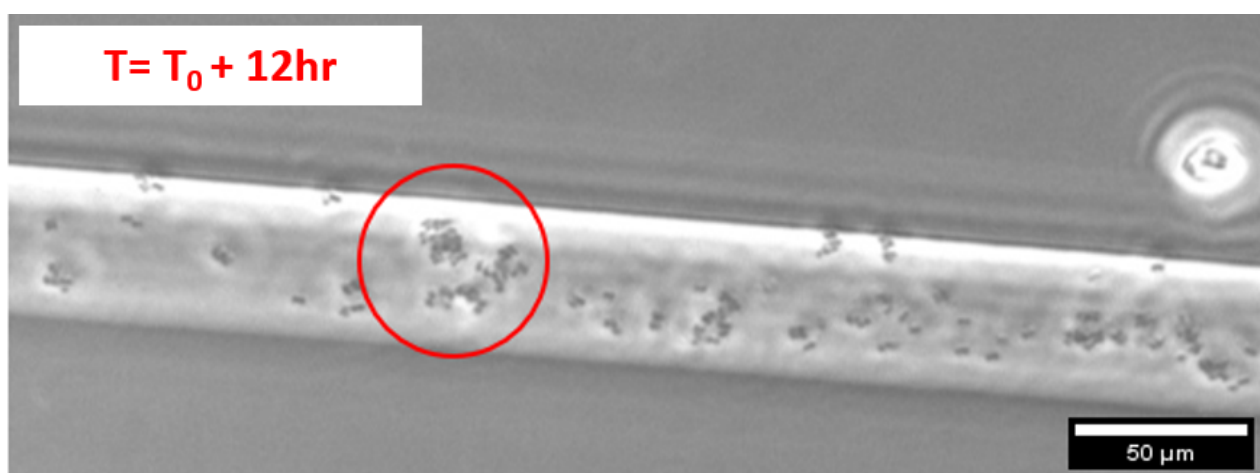
Bacterial culturing experiments

The inoculated device ($2\ \mu\text{m}$ high design shown in figure 4.9) was mounted on an inverted optical microscope which was focussed manually onto bacteria visible within the microfluidic device. Images were subsequently collected every three minutes for a total of 12 hours. Microscopic images at the time of bacteria inoculation and after the 12 hours of recording are shown in figure 4.10.

From a simple visual comparison (figure 4.10), it is possible to confirm an increase in the number of bacteria over time, testifying the growth of the population occurred in a microfluidic device. In itself this is already a first important result: we are able to grow bacteria in a PDMS device. Quantification of bacterial growth is discussed in chapter 4.3.



(a) *Few min since bacteria inoculation*



(b) *12 h since bacteria inoculation*

Figure 4.10: Platform for bacterial culture: design N° 3 after bacteria inoculation. Panel (a) and panel (b) show two subsequent microscopic images of the same area inside the platform. As visible, the total number of bacteria has increased over 12 hours. The red circle enlightens a zone where the bacteria growth can be easily observed. Image was taken after 10 minutes since the device seeding with bacteria.

I note, following inoculation, the PDMS structure was found to have collapsed onto the surface. This is believed to be due to mechanical stresses following insertion of a pipette tip mounted on a 1 ml syringe in the device inlet port. As evidence of this statement, when the platform is primed with Lysogeny Broth using a syringe pump and a constant flow rate (protocol described in chapter 3) no collapse was observed allowing flow to continue.

Therefore, the fabricated single chamber PDMS devices were primed, prior to inoculation, with Lysogeny broth by means of a syringe pump while the priming was monitored using an optical microscope. The overall setup is shown in figure 4.11.

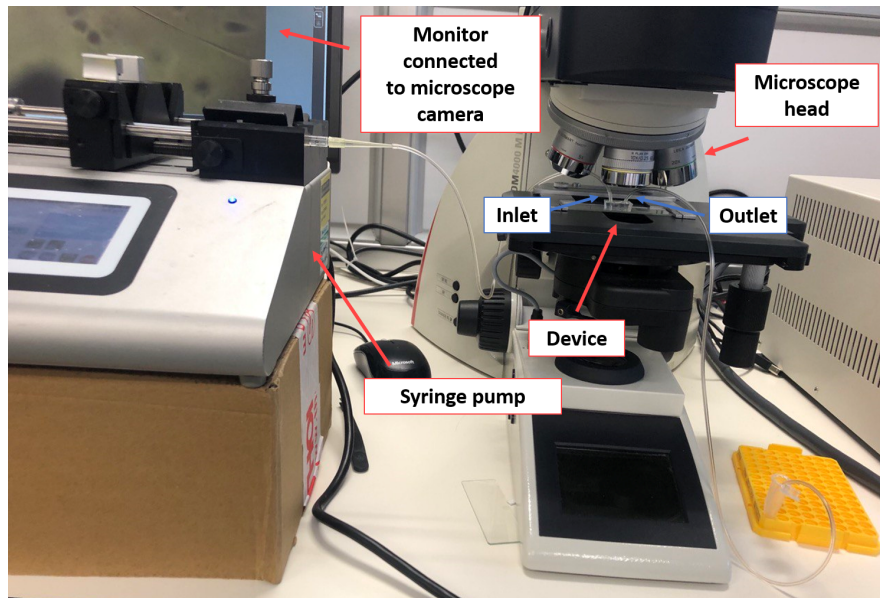


Figure 4.11: Setup for device priming. To prime the device with Lysogeny broth the inlet is connected through a microfluidic tube to a syringe mounted on a syringe pump while the outlet is connected through a microfluidic tube to a reservoir. Difference in heights between the device plane, the pump and the reservoir are chosen to speed up the priming process that is real time controlled from a monitor connected to a camera mounted on a microscope pointing the device.

After priming with Lysogeny Broth (priming setup shown in figure 4.11) the device was seeded with bacteria as described in chapter 3. Preventing PDMS structures from collapsing allows motile bacteria to swim into the central culturing chamber as shown in figure 4.12.

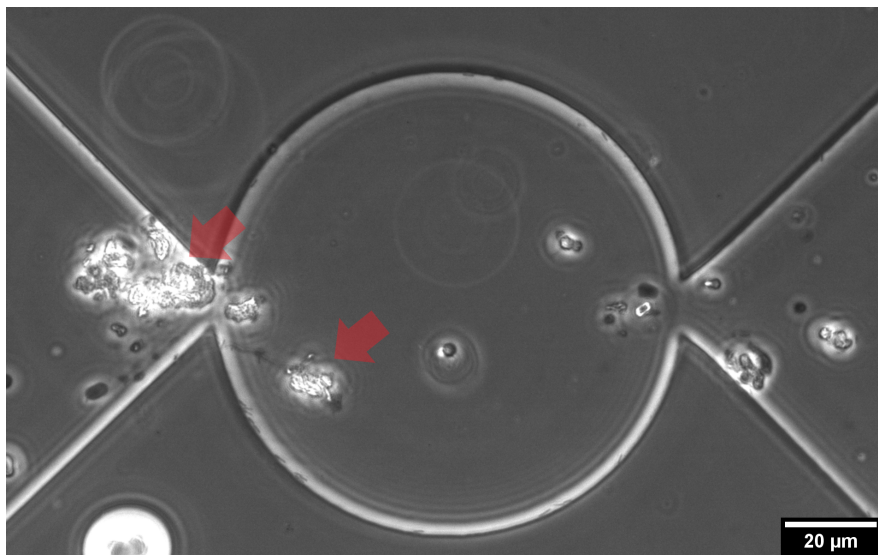


Figure 4.12: Platform for bacterial culture: design N° 3 - bacteria in the culture chamber. Microscopic picture acquired during a test of a microfluidic device for single bacteria culture. The image shows we were able to insert bacteria in the device and that they reached the central culture chamber. Right red arrow points a bacteria colony growing in the central chamber while left red arrow points to a big clog of bacteria that makes it difficult for others to reach the culturing chamber.

While using this design I had successfully demonstrated bacterial growth, there are still two main problems to be addressed to obtain a functional microfluidic platform:

- bacteria should preferentially be located within the specific culturing region in order to have reproducible experiments for comparative experiments;
- bacteria were found to aggregate at the narrowing between the channel and the culture chamber preventing bacteria from accessing the culture chamber.

I propose two solutions to address these problems:

1. coating the culture chamber with Poly-L-Lysine to promote bacterial adhesion;
2. further modification of the device geometry to direct bacteria in a specific zone of the culturing platform.

The following sections are dedicated to the designs explored to “force” bacteria to locate in a specific area of the microfluidic platform.

4.2.4 Double height culturing device

At the end of section 2.2.1 it has been described how microfluidic *culture wells* use gravity to confine bacteria in specific “deeper” areas (wells) of the device. Therefore, informed by an example found in literature [52], I investigated a microfluidic bacteria culture module with multiple heights. Following the protocol presented in [52] a double layer PDMS device was initially attempted. However, due to the difficulty in creating a thin ($< 1 \mu\text{m}$) bottom layer of PDMS and in precisely sealing two PDMS layers, I decided instead to fabricate a platform composed by a single block of PDMS in which the difference in heights is generated at the SU-8 mould level

Double layer SU-8 mould

While I initially designed and fabricated a double-layer SU8 mould, as a result of the national UK lockdown, I was unable to fabricate the complete PDMS device. The following fabrication steps, starting with the data collection for the mould profile (panel b of figure 4.17) were kindly completed by my colleague Kalum Thurgood-Parkes following the reopening of laboratories and under my remote guidance.

Given the difficulties in assembling a two-layer PDMS device, the difference in height has been recreated at the mould fabrication level. Figure 4.13 schematically shows the structure of the mould while the fabrication protocol is described in “strategy 4” of chapter 3.

The bottom layer consists of a square culture chamber $200 \mu\text{m} \times 200 \mu\text{m} \times 0.5 \mu\text{m}$. The cross-sectional area of this chamber is large and is thus prone to collapsing onto the substrate surface. To prevent this, an array of circular pillars was included within the chamber to provide mechanical stability. These pillars (which in the mould are actually “holes”) are

$20\ \mu\text{m}$ diameter and are spaced $40\ \mu\text{m}$ from the edges of the chamber and $30\ \mu\text{m}$ from each other.

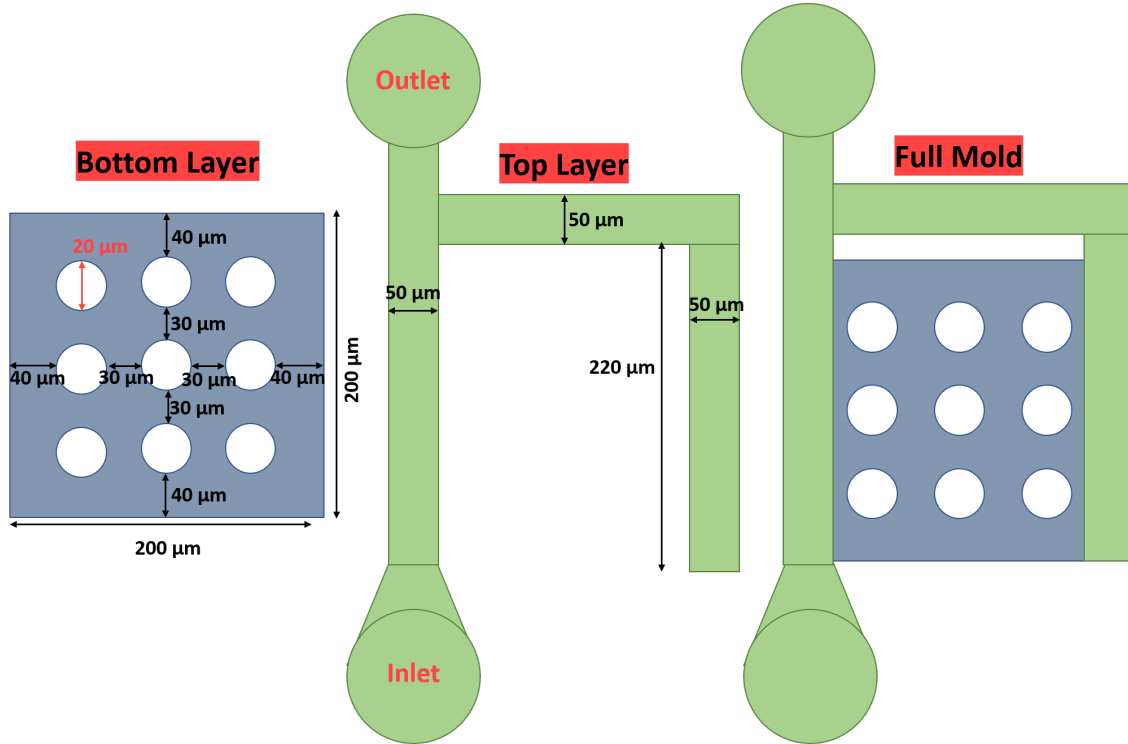


Figure 4.13: Double layer SU-8 mould: schematic design. From left to right: design of the bottom SU-8 mould and relative dimensions, design of the top SU-8 mould and relative dimensions, final complete design with bottom and top designs assembled together as they should appear after development. White circles are areas left unexposed (holes in the mould). The bottom layer is $\simeq 0.5\ \text{nm}$ high and the top one is $20\ \mu\text{m}$.

0.5 μm thick SU-8 layer: spin-coating optimisation

The first step for the fabrication of the bottom SU8 layer of the mould was the optimisation of a spinning protocol; the height of this layer is critical to ensure a single bacterial monolayer. Results of the optimisation are summarised in the graph of figure 4.14. It was found that at a spin speed of 6000 rpm, the resulting SU-8 layer was around $0.78\ \mu\text{m}$ thick which is sufficiently thin to allow for monolayer bacterial growth. I note, 6000 rpm is close to the maximum spin speed of the machine and while working close to the smallest height declared for the SU-8 2000.5, the photoresist final profile varies imperceptibly even with a substantial increase in spinning speed.

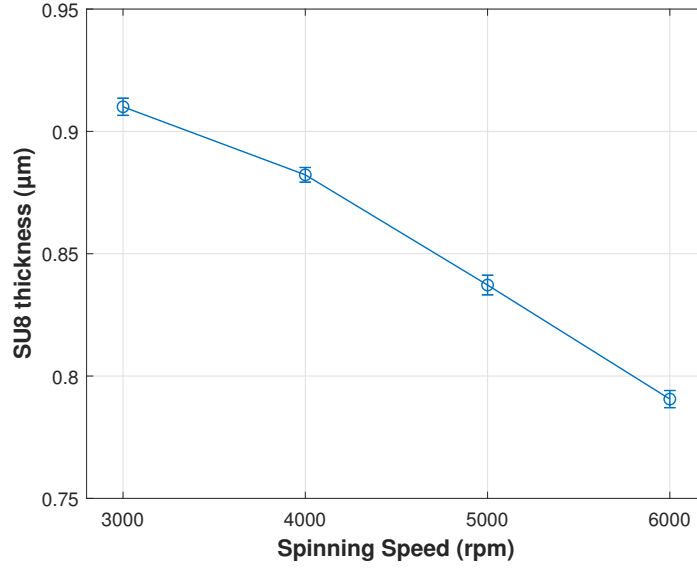


Figure 4.14: 0.5 μm thick SU-8: spin curves for different spin speeds. The higher the spin speed, the thinner the film, as expected. Each test consists of two spinning steps: the first is kept at the same speed for all the tests while values in the graph refer to the second spinning step. First step is at 500 rpm for 15 s for all the tests. The duration of the second step is 30 s for all the tests. Error bars refer to the standard error over five different locations across the sample being scanned by the stylus profiler.

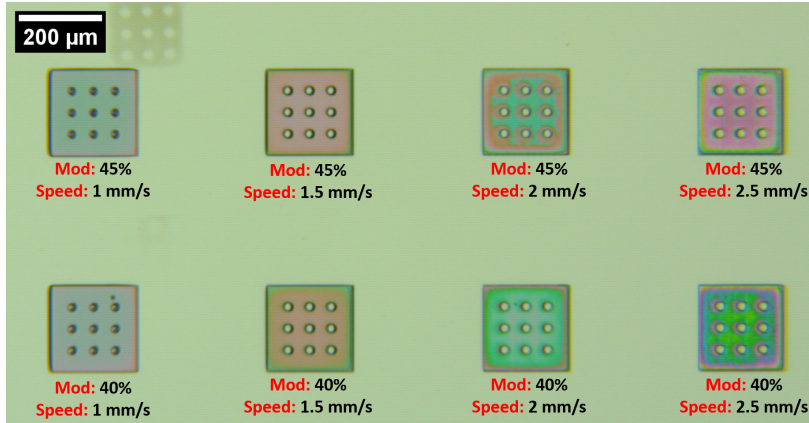
0.5 μm thick SU-8 layer: exposure optimisation

When fabricating a mould as the one shown in figure 4.13 it is important to finely optimise the exposure parameters for the bottom layer. If the photoresist layer is globally overexposed, the “holes” in the mould may appear partially or completely closed after development. The lithography optimisation protocol for the 0.5 μm thick SU-8 layer consisted in repeating the exposure of the mould varying the DLW parameters as follow:

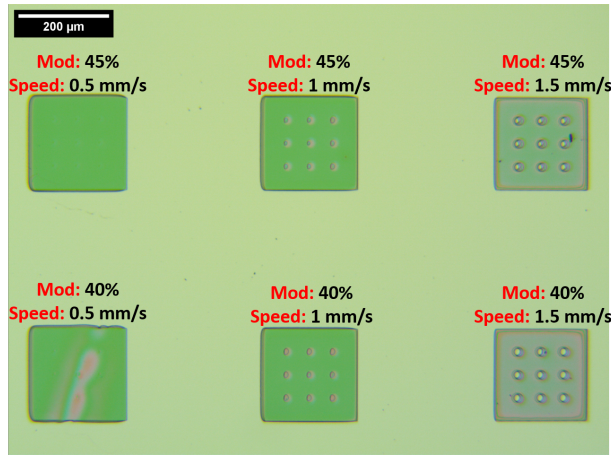
- **Laser power:** 40% – 45%;
- **Writing speed:**
 1. Test N°1: 1 mm/s – 1.5 mm/s – 2 mm/s – 2.5 mm/s ;
 2. Test N°2 (to confirm the results): 0.5 mm/s – 1 mm/s – 1.5 mm/s ;
- **Δz :** +1 μm .

Microscopic images resulting from the optimisation tests are shown in figure 4.15. The optimised protocol in table 3.6 is the result of this test: *Laser Power* = 40%, *Writing speed* = 1.5 mm/s and Δz = +1 μm .

The exposure of the bottom layer also includes three markers to complete a three point alignment of the upper SU8 layer as explained in chapter 3. These markers were positioned close to the bottom left, bottom right and top left corners of the silicon wafer, and centred 2.5 mm the die edge. Each arm of the crosses are 100 μm long and 10 μm thick and were written with a laser power of 80% and a writing speed to 0.5 mm/s .



(a) *Exposure optimisation Test N°1*



(b) *Exposure optimisation Test N°2*

Figure 4.15: $0.5 \mu\text{m}$ high SU-8 layer: lithography parameter optimisation. Microscopic images resulting after baking, exposure and development of a mould reproducing the bottom layer of the mould for the bacterial culturing device. From the first test (panel a) the exposure at 40% laser power (Mod.) and 1.5 mm/s writing speed appeared the one receiving the most appropriate dose. Results of the second test (panel b) confirm this result. Value of Δz ($\Delta z = +1 \mu\text{m}$) is left unchanged between the test.

Top layer and final mould

For the upper SU-8 layer the optimisation of the lithography parameters is less critical and after a crude dose trial, the exposure parameters detailed in table 3.7 were used. The height of this photoresist layer was measured with the DektakXT Stylus Profiler following method N°2 described in figure 3.6. The resulting profile is shown in figure 4.16.

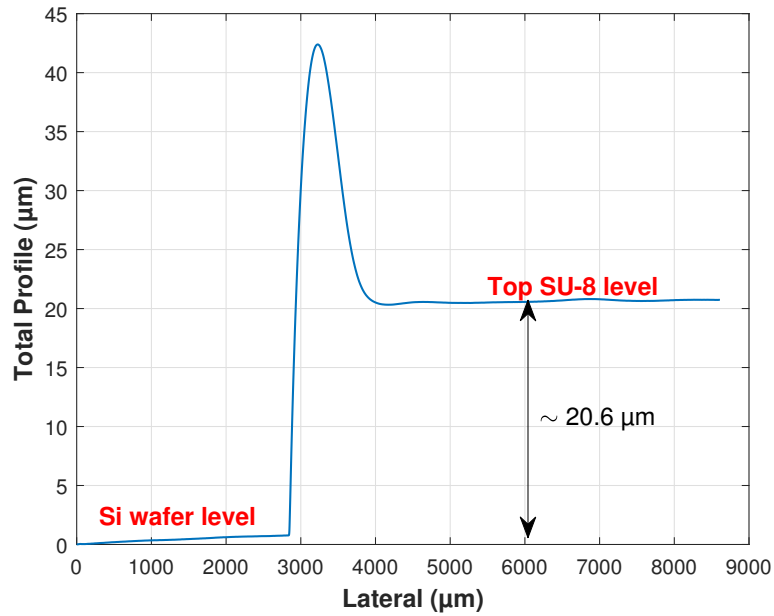


Figure 4.16: 20 μm thick SU-8 layer: stylus profile. Exported data from the DektakXT Stylus Profiler: the 0 μm value for the “Total profile” corresponds to the top surface of the Silicon Wafer; passing from the bare silicon wafer to the SU-8 surface the profile shows a positive peak due to the edge bead. The total profile flattens in proximity of the centre of the sample with an average value of $\simeq 20 \mu\text{m}$ (marked in the graph) that corresponds to the height of the photoresist layer.

The resulting complete mould is shown in panel a of figure 4.17. I note, while the upper channels are aligned with the culture chamber, the alignment is not perfect.

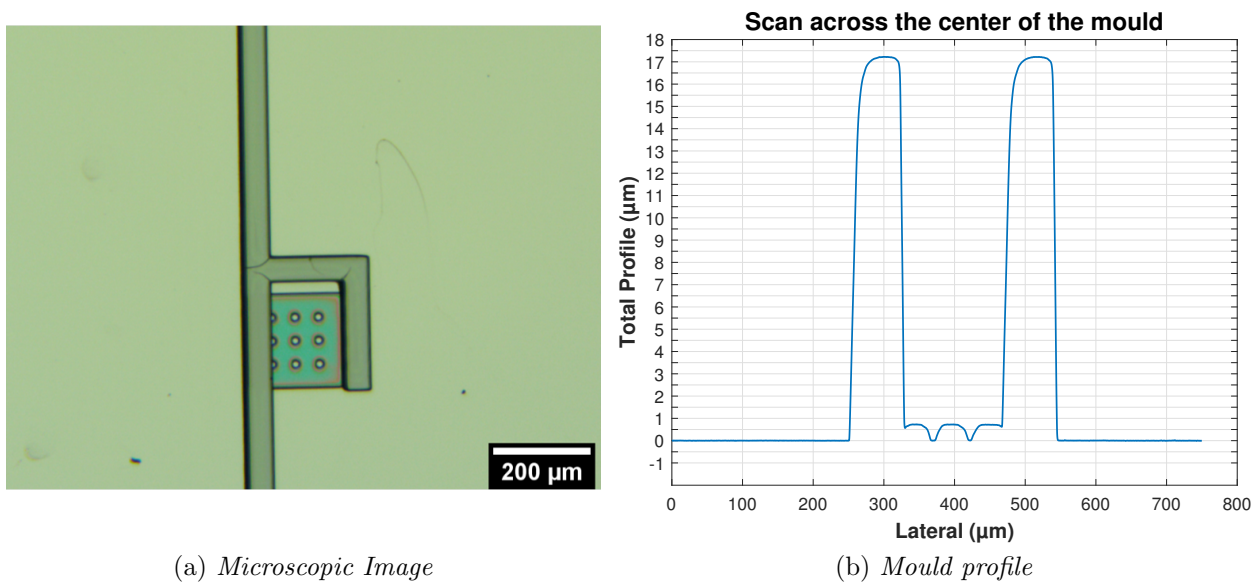


Figure 4.17: Double layer SU-8 mould. Microscopic images of the mould shows an inaccurate alignment of the two layers (a) but the profile of the mould confirms that the overlap is enough to permit a correct replica moulding (b).

The profile of the mould (obtained using the DektakXT Stylus Profiler and scanning across the top channels and bottom chamber) is shown in panel b of figure 4.17. Both layers are slightly thinner than expected (upper SU8 layer measured $\simeq 17 \mu m$, expected $\simeq 20 \mu m$; lower SU-8 layer measured $\simeq 500 nm$, expected $\simeq 800 nm$). I believe this is likely due to the hard baking step that, completing the photoresist cross-linking process it may also causes a slightly shrinkage of the exposed features I note this does not compromise the eventual success of the experiment. Having a thinner bottom layer is, indeed, more favourable for bacterial mono-layer growth.

Following the protocol described in section 3.4, a PDMS replica of the two-layer SU8 mould was prepared, as shown in picture 4.18. Unfortunately, following multiple attempts at bonding the PDMS to the glass substrate, it was found that the culture chamber repeatedly collapsed. This was probably due to the large cross sectional area of the culture chamber that is not well compensated by the 9 pillars either because they are too few/ too small to support the whole bottom chamber or by the incomplete opening of the holes in the mould exposure step. While it would have been desirable to optimise the geometry and fabrication of the SU8 mould, the impossibility of returning to the laboratory in person meant the research had to be halted.



Figure 4.18: Double layer SU-8 mould: PDMS replica. Microscopic images of the PDMS replica before PDMS-glass bounding step.

4.3 Bacterial cell counting

At this point data collected for the first two experiments are enough to develop and test a MATLAB algorithm able to process microscope images for automated counting of bacteria inside the device. Two images from the dataset used to develop this algorithm are shown in figure 4.9. The full dataset comprises 240 images of the same area of the device taken every 3 minutes for a period of 12 hours following inoculation of the device.

4.3.1 Binary image creation

To accurately count discrete objects (here, bacteria) within a microscope image, it is fundamental to precisely distinguish relevant objects from the background. Here, this was achieved by developing an algorithm in MATLAB consisting of multiple steps that were applied to each individual image as detailed below.

1. **Image acquisition and cropping:** image is acquired in its original “*.tif” format and cropped to the area of interest. Sizes for the cropped image are established manually for the first image of the dataset (t=0) and kept the same for all subsequent images;
2. **Binary mask creation:** from the cropped image, a black and white image is created following Otsu’s method for the threshold identification. Briefly, this defines a global intensity threshold to assign to each pixel in the image either a black colour (intensity = 0) or white colour (intensity = 1). The threshold is chosen to maximise the inter-class variance or to minimise the intra-class variance. A mask is then obtained from the binary image where white pixels correspond to the areas enclosed in the microfluidic device;
3. **Extraction of region of interest:** the mask is used to filter the original cropped image to effectively “crop” the pixels outside the area of interest, where it is not necessary to complete the subsequent operations (here, regions outside of the microfluidic channel). In addition, an image is created from the binary mask that only shows the edges of the area of interest i.e. the walls of the fluidic channel. This region of interest image is used in all subsequent steps;
4. **Pixels value inversion:** values of the pixels are inverted to have white objects on a dark background. This step simplifies following operations;
5. **Background non-uniformity correction:** is achieved through operation of the “tophat” function. This requires the following inputs.
 - **Grey-scale image** to correct for non-uniformity;
 - **Structural element** this is a logical matrix where the elements ascribed a number 1 form a specific shape laying on elements marked with the number 0 (the background). This shape must be similar to the one of the objects (elements in foreground) in the original image. For our case, where bacteria are the objects, a circular shape of 6-pixels radius was found to be the most appropriate.

The *Top-hat* function returns an image containing those objects (bacteria in our example) that are smaller than the structural element and brighter than their surrounding, performing the following two consecutive operations on the input image.

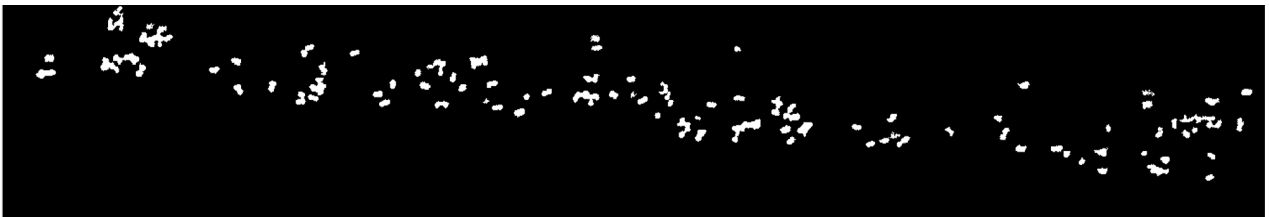
- (a) **Aperture** to estimate the background. It consists of an *erosion* operation followed by a *dilation*. The *erosion* removes from the image all the elements having a dimension smaller than the structural element, the subsequent [dilation] “dilates” the feature that are left in the image to better approximate the background close to the removed objects (bacteria);
 - (b) **subtraction** of the background estimate (opened image resulting from the previous step) from the original image.
6. **Binary image creation:** after background correction, the procedure of step N° 2 is repeated on the image. From the resulting binary image, the edges extracted during step N° 3 are subtracted.

7. **Binary image correction:** after the creation of the binary image, there are white features that are too small to be attributable to a bacterium. Therefore, all the white areas smaller than a minimum value of pixels ($Min.area_{ip}$) are deleted. After repeating this step with different values of $Min.area_{ip}$, on the the basis of visual comparison between the binary images and the corresponding original images of the dataset, its value was set to be $Min.area_{ip} = 20\ pixels$. All white areas smaller than $Min.area_{ip} = 20\ pixels$ are thus deleted. $Min.area_{ip}$ corresponds to a unique value for a specific dataset.

Steps from 1 to 7 and respective results in term of images obtained are summarised in figure 4.20 while step 7 is briefly explained in figure 4.19.



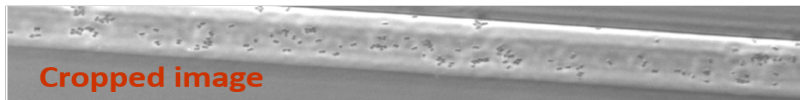
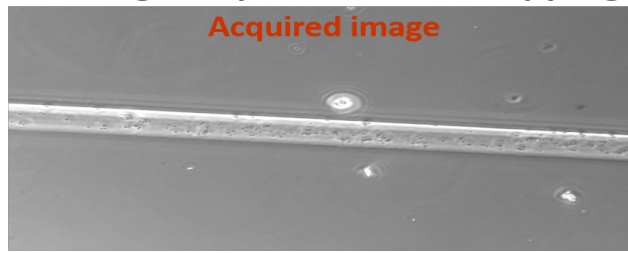
(a) *Binary image before correction*



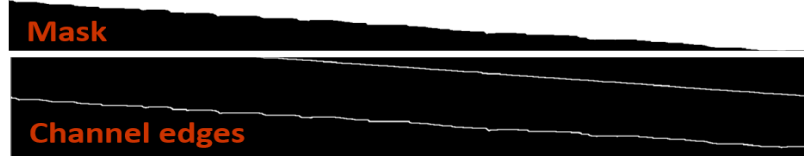
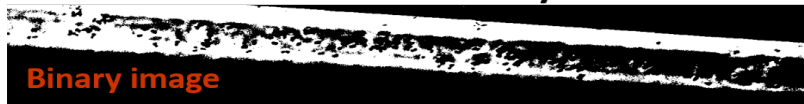
(b) *Binary image after correction*

Figure 4.19: Image processing algorithm: binary image correction. Red circles in panel (a) highlight white pixels areas too small to be attributable to a bacterium. Panel (b) shows the final binary image obtained after the “deletion” of white area smaller than 20 pixels ($Min.area_{ip} = 20\ pixels$). All the white areas potentially attributable to bacteria are still visible in panel (b). The choice of $Min.area_{ip}$ is extremely important for the success of the counting algorithm.

1. Image acquisition and cropping



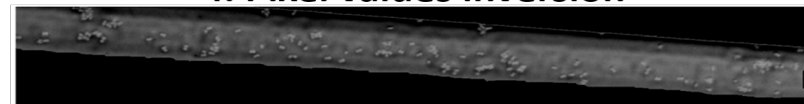
2. Creation of a binary mask



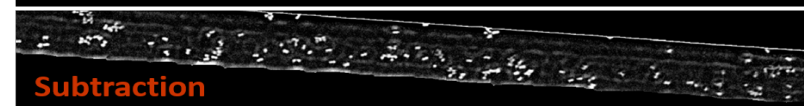
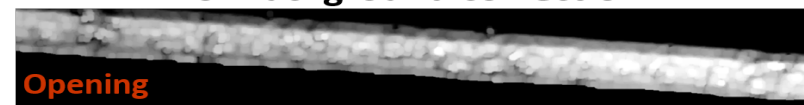
3. Region of interest



4. Pixel values inversion



5. Background correction



6 & 7. Final binary image

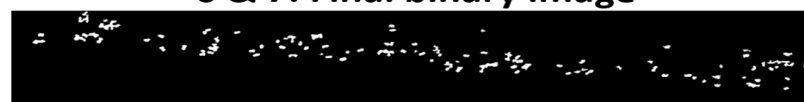


Figure 4.20: Image processing algorithm: flow chart and results. Results shown step after step. Mask of step N° 2 is used to extract the “Region of interest” from the original cropped image. In step N° 5 image resulting from the “Opening” is subtracted from image resulting from step N° 4 and to obtain the “Final binary image”, “Channel edges” extracted in step N° 2 are subtracted after “Background correction”.

4.3.2 Bacterium area estimate and bacteria counting

In the final binary image (see bottom panel of figure 4.20) only bacteria appear as white pixels and the number of individuals is estimated as follow.

$$N^{\circ} \text{ bacteria} = \frac{N^{\circ} \text{ white pixels}_{\text{binary image}}}{\text{Single bacterium area}}$$

Where *Single bacterium area* is the number of white pixels that forms a bacterium. Strategy developed to calculate the average area of a bacterium is described in the following section.

Area estimate

As a first evaluation, the average area of one bacterium was calculated by manually cropping a single bacterium for some of the final binary images resulting from the dataset and counting the white pixels composing the cropped shape. For each image, 10 bacterium were selected. Where possible, for each image a different bacterium was selected. Given the tendency of bacteria to form dense colonies, the identification of a single microorganism in the images is not always immediate. For this reason the area of a single bacterium was found to be highly variable, even within the same image. Once extracted, the average of the ten single bacterium areas is calculated for each image. The overall average area of a single bacterium is estimated as the global average of the values previously calculated for each image. The raw data used for this calculation are shown in graph of figure 4.21.

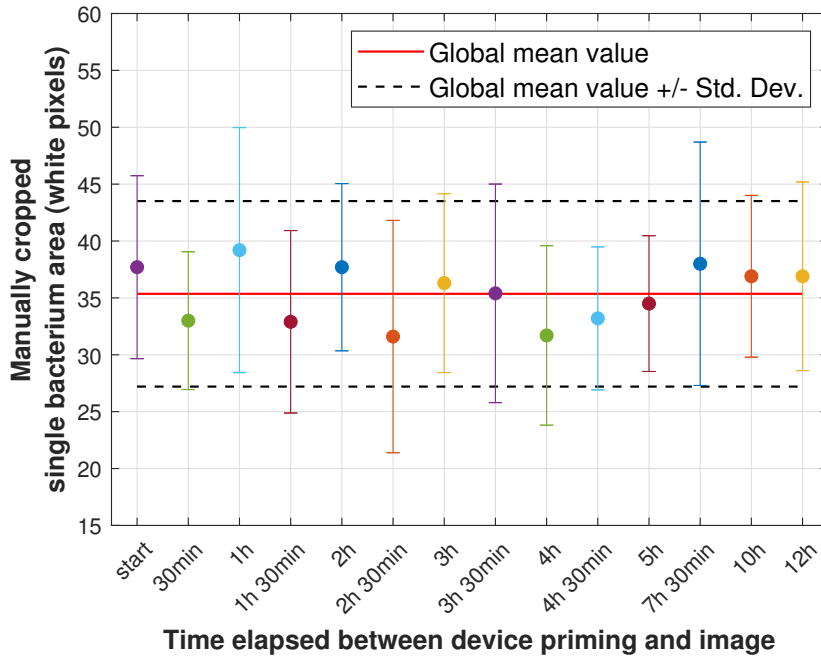


Figure 4.21: Single bacterium area estimate: first evaluation. Each point in the graph represents the average value of the single bacterium areas calculated for each selected image. A bacterium is manually cropped after visual evaluation, 10 times for each image. Error bars show a rather high variability. Red horizontal line marks the global average calculated over the points and considered as the global average area of a single bacterium.

As shown in figure 4.21, the global average area used to estimate the area of a single bacterium corresponds to an area of $35.36 \pm 8.15 \text{ pixels}$, approximately $14.83 \mu\text{m}^2 \pm 3.39 \mu\text{m}^2$. This is the area of a circle with radius $\sim 2 \mu\text{m}$ that is a fair approximation of the projection of a bacterium on the glass slide lying at the bottom of the microfluidic device. In fact, bacteria cells are typically oval or spherical in shape with a length of $0.5 - 5 \mu\text{m}$ whose projection is a circle or an ellipse with radius or the axes of few micrometers.

To optimise the estimate of the single bacterium area so as the procedure becomes faster and adaptable to subsequent experiments, the results shown in figure 4.21 was also assessed using the built-in MATLAB function *regionprop*. This function identifies all objects consisting of 8-connected pixels in a binary image i.e. all the white areas consisting of at least 8 neighbouring pixels are counted as a single object and their areas are returned.

Ideally the “objects” in our images dataset are only bacteria but identifying a single bacterium is hard with *regionprop* function. Specifically, colonies of bacteria are returned as individual “objects” so the output areas can not be directly associated with that of a single bacterium. The average value of the areas returned using this function for each image, is always around twice the global mean value estimated when manually cropping single bacterium (corresponding to $97.07 \pm 6.00 \text{ pixels}$). The graph shown in figure 4.22 visually summarises these results.

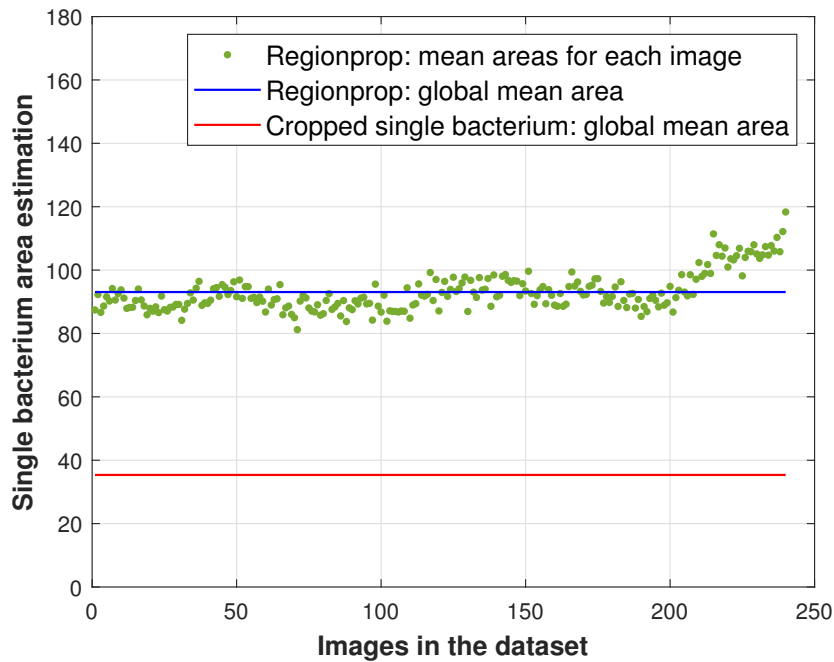


Figure 4.22: Single bacterium area estimate with *regionprop* function: average values. Green points are the average value of the the areas identified by the *regionprop* function for each image. The global average over these values is shown as a blue horizontal line. The red horizontal line indicates average area of a single bacterium obtain from previous evaluation (“manually cropped single bacterium”).

The smallest area returned by *regionprop* is generally not attributable to a bacterium. In fact, for most of the images the smallest object size was found to be equal or close to 20 pixels

(figure 4.23). These objects are “artefacts” introduced at “step 7” of the image processing protocol described in section 4.3.1 and figure 4.19.

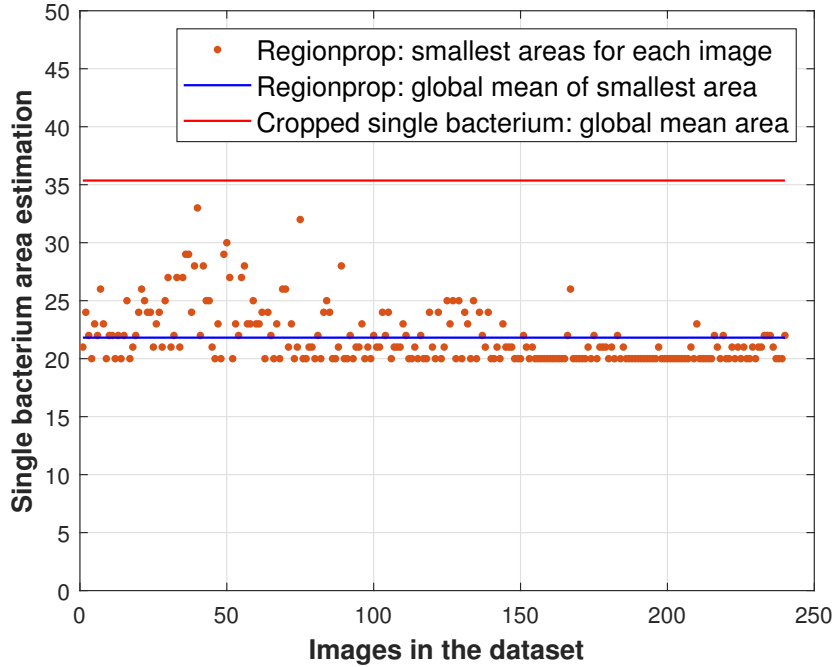


Figure 4.23: Single bacterium area estimate with *regionprop* function: minimum values. Orange points are the minimum values of area identified by the *regionprop* function for each image. The global average over these values is shown as a blue horizontal line. The red horizontal line indicates average area of a single bacterium obtain from previous “manual” evaluation (“manually cropped single bacterium”).

My solution to improve the evaluation of the area of a single bacterium follow these steps for each binary image of the sequence:

1. *regionprop* function is run on a single image;
2. the minimum value among the returned areas is calculated ($Min. area_{rp}$);
3. the minimum value is compared with the minimum value imposed at “step 7” of the image processing protocol in section 4.3.1 ($Min. area_{ip}$):
 - if $Min. area_{rp} \geq Min. area_{ip} + (0.5 \times Min. area_{ip}) \rightarrow$ *regionprop* is not run on following images and the area of a single bacterium is estimated as follow:

$$Area_{bacterium} = Min. area_{rp}$$

- if $Min. area_{rp} < Min. area_{ip} + (0.5 \times Min. area_{ip}) \rightarrow$ the average of the returned areas is calculated and stored, steps 1, 2, 3 are repeated for subsequent images.

If the condition at the first point of step N°3 is never satisfied, the area of a single bacterium is estimated as follow:

$$Area_{bacterium} = \frac{Area_{rp}}{2}$$

where $\overline{Area_{rp}}$ is the global average value calculated over the average areas returned for each image.

This algorithm is based upon the implementation of the build-in Matlab function *regionprop* to limit user intervention and thus systematic errors. In most of the images collected during the bacterial culture experiment in the microfluidic device (eg figure 4.10), the majority of the bacteria are very close to each other. Therefore, when these images are given as inputs to the *regionprop* function, after being converted into binary images, the objects returned by *regionprop* are colonies rather than single bacteria (see figure 4.22). Assuming that bacteria are all similar, the algorithm further investigates only the minimum area value returned by *regionprop* which, in the case of having at least one isolated bacterium in the device, should be a good estimation of the area of a single bacterium. However, I observed that the minimum area value often derives from an artefact introduced during previous image processing operations (see figure 4.23).

In fact, when creating the binary (black and white) images to be given as inputs to *regionprop*, all white regions composed of a number of pixels lower than a certain threshold are “deleted” to ensure that white objects correspond to bacteria and not to pixels introduced by any kind of noise (eg white “dots” introduced by uneven lighting)(see section 4.3.1). Such threshold is chosen by creating the same binary image for different threshold values and visually confronting them with the related image from the experimental dataset. This forces the smallest “white object” to be composed of a number of pixels equal to, or slightly higher, than the threshold itself, thus not being significant in the estimation of the area of a single bacterium. For this reason, the minimum area returned by *regionprop* is selected as the area of a bacterium only if it is sufficiently larger than the threshold value chosen when creating the binary image. The minimum area returned by *regionprop* is confronted with a threshold chosen by taking into account the entity of the artefact previously introduced and the estimation of the area of a bacterium based on the results in figure 4.21. Only if bigger than this threshold, the minimum area returned by *regionprop* is chosen as the area of a single bacterium, thus avoiding the risk that its value is affected by the aforementioned artefact. If this condition is not met for any images in the dataset, given the tendency of the bacteria to form groups of few cells (generally up to 10), the half of the average of the areas returned by *regionprop* for the entire dataset is chosen as best approximation of the area of a single bacterium.

In our case the condition is satisfied at image N° 40 (see graph in figure 4.23):

- $Min. area_{ip} = 20$ (see “step 7” in section 4.3.1);
- $Min. area_{ip} + 0.5 \times Min. area_{ip} = 30$;
- $Min. area_{rp} = 33$ at the image N° 40;
- **Single bacterium area = 33 pixels and the *regionprop* function is stopped running at image N° 40.**

As shown in figure 4.24 (first two bars), the area of a single bacterium estimated automatically compares well with the area calculated manually (figure 4.21).

To further verify the accuracy and generality of the method for bacterium area calculation, the algorithm was also tested on datasets obtained from different bacterial culture experiments; results are shown in figure 4.24.

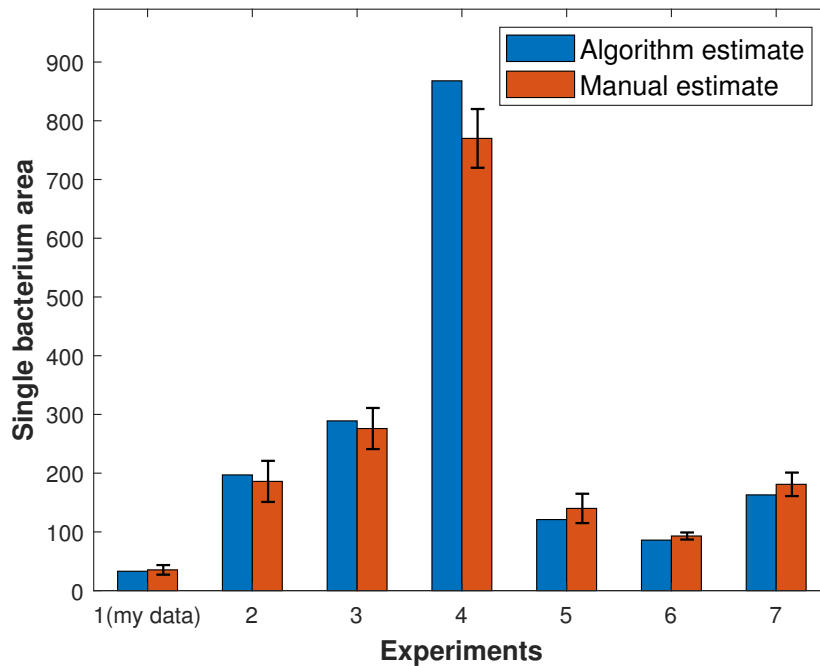


Figure 4.24: Single bacterium area: manual and automatic estimate comparison. The numbers in the vertical axis correspond to the total number of white pixels composing the shape of a bacterium in the binary image. First couple of bars refer to my experiments while the rest of the bars refer to experiments carried out by Fatima Yendybayeva as stated in the text. Each experiment constitutes a unique dataset.

The set of images used to extract the data of figure 4.24, were collected by Fatima Yendybayeva, a BSc student in the biology department of the University of York (academic year 2019-2020). These data were collected using *E. coli* cultured in a mother machine fabricated on an agarose substrate (see section 2.2.1 and figure 2.4 for further information). Binary images were generated adapting the procedure described in section 4.3.1. An important parameter to change when changing dataset is the value of $Min.area_{ip}$ set at “step 7” in the protocol described in the section 4.3.1. The manual estimate of the area of a single bacteria was calculated following the same procedure used to obtain the graph in figure 4.21 and the average value is represented in figure 4.24 with the respective error bar showing the standard deviation over all the measures.

Except for the experiment N°4 in figure 4.24, the area of a single bacterium returned by the algorithm falls within the confidence interval of the manually estimated areas. In all the experiments the difference between the average value of the manual estimate and the algorithm estimate never exceeds the 15% of the respective estimates. Hence the performances of the

manual estimate and the algorithm one are comparable but this latter is preferred because it is automated and less time consuming.

Bacterial cell counting

Once the number of white pixels composing a single bacterium has been estimated (single bacterium area), for each image the total number of bacteria can be extracted. Before proceeding with the analysis of the bacterial growth rate inside the microfluidic device, the performance of the cell counting algorithm was evaluated by comparing cell count obtained automatically with those calculated manually. This comparison was performed using 13 images within the data set, corresponding to one image per hour, in which bacteria were counted manually 5 times. Results from the comparison are shown on the bar plot of figure 4.25

Taking into account counting errors, the difference between the number of bacteria counted manually and automatically was less than 100 for each image. The general trend is bacterial counting is also maintained over time: the number of bacteria counted manually is consistently around 70 more than the number of cells calculated automatically. This is likely due to the presence of a bacteria colony growing extremely close to the channel walls that can be “deleted” during the image processing procedure. In fact, changing the dataset, this difference decreases and the overall trend of having an almost constant difference between the two counting methods does not repeat systematically (figure 4.28).

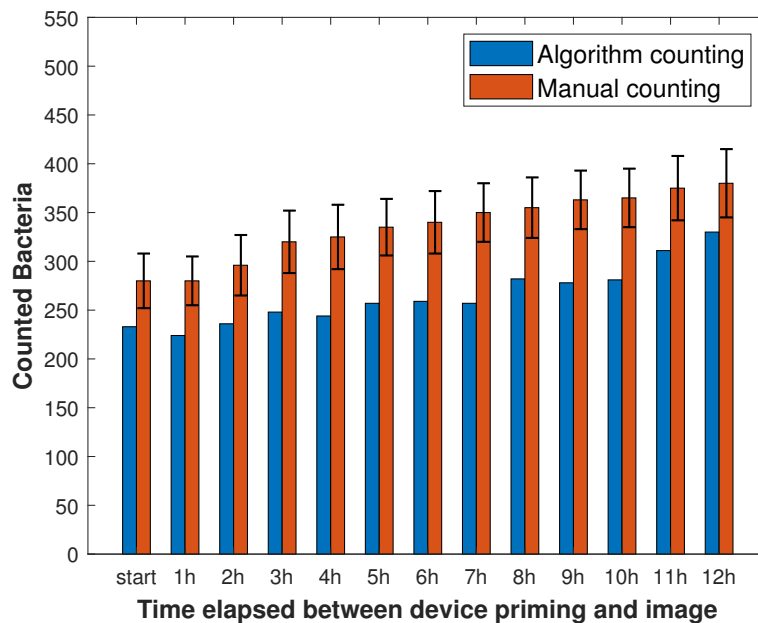


Figure 4.25: Manual and automatic counting comparison.

As already visible from figure 4.25, over the whole 12 hour period bacterial growth is observed but is slow. Graph in figure 4.26 visually summarises the overall growth of the population in the device. The red line shows a polynomial curve fitting of second degree which helps to visualise the trend. The number of bacteria counted in the final image (12 hours after

priming) compared with the number counted on the first image (right after priming) shows that the population has increased less than 50% in respect to the initial number of bacteria.

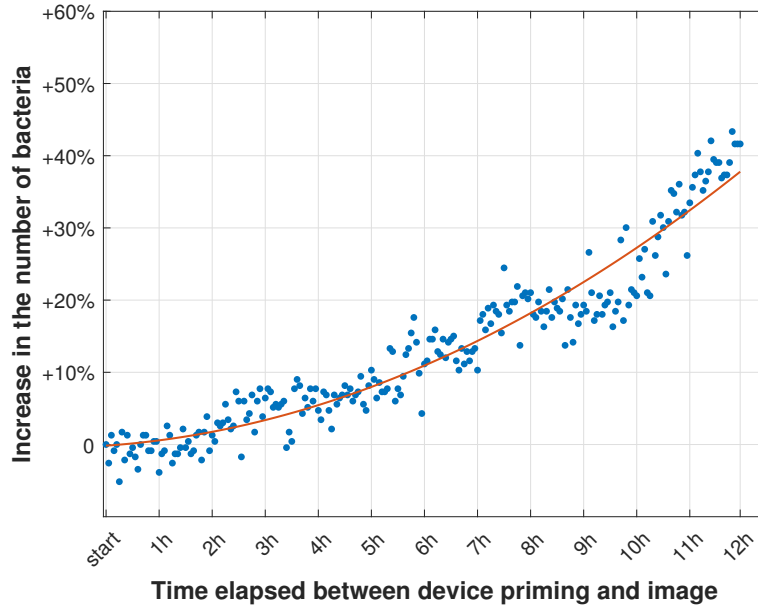


Figure 4.26: Experimental results: *E. coli* W3110 growth in the device. Increase in the number of bacteria counted by the algorithm compared to those counted immediately after incubation.

When bacteria are cultivated in a batch culture (closed system), as generally happens in laboratory, their typical growth curve looks like the one in figure 4.27.

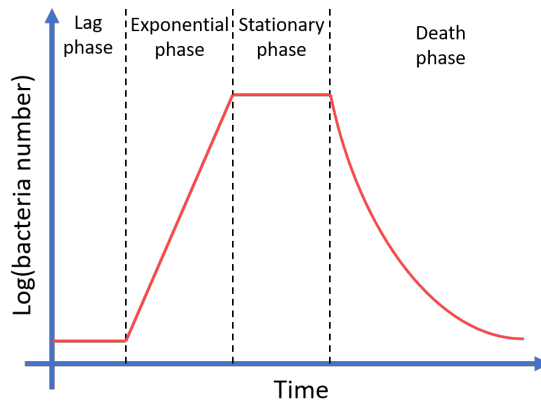


Figure 4.27: Bacterial reference growth curve in batch culture. When inoculated in a fresh culture, bacteria, after an initial phase needed to adjust to the new environment (*lag phase*), start dividing via binary fission (*exponential phase*) and continue dividing as long as nutrients are available. Once the waste products outweigh the nutrients or the space available for population growth becomes limited or the accumulation of harmful metabolites, population growth stops (*stationary phase*), eventually secondary metabolites are produced in this phase. If the incubation continues after this phase the population declines (*death phase*).

Analysing the graph in figure 4.26 we can affirm that bacterial growth in the device, never reached the exponential phase. In fact, as reported by Micha Peleg and Maria G. Corradini

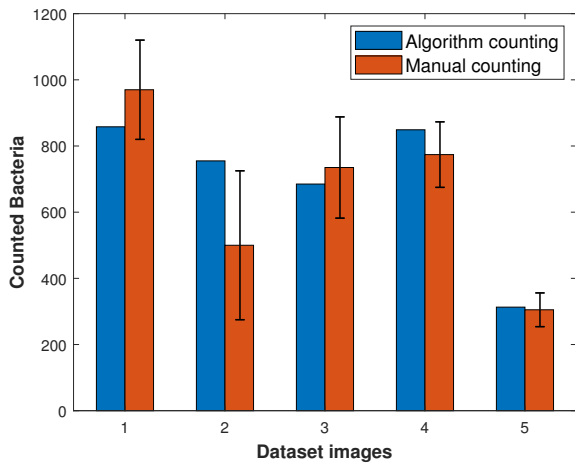
[78] commonly the *lag phase* (see figure 4.27) is considered concluded when the growth reaches 50% or 100% from the starting number of bacteria. It is excluded that bacteria may have been inoculated into the device with a concentration such as to have already reached the death phase. In fact, the concentration chosen for the incubation of *E. coli* ($OD_{600} = 0.5 - 1$) is, by protocol, associated with the *exponential phase*. A *lag phase* longer than 12 hours is anomalous in a closed system with optimal growth conditions.

From an initial analysis the cause of the behaviour in the device is attributed to the temperature of the room where the device is located, at least ten degrees below the 37°C , optimal for *E. coli* growth. Furthermore, as the channel collapsed on the glass substrate, the volume of the device is not known and it is thus not possible to estimate the bacterial concentration in the area of the device captured by the processed images.

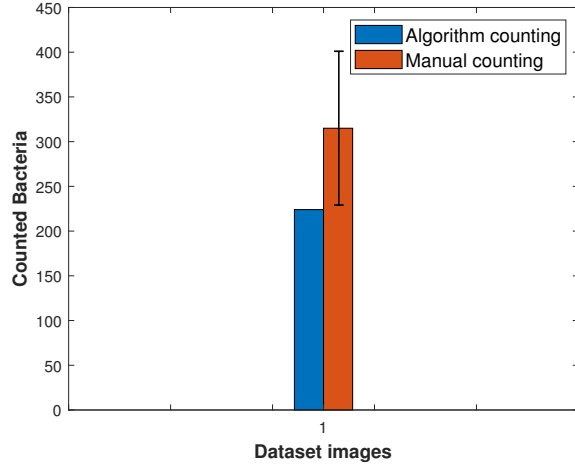
While an attempt to repeat bacterial growth at 37°C was attempted (see figure 4.12), a dense colony of bacteria blocked the entrance to the central culture chamber, where the objective of the microscope for the acquisition was focussed. Furthermore, images show a high bacterial mobility rather than a colonisation of the device.

To confirm that the performances of the counting algorithm do not depend on the dataset, the comparison between manual and algorithm counting was repeated using different datasets. Results from these comparisons are shown in figure 4.28, the set of images used is the same used to extract data in figure 4.24. Data in figure 4.28 were extracted following the same procedure for the ones in figure 4.25 and confirm that, taking in consideration the confidence intervals of manual counting data, the number of bacteria returned by the the manual and the automated counting almost coincides. Without taking in consideration the confidence interval, the average difference corresponds to the 13% of the relative estimates and only for image N°2 in panel a of figure 4.28 and image N°2 in panel f of figure 4.28 the difference reaches the 50% of the relative estimates.

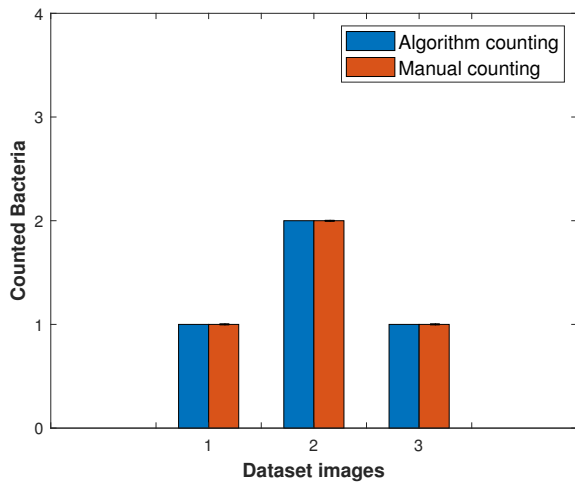
When the cell counting algorithm is needed to evaluate the bacterial growth inside a microfluidic device, the consistency of the results is important while an absolute accuracy is preferred but not required. This is clear when analysing results in figure 4.26; here, data distribution correctly shows an overall increase in the number of bacteria but the presence of outliers indicates that the number of “counted bacteria” is not exact. However, this does not prevent a satisfactory estimate of growth rate. The area of a single bacterium is estimated once for the entire dataset and its estimate is generally based on the processing of some if not all the images within the dataset. For this reason, the evaluation of bacterial growth rate is not substantially compromised by the specific value of the single bacterium area. It should be noted, changes in the the binary images over time (e.g. a change in the illumination) will introduce additional white pixels in the respective binary image leading to errors in the estimation of growth rate.



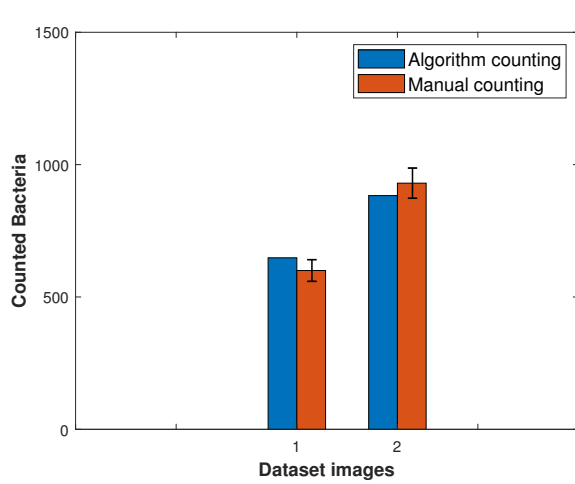
(a) *Experiment 1*



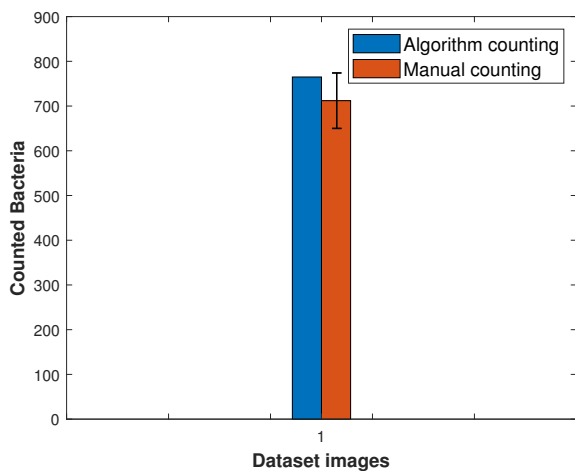
(b) *Experiment 2*



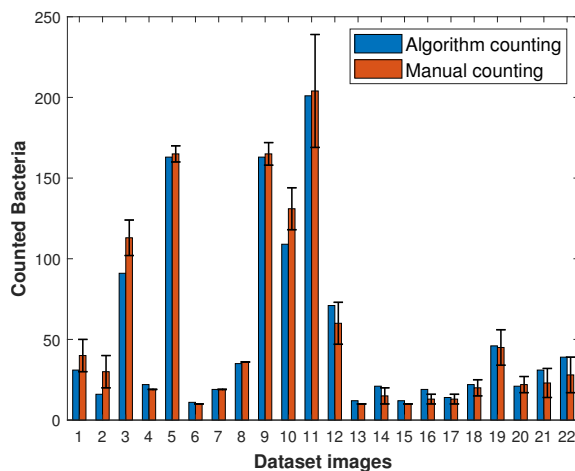
(c) *Experiment 3*



(d) *Experiment 4*



(e) *Experiment 5*



(f) *Experiment 6*

Figure 4.28: Manual and automatic counting comparison on additional datasets. Experiments related to the data shown were carried out by Fatima Yendybayeva as previously stated. Each experiment constitutes a dataset that is composed by images obtained using the same parameters at the binary image creation step.

Before proceeding with the section dedicated to COMSOL simulations I list below the main steps of the overall protocol developed for the fabrication of a single bacterial species culture microfluidic platform integrated with growth monitoring at the single cell level.

1. **PDMS device fabrication:** replica moulding with DLW as lithography technique;
2. **device priming and bacteria loading:** in a device primed with liquid medium bacteria are seeded after being appropriately cultured and diluted;
3. **bacterial culture in the device and image acquisition over time:** an inverted microscope is focused toward a specific area of the device and a connected bright field camera is set to acquire subsequent pictures over time;
4. **image processing and bacteria counting:** the acquired images are converted in binary images where the average area of a white bacterium is estimated and used to count how many bacteria does the total of white pixels of each image correspond to.

Chapter 5

COMSOL simulations

This section provides a deeper look into fluid-dynamics inside microfluidic devices proposed as platforms for bacterial culture. This is achieved using computational models to model the key fluid-dynamic phenomena that take place within microfluidic devices. First, I give a physical explanation to the difficulties encountered in priming some of the proposed chip designs, including a comparison between the design shown in figure 4.6 and that in figure 4.9). Secondly, I show a simulation of the fluid flow within the successfully primed design (figure 4.9) and in the “double-height” device of figure 4.18. The models were implemented in COMSOL Multiphysics 5.5 considering water instead of *Lysogeny Broth*. In fact, giving the concentrations of the powders dissolved in water to formulate the broth (see last section of chapter 3), the viscosity of the latter can be considered in first approximation equal to that of water.

The COMSOL computation flow dynamics (CFD) package solves the Navier-Stokes equations for mass and momentum conservation that has the following form:

$$\underbrace{\rho \left(\frac{\partial \mathbf{u}}{\partial t} + \mathbf{u} \cdot \nabla \mathbf{u} \right)}_{\text{inertial}} = \underbrace{-\nabla p}_{\text{pressure}} + \underbrace{\eta \nabla^2 \mathbf{u}}_{\text{viscous}} + \underbrace{\mathbf{F}}_{\text{external}}$$

where ρ is the density and η the viscosity of the fluid, \mathbf{u} is the velocity vector, p is pressure and \mathbf{F} is a force vector. The finite element COMSOL software solves the equation for $u_x(y, z)\hat{x}$ with the fluid flowing in x direction, z indicating the direction vertical to the flow and y the transversal direction to the flow.

5.1 Priming difficulties and channel dimension: back-pressure

As briefly summarised in figure 5.1, I established COMSOL models to observe how the velocity field and the distribution of pressures in two of the microfluidic devices vary as the ratio between the width of the channel and the diameter of the inlet changes.

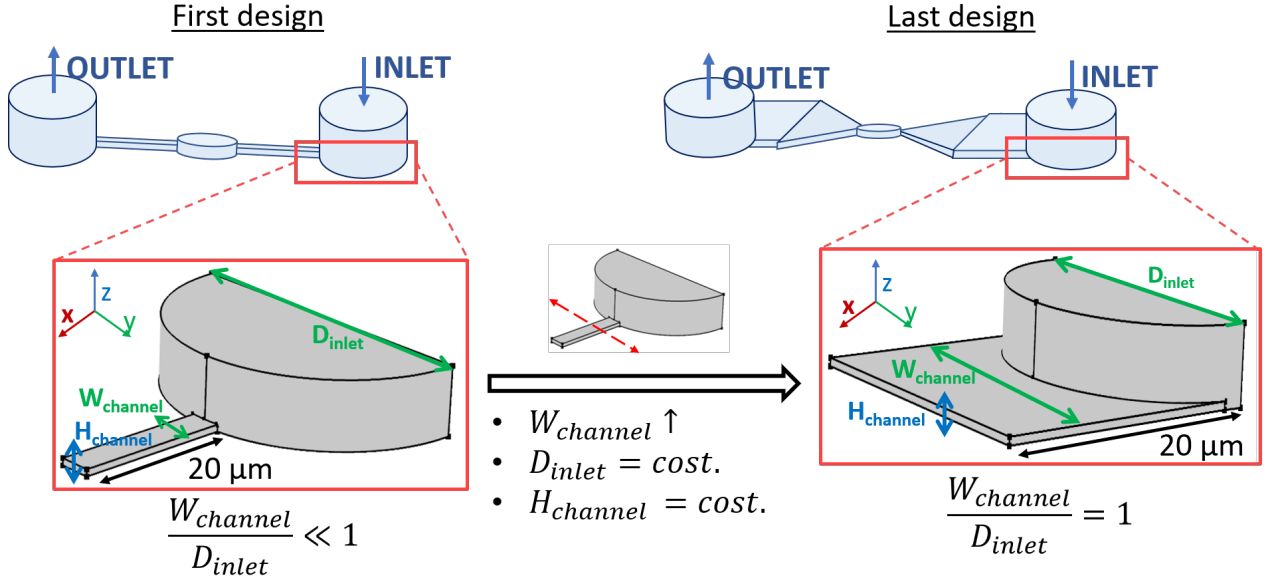
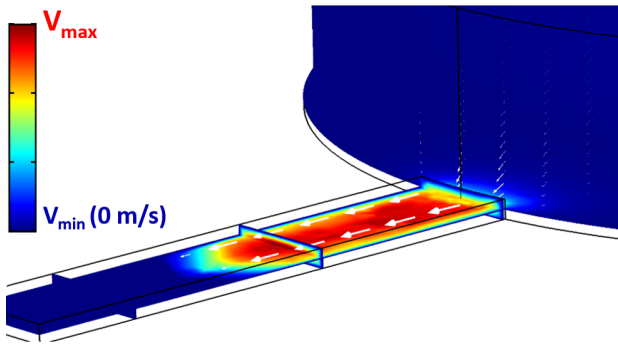


Figure 5.1: Device inlet modelling: geometry and setup. The simulation was run sweeping the value of the channel width, reproducing the solutions adopted in the laboratory to overcome the priming difficulties encountered with the “first design” and solved with the “last design”. The study focused on the first channel tract, close to the discontinuity introduced by the narrowing between inlet and channel. The outlet was positioned on the vertical free face of the channel.

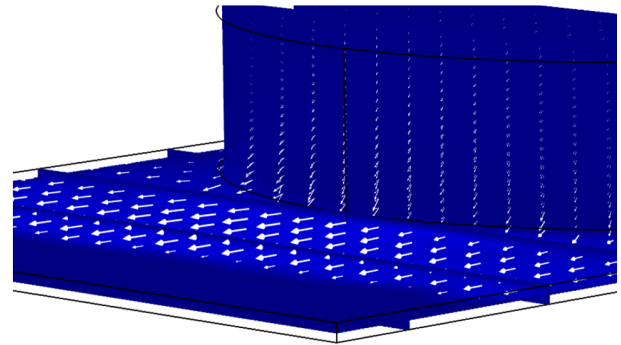
At the top face of the inlet port, the flow rate was set to be $Q_{inlet} = 10 \mu l/min$, as used in experiment, and the pressure at the outlet was set to a null value. Simulation results are shown in figure 5.2. When the liquid flows from the inlet into the channel, the fluid velocity increases while static pressure decreases following Bernoulli’s principle. This effect is more evident for smaller channel widths and translates into a pressure drop between the channel entrance and the device output. Such a pressure differential generates a high resistance to the flow that increases as the channel reduces in cross sectional area. This resistance is generally referred to as “back-pressure”. In fact, pressure is a scalar quantity and the term “back-pressure” is thus a misnomer, however, it gives the correct idea of restricting the flow in the desired direction.

Considering constant inlet dimensions and channel height, as in the “first design” in figure 5.1 and the “last design” in figure 5.1, the ratio $\frac{W_{channel}}{D_{inlet}}$ plays a critical role for the success of the device priming procedure.

As shown in figure 5.3, the pressure drop between inlet and outlet reduces as this ratio approaches 1 and so the resistance to flow also reduces. I believe that in the case of the “first design” in figure 5.1 this ratio is so small that the liquid can not flow into the channel.

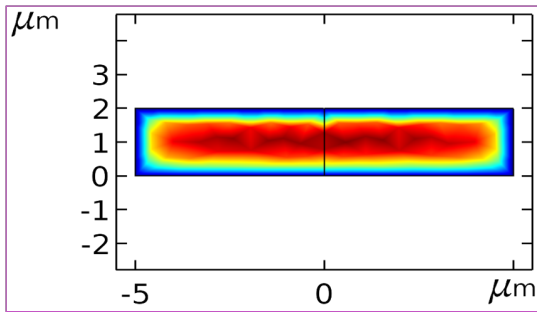


channel width \ll inlet diameter

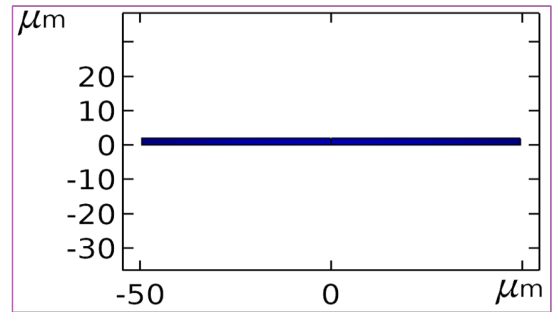


channel width = inlet diameter

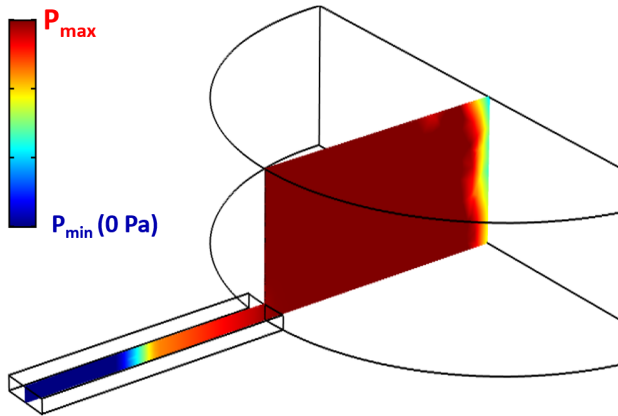
Channel entrance: vertical cross-section



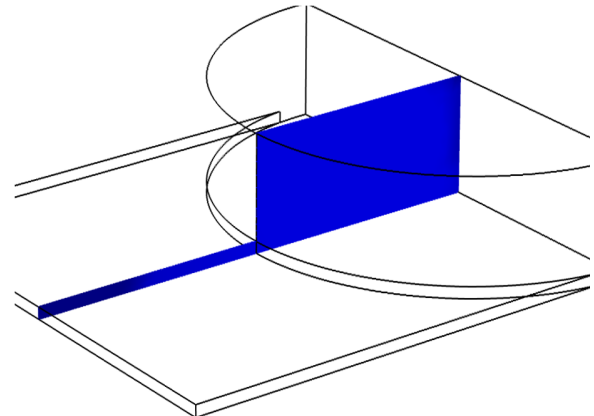
Channel entrance: vertical cross section



(a) Velocity - vertical and horizontal cross-sections



channel width \ll inlet diameter



channel width = inlet diameter

(b) Pressure - longitudinal cross-section

Figure 5.2: Device inlet modelling: COMSOL simulation results. Confronting images in the left column with images in the right column, it can be noticed that downstream effect of the constriction is greater for channel much smaller than the inlet. In left column panels, higher speeds are reached (a) and the pressure at the constriction (b) is higher in respect to the right panels. This translates into a more consistent load loss for the devices in the left panels. To help the visualisation the case of the first tested device ($\frac{W_{channel}}{D_{inlet}} = 0.005$) is not shown. Left panels show simulation results for the ratio $\frac{W_{channel}}{D_{inlet}} = 0.2$, right panels show simulation results for the ratio $\frac{W_{channel}}{D_{inlet}} = 1$

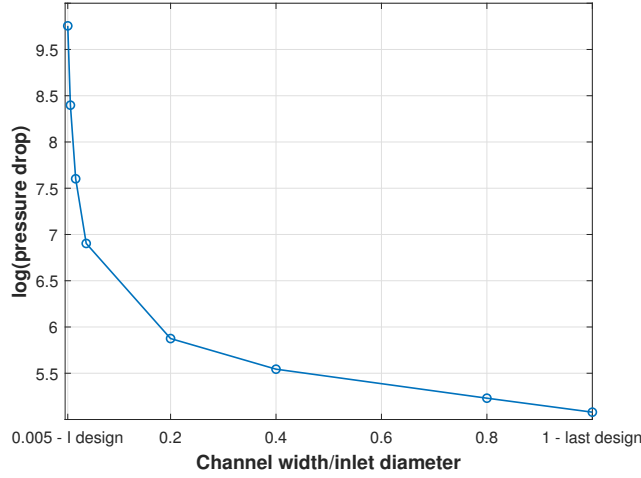


Figure 5.3: Device inlet modelling: pressure drop versus $\frac{W_{channel}}{D_{inlet}}$. The graph shows how the \log_{10} of the pressure drop changes in relation to the ratio $\frac{W_{channel}}{D_{inlet}}$. Pressure drop values are calculated as the difference in Pascal between the pressure at the channel entrance section and the pressure at the outlet (null pressure). Data are extracted from COMSOL simulations. The higher is the pressure drop the higher is the resistance to the flow. As marked in the graph the drop related to the first design tested is 4 order of magnitude greater than the drop related to the last design successfully primed.

5.2 Device design and bacteria confinement

As discussed at the end of section 4.2.3, the third solution proposed for the bacteria culture module (figure 4.9), even if successfully primed and seeded with bacteria, is not yet optimised. Experimentally, it was observed that many colonies form at the entrance to the culture chamber, obstructing fluid flow, and those bacteria that do enter the chamber continue moving towards the outlet.

Figure 5.4 shows the velocity field returned by a COMSOL simulation in a 3D model reproducing the experimental geometry. Stream-lines and velocity magnitude at the plane $z = 1 \mu m$ (half of the total channel height), reveal much higher velocities inside the chamber than in the rest of the device. In the section separating the channel from the chamber, velocity magnitudes are low except for the areas closest to the walls and so only few lateral streamlines cross the chamber. Assuming that the bacteria, in the loading phase, are carried by the fluid flow, this distribution of velocities explains why many bacteria aggregate at the entrance of the chamber (zone at almost null velocity) and why those that enter the chamber continue to flow towards the outlet.

As described in section 4.2.4, to overcome those problems I started the fabrication of a double height device based on a two-layer SU-8 photoresist mould whose design is shown in figure 4.13. Although fabrication of device has not been completed, I have simulated its working principle and make some deductions about its effectiveness in terms of bacteria confinement in the central, thin chamber.

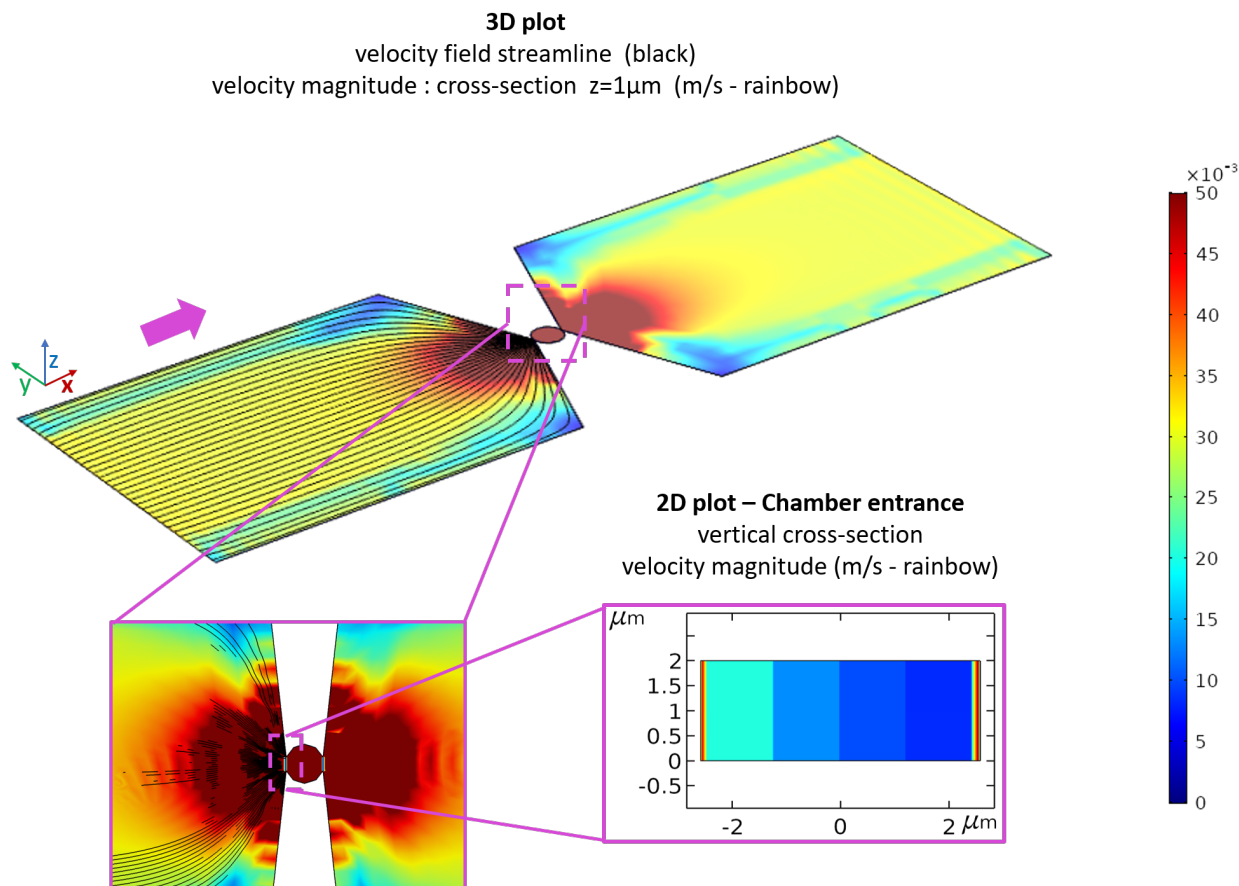
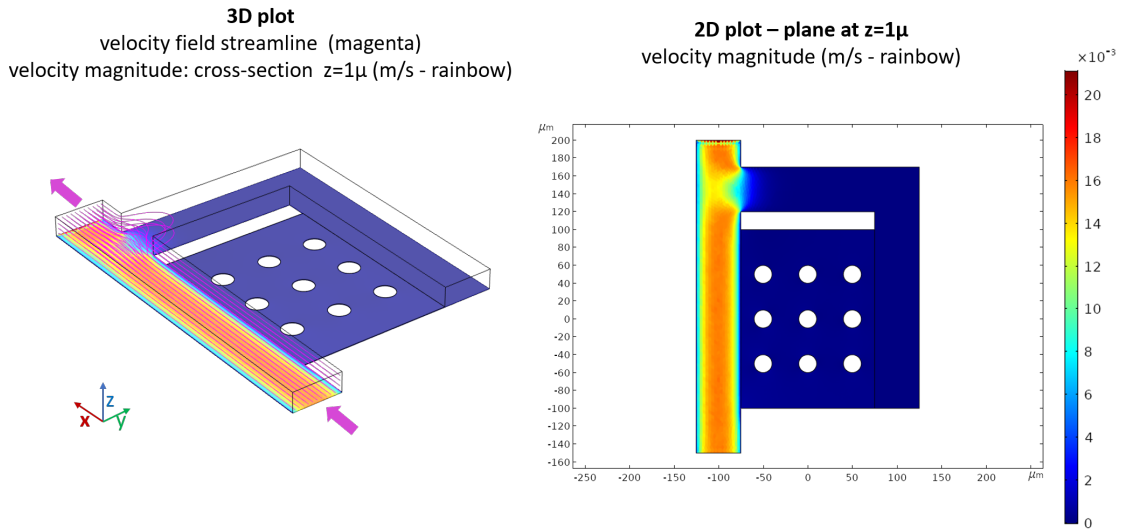


Figure 5.4: Microfluidic bacterial culture device modelling: velocities field. Magenta arrow indicates the direction of the flow. The two subsequent zooms on the area close to the central culture chamber, show how the velocity, in the flow direction, increases, then decreases abruptly to increases again once inside the chamber. The 2D plot shows the section at the intersection channel-chamber. Specular behaviour is observed at the chamber exit.

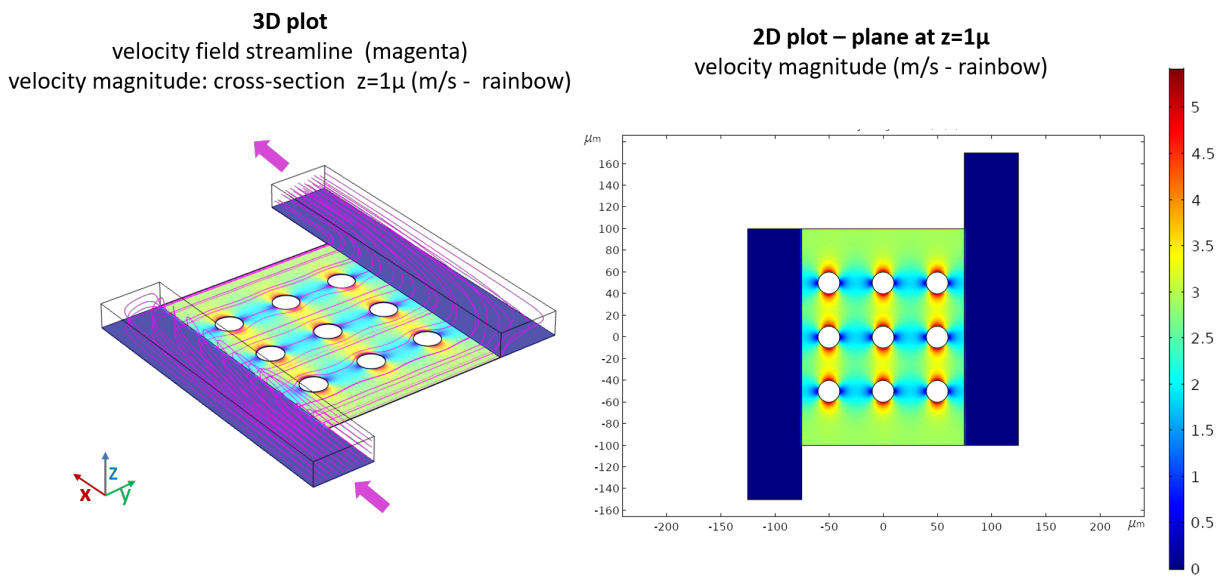
Results of the simulation of the double layer device (panel a of figure 5.5), show the flow velocity in the chamber is much lower than in the main fluid channel. This causes the streamlines to avoid the chamber with most of the fluid flowing in the channel directly connecting the inlet and outlet ports. Fabricating a higher culture chamber could eventually help the fluid to flow inside the chamber but this is not a viable solution since it may preclude the monolayer bacterial growth. I note, the fluid flow at the entrance to the culture chamber is low which may allow motile bacteria that enter this region to actively swim into and colonise the chamber however given the fluid in this region would not be replenished, growth could soon stagnate.

An alternative design is shown in panel (b) of figure 5.5. It has a modified top layer designed to force fluid to flow through the chamber. Simulation results in panel b of figure 5.5, show a maximised number of streamlines crossing the chamber. With the assumption of bacteria following the flow during the inoculation phase this should help them to enter the central chamber. However, the three orders of magnitude difference between the velocity values of

the first solution (panel a in figure 5.5) and the one of the second solution (panel b in figure 5.5) may result again in the difficulty of preventing bacteria from escaping from the chamber. Definitive answers can only be provided by experiments, but I expect that, once inside the chamber, the difference in height with the exit channel will limit their escape.



(a) *First implemented design*



(b) *Second modified design*

Figure 5.5: Double-height device for bacterial culture: COMSOL simulation results. In the 3D plots magenta arrows indicate the flow direction. In panel (a) the stream-lines in the 3D plot hardly cross the central chamber, likely resulting in bacteria not entering in the culture chamber and the 2D plot shows a very-low velocity zone in the culture chamber. In panel (b) all the stream lines in the 3D plot cross the central chamber, likely resulting in bacteria easily entering in the culture chamber and the 2D plot shows a high velocity zone in the culture chamber. Note the difference of the scales.

Chapter 6

Conclusion and future prospective

Studying bacteria in mixed co-culture systems is of paramount importance to harvest the full metabolic potential of the microbial world. Often, pathogenic microorganisms infect our body by combining into poly-microbial infections, interacting, mostly via metabolite exchange, between different species. A thorough understanding of such interactions can open new possibilities for the treatment of infectious diseases. To this end, traditional bacterial bulk cultures techniques only provide limited information regarding bacterial communication unless integrated with complex and expensive sequencing or phenotyping techniques. The main obstacle that microfluidic devices aim to overcome is the impossibility of recreating the microscopic spatial organisation, typical of bacteria natural environment. In addition, in micro-volumetric cultures, all the average effects of bulk cultures are avoided and single cell resolution can be achieved.

This work aimed to optimise the fabrication procedure of a microfluidic platform for the study of chemical interactions between two bacterial species while avoiding any physical contacts and, ultimately, provide experimental approaches to study bacterial communication. Microfluidic devices for culturing single bacterial species are numerous in the literature. In contrast, microfluidic co-culture systems are still rare and mostly focused on Eukaryotic cells.

The outcome of my work is a simple microfluidic device and associated image processing to quantify bacterial growth at the single cell level. This is only the first step towards a full mixed species platform where the entire protocol can be replicated for multiple species cultured in individual chambers separated by hydrogel barriers. Two devices have been completely fabricated and successfully primed and seeded with *E.coli* strains. Images acquired from bacteria inoculated in the device allowed me to count bacteria, for each image, and confirm an extremely slow growth rate over a 12 hour period. The low growth rate is likely partly due to the low temperature in the laboratory.

The experimental approach can return useful information about the bacterial growth rate only if the two following conditions are met:

- **Bacteria must grow in monolayers** to accurately account every bacteria. In monolayer growth chambers micro-environments are defined and single cell resolution can be achieved;

- **bacterial growth should preferentially be confined in a specific area** to be able to take microscopic images in a specific zone of known volume.

For the device fabrication step, I employed Direct Laser Writing (DLW) lithography for creation of the photoresist mould to be replicated in PDMS. The spinning of a thin layer of SU8 suitable for a bacterial monolayer culture chamber, has been achieved whose compatibility with DLW has also been demonstrated. When applicable in terms of smallest desired feature, DLW is easier to implement than e-beam lithography and in contrast to standard UV lithography, does not require a photomask.

Confinement in a specific growth chamber was not achieved in the simple, single layer PDMS device but a solution to this was proposed based on a double layer device that has been studied by computational modelling. DLW has been used to fabricate a double-layer SU-8 mould however the dimensions of the culture chamber needs to be optimised to prevent collapse. Particular attention is needed in the design of the connection between the fluid inlet/ outlet ports and the growth chamber to recreate a favourable pressure distribution that avoids high pressure drops that prevent priming and inoculation of the device.

In addition to integrating the single species microfluidic modules for bacterial culture in a mixed species co-culture device, the approaches demonstrated here can be used to dynamically monitor microorganism growth as a function of external conditions such as pH, temperature or drug administration.

6.1 Toward a mixed-species co-culturing device

Once the proposed double-layer microfluidic platform has been fabricated and tested, this could be integrated with other identical modules to build a co-culture system with access to real time single bacteria growth information. This requires that multiple chambers are connected such that metabolites can still be exchanged between species. I propose this would be could achieved using a semi-permeable membrane to provide separation between growth chambers. The alternative is to fabricate a nanometre-scale connection between chambers to allow metabolites exchange while preventing physical contact between bacterial species. Although protocols to develop such structures have been already developed, this typically requires e-beam lithography. I thus conclude that a membrane synthesised from a hydrogel would be the simplest solution.

Preliminary experiments to study how to insert a sodium alginate hydrogel within a PDMS device have been performed. As proof of principle, I demonstrated the integration of a hydrogel by punching a 6 mm diameter hole in a microfluidic channel connecting two culturing chambers. This aperture was then injected with a 1% wt/vol solution of sodium alginate and the curing agent (5% wt/vol $CaCl_2$ solution in water) with a 1:1 volume ratio. While it was possible to insert the hydrogel into the aperture within the PDMS, the protocol needs to be improved to optimise the sodium alginate viscosity and porosity. Subsequent experiments will have to be the fabrication of a PDMS channel divided by a hydrogel barrier where solutions

of different compounds can be flushed to test porosity. Testing bacteria behaviour in the channel should be the final fundamental experiment.

In order to have a device composed of two independent, double-layer culture chambers, I would have tried to insert the hydrogel in the lower layer in a microfluidic structure that combining the right dimensions with the hydrophobicity of the PDMS could prevent the hydrogel from entering in the culture chambers (figure 6.1). The scientific literature is full of examples of this technique, which can be integrated into the developed protocol.

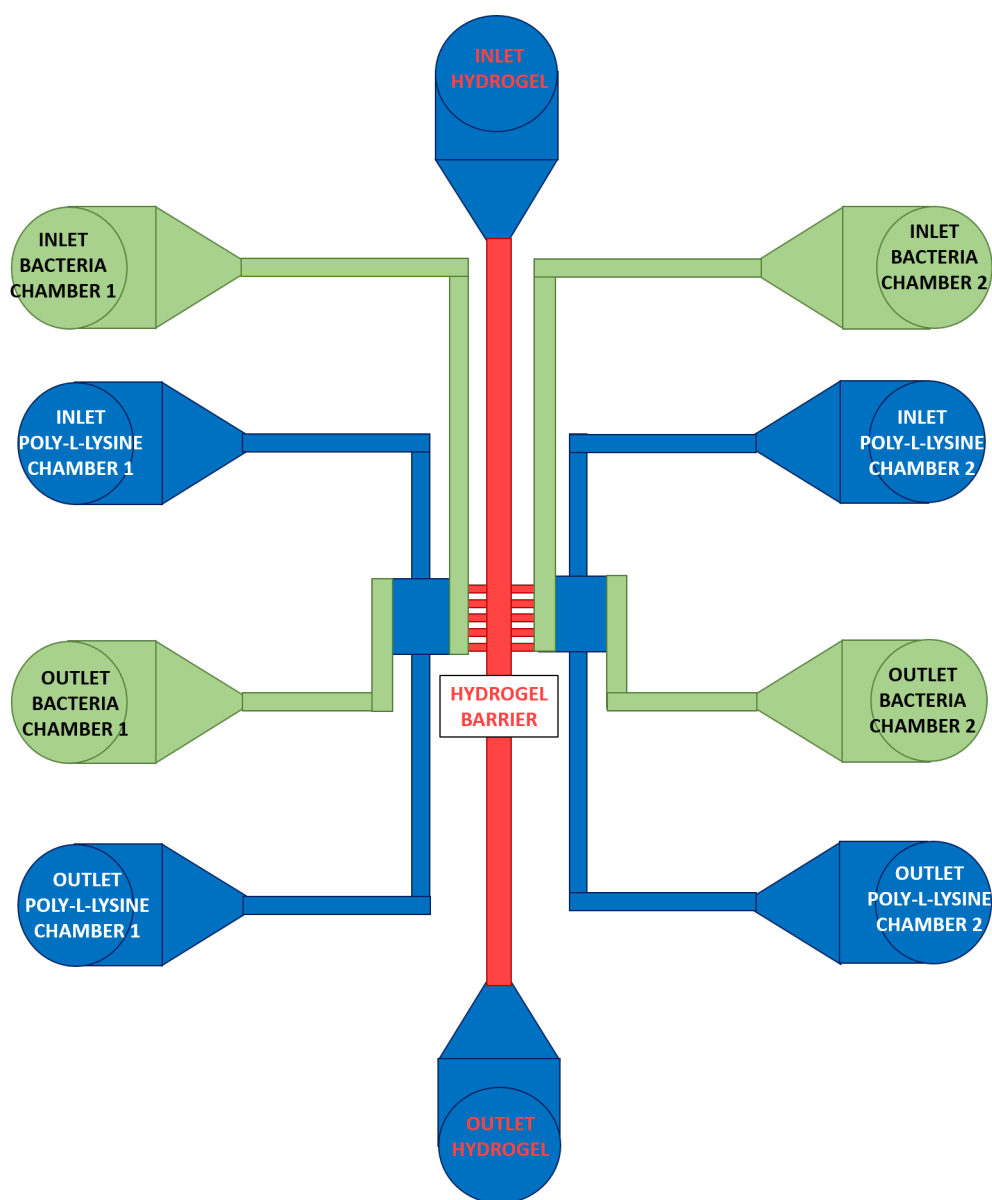


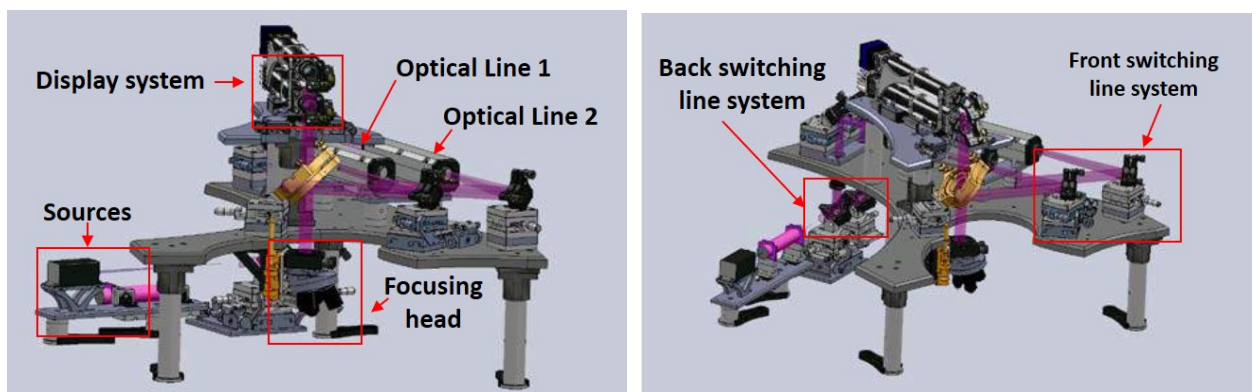
Figure 6.1: Device for bacterial co-culture in monolayer chambers: proposed design. Lower layer is indicated in blue, higher layer is indicated in green. The hydrogel is integrated in the lower layer and its polymerisation is triggered by UV light.

Figure 6.1 shows a potential design of a microfluidic platform for the co-culture of two bacterial species consisting of two, double-layer culturing microfluidic modules for bacterial monolayer growth separated by a hydrogel barrier. Here, the hydrogel is integrated in the lower layer in a fish bone structure, reproducing the fabrication implemented by Kyung Jin Son et al. [67]. Each chamber reproduces the structure simulated in COMSOL (see figure 5.5). To prevent bacteria from escaping from the chambers, the lower layer is coated with Poly-L-Lysine that promotes bacterial adhesion. Inlet and outlet ports in figure 6.1 have been designed following the simulation results described in section 5.1.

Appendix A

Dilase 650 for DLW lithography

A.1 Physical equipment



(a) *Dilase 650 lithography setup: overview*

(b) *Dilase 650 lithography setup: line switching*

Figure A.1: Dilase 650 system for DLW: lithography setup. Main optical components and relative position in the overall lithography setup consisting in two lasers sources (a) that can be directed towards two different optical lines (a) through two consecutive switching mirrors along the path (b). The first mirror introduces the laser to one of the two optical tubes defining the optical line, at the exit of the tube the second mirror switches the beam to the focusing head provided with connectors for microscope objectives (a). The display system includes the CMOS camera and the LEDs illumination (a). An absorbing filter can be mounted on the Iris diaphragms on the extremities of the optical tube. Figures adapted from [76].

A.2 Software suit

A.2.1 KloeDesign

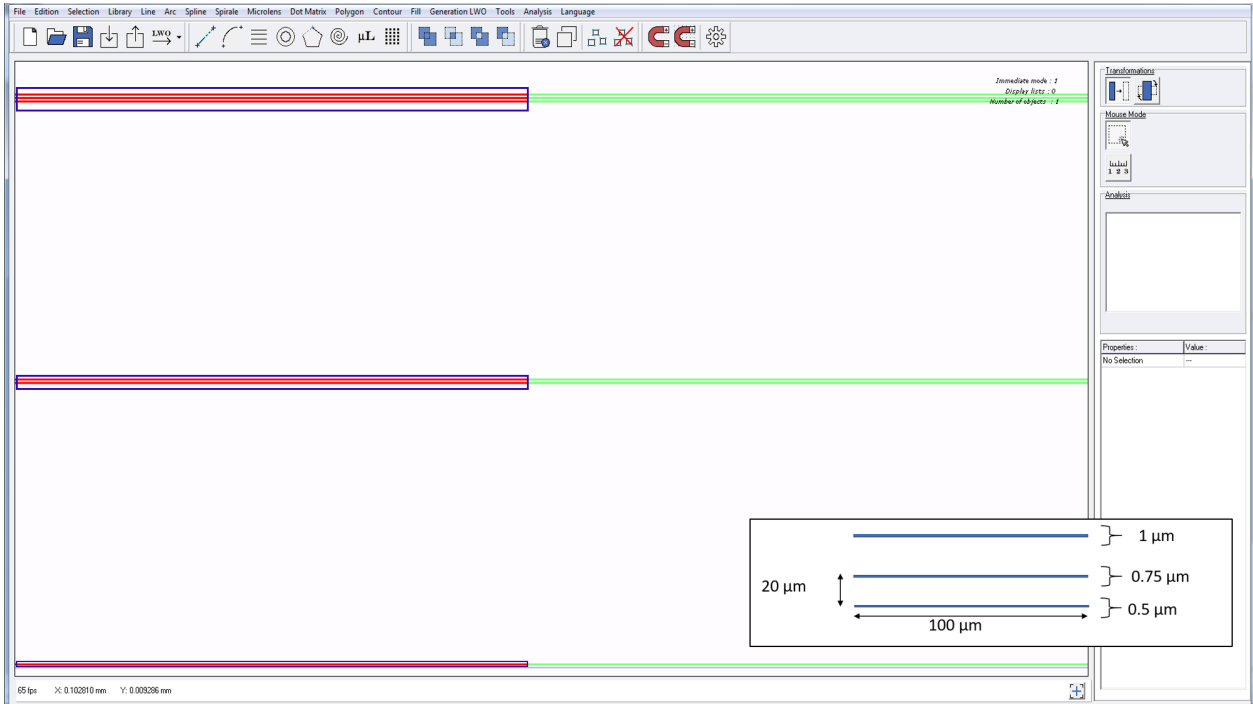


Figure A.2: KloeDesign user interface: screenshot. The software permits either direct drawing of the design file, using elementary patterns available in the software library or import and conversion of “*.DXF” and “*.GDS” files. Figure shows a zoom in on a three line drawing and fillings. Supplementary panel (bottom right) indicates their dimensions. The lines have been drawn and then filled as three rectangles with same length and increasing width. Green and red trajectories have been generated by the software as results of the filling operation and will be exported in a “*LWO” file. To have the $0.5 \mu\text{m}$, $0.75 \mu\text{m}$ and the $1 \mu\text{m}$ filled respectively by a one, two and three horizontal trajectories, filling must be completed using a $0.5 \mu\text{m}$ spot-size and an overlap rate of 50%. The red part of the filling lines will correspond to a laser ignition zone while the green zone will correspond to a laser shutdown section. The software gives the possibility to export as a “*.LWO” file the design contours, the design fillings or both.

A.2.2 DilaseSoft

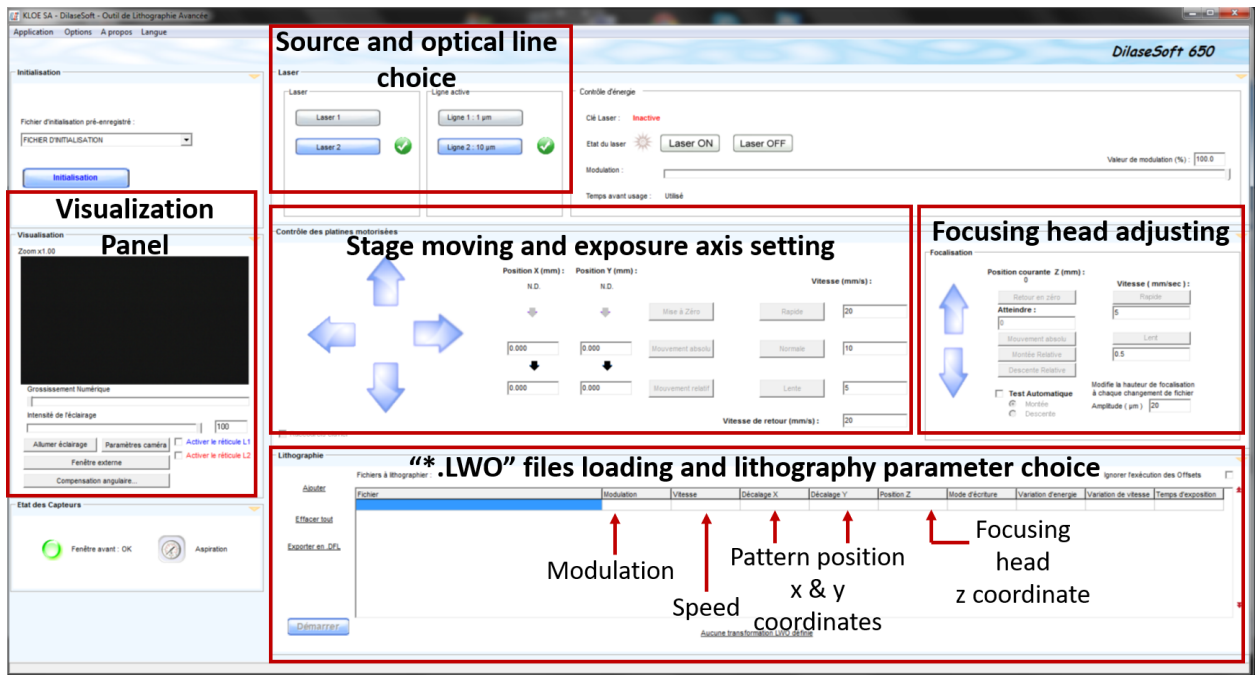


Figure A.3: DilaseSoft user interface: screenshot. Main panels and their function are indicated. In general the overall operating procedure follows the panel from top right to bottom left: from the “stage initialisation” to the “lithography setting choice”. Users can initialise the stage, choose the laser source and the optical line to use for the exposure, adjust the stage starting position defining a spatial coordination system relative to the sample, adjust the focusing height and provide the lithography setting such as energy to apply (“modulation”), “speed” at which the stage holding sample moves to complete the exposure and focal length (bottom right panel). Thanks to the display system, while using the software, it is always possible to image the sample through the objective lens. Real time images captured by the CMOS camera can be visualised in the dedicated panel.

Bibliography

- [1] R. M. Stubbendieck, C. Vargas-Bautista, and P. D. Straight, “Bacterial communities: Interactions to scale,” *Frontiers in Microbiology*, vol. 7, 2016.
- [2] J. Friedman and J. Gore, “Ecological systems biology: The dynamics of interacting populations,” *Current Opinion in Systems Biology*, vol. 1, pp. 114–121, 2017.
- [3] S. Mitri and K. R. Foster, “The genotypic view of social interactions in microbial communities,” *Annual review of genetics*, vol. 47, no. 1, pp. 247–273, 2013.
- [4] E. T. Zemanick and L. R. Hoffman, “Cystic fibrosis: Microbiology and host response,” *Pediatric clinics of North America*, vol. 63, no. 4, pp. 617–636, 2016.
- [5] C. F. Michelsen, A.-M. J. Christensen, M. S. Bojer, N. Højby, H. Ingmer, and L. Jelsbak, “Staphylococcus aureus alters growth activity, autolysis, and antibiotic tolerance in a human host-adapted pseudomonas aeruginosa lineage,” *Journal of bacteriology*, vol. 196, no. 22, pp. 3903–3911, 2014.
- [6] P. Briaud, L. Camus, S. Bastien, A. Doléans-Jordheim, F. Vandenesch, and K. Moreau, “Coexistence with pseudomonas aeruginosa alters staphylococcus aureus transcriptome, antibiotic resistance and internalization into epithelial cells,” *Scientific reports*, vol. 9, no. 1, pp. 16 564–16 564, 2019.
- [7] R. Baldan, C. Cigana, F. Testa, I. Bianconi, M. De Simone, D. Pellin, C. Di Serio, A. Bragonzi, and D. M. Cirillo, “Adaptation of pseudomonas aeruginosa in cystic fibrosis airways influences virulence of staphylococcus aureus in vitro and murine models of co-infection.(research article)(report),” *PLoS ONE*, vol. 9, no. 3, e89614, 2014.
- [8] (2019). “Cystic fibrosis faqs,” [Online]. Available: <https://www.cysticfibrosis.org.uk/> (visited on 07/17/2020).
- [9] (2017). “Who priority pathogens list for r&d of new antibiotics,” [Online]. Available: <https://www.who.int/en/news-room/detail/27-02-2017-who-publishes-list-of-bacteria-for-which-new-antibiotics-are-urgently-needed> (visited on 07/17/2020).
- [10] E. H. Wintermute and P. A. Silver, “Emergent cooperation in microbial metabolism,” *Molecular Systems Biology*, vol. 6, no. 1, 2010.
- [11] M. F. Traxler, J. D. Watrous, T. Alexandrov, P. C. Dorrestein, and R. Kolter, “Interspecies interactions stimulate diversification of the streptomyces coelicolor secreted metabolome,” *mBio*, vol. 4, no. 4, A1, 2013.

- [12] M. G. J. de Vos, M. Zagorski, A. McNally, and T. Bollenbach, "Interaction networks, ecological stability, and collective antibiotic tolerance in polymicrobial infections.," *Proceedings of the National Academy of Sciences of the United States of America*, vol. 114, no. 40, pp. 10 666–10 671, 2017.
- [13] K. Duana, C. D. Sibleya, C. J. Davidson, and M. G. Surette, "Contributions to microbiology, vol. 16: Bacterial sensing and signaling," *Mycoses*, vol. 52, no. 1, pp. 1–17, 2009.
- [14] I. Young and J. Crawford, "Interactions and self-organization in the soil-microbe complex," *Science*, vol. 304, no. 5677, pp. 1634–1637, 2004.
- [15] J. L. Mark Welch, Y. Hasegawa, N. P. McNulty, J. I. Gordon, and G. G. Borisy, "Spatial organization of a model 15-member human gut microbiota established in gnotobiotic mice," *Proceedings of the National Academy of Sciences of the United States of America*, vol. 114, no. 43, E9105–E9114, 2017.
- [16] D. Nichols, N. Cahoon, E. M. Trakhtenberg, L. Pham, A. Mehta, A. Belanger, T. Kaniyan, K. Lewis, and S. S. Epstein, "Use of ichip for high-throughput in situ cultivation of "uncultivable" microbial species," *Applied and Environmental Microbiology*, vol. 76, no. 8, p. 2445, 2010.
- [17] R. M. Stubbendieck, C. Vargas-Bautista, and P. D. Straight, "Bacterial communities: Interactions to scale.," *Frontiers in microbiology*, vol. 7, pp. 1234–1234, 2016.
- [18] L. Goers, P. Freemont, and K. M. Polizzi, "Co-culture systems and technologies: Taking synthetic biology to the next level," *Journal Of The Royal Society Interface*, vol. 11, no. 96, 2014.
- [19] B. LibreTexts. (2019). "16.1d: Microbial environments and microenvironments." LibreTexts, Ed., [Online]. Available: [https://bio.libretexts.org/Bookshelves/Microbiology/Book%3AMicrobiology_\(Boundless\)/16%3AMicrobial_Ecology/16.1%3AMicrobial_Ecology/16.1D%3AMicrobial_Environments_and_Microenvironments](https://bio.libretexts.org/Bookshelves/Microbiology/Book%3AMicrobiology_(Boundless)/16%3AMicrobial_Ecology/16.1%3AMicrobial_Ecology/16.1D%3AMicrobial_Environments_and_Microenvironments).
- [20] J. Lederberg and A. McCray, "ome sweet 'omics - a genealogical treasury of words," *Scientist*, vol. 15, no. 7, pp. 8–8, 2001.
- [21] J. A. Gilbert, M. J. Blaser, J. G. Caporaso, J. K. Jansson, S. V. Lynch, and R. Knight, "Current understanding of the human microbiome," *Nature Medicine*, vol. 24, no. 4, p. 392, 2018.
- [22] S. Altveş, H. K. Yildiz, and H. C. Vural, "Interaction of the microbiota with the human body in health and diseases.," *Bioscience of microbiota, food and health*, vol. 39, no. 2, pp. 23–32, 2020.
- [23] H. M. Project. (2016). "Nih: Human microbiome project." H. M. Project, Ed., [Online]. Available: <https://www.hmpdacc.org> (visited on 07/21/2020).
- [24] "Nih human microbiome project defines normal bacterial makeup of the body," *Targeted News Service*, 2012.
- [25] N. N. H. G. R. Institute. (2020). "The human genome project." N. N. H. G. R. Institute, Ed., [Online]. Available: <https://www.genome.gov> (visited on 07/21/2020).

- [26] Y. Belkaid and T. w. Hand, “Role of the microbiota in immunity and inflammation,” *Cell*, vol. 157, no. 1, pp. 121–141, 2014.
- [27] “Structure, function and diversity of the healthy human microbiome,” *Nature*, vol. 486, no. 7402, p. 207, 2012.
- [28] J. Lloyd-Price, C. Arze, A. N. Ananthakrishnan, M. Schirmer, J. Avila-Pacheco, T. W. Poon, E. Andrews, N. J. Ajami, K. S. Bonham, C. J. Brislawn, D. Casero, H. Courtney, A. Gonzalez, T. G. Graeber, A. B. Hall, K. Lake, C. J. Landers, H. Mallick, D. R. Plichta, M. Prasad, G. Rahnavard, J. Sauk, D. Shungin, Y. Vázquez-Baeza, R. A. White, J. Braun, L. A. Denson, J. K. Jansson, R. Knight, S. Kugathasan, D. P. B. Mcgovern, J. F. Petrosino, T. S. Stappenbeck, H. S. Winter, C. B. Clish, E. A. Franzosa, H. Vlamakis, R. J. Xavier, and C. Huttenhower, “Multi-omics of the gut microbial ecosystem in inflammatory bowel diseases,” *Nature*, vol. 569, no. 7758, pp. 655–662, 2019.
- [29] W. Zhou, M. R. Sailani, K. Contrepois, Y. Zhou, S. Ahadi, S. R. Leopold, M. J. Zhang, V. Rao, M. Avina, T. Mishra, J. Johnson, B. Lee-Mcmullen, S. Chen, A. A. Metwally, T. D. B. Tran, H. Nguyen, X. Zhou, B. Albright, B.-Y. Hong, L. Petersen, E. Bautista, B. Hanson, L. Chen, D. Spakowicz, A. Bahmani, D. Salins, B. Leopold, M. Ashland, O. Dagan-Rosenfeld, S. Rego, P. Limcaoco, E. Colbert, C. Allister, D. Perelman, C. Craig, E. Wei, H. Chaib, D. Hornburg, J. Dunn, L. Liang, S. M. S.-F. Rose, K. Kukurba, B. Piening, H. Rost, D. Tse, T. Mclaughlin, E. Sodergren, G. M. Weinstock, and M. Snyder, “Longitudinal multi-omics of host-microbe dynamics in prediabetes,” *Nature*, vol. 569, no. 7758, pp. 663–671, 2019.
- [30] J. M. Fettweis, M. G. Serrano, J. P. Brooks, D. J. Edwards, P. H. Girerd, H. I. Parikh, B. Huang, T. J. Arodz, L. Edupuganti, A. L. Glascock, J. Xu, N. R. Jimenez, S. C. Vivadelli, S. S. Fong, N. U. Sheth, S. Jean, V. Lee, Y. A. Bokhari, A. M. Lara, S. D. Mistry, R. A. Duckworth, S. P. Bradley, V. N. Koparde, X. V. Orenda, S. H. Milton, S. K. Rozycki, A. V. Matveyev, M. L. Wright, S. V. Huzurbazar, E. M. Jackson, E. Smirnova, J. Korlach, Y.-C. Tsai, M. R. Dickinson, J. L. Brooks, J. I. Drake, D. O. Chaffin, A. L. Sexton, M. G. Gravett, C. E. Rubens, N. R. Wijesooriya, K. D. Hendricks-Muñoz, K. K. Jefferson, J. F. Strauss, and G. A. Buck, “The vaginal microbiome and preterm birth,” *Nature medicine*, vol. 25, no. 6, pp. 1012–1021, 2019.
- [31] E. Baldwin, M. Walther-Antonio, A. Maclean, D. Gohl, K. Beckman, J. Chen, B. White, D. Creedon, and N. Chia, “Persistent microbial dysbiosis in preterm premature rupture of membranes from onset until delivery,” *Peerj*, vol. 3, no. 11, 2015.
- [32] V. Lloréns-Rico and J. Raes, “Tracking humans and microbes,” *Nature*, vol. 569, no. 7758, pp. 632–633, 2019.
- [33] M. Yassour, M. Y. Lim, H. S. Yun, T. L. Tickle, J. Sung, Y.-M. Song, K. Lee, E. A. Franzosa, X. C. Morgan, D. Gevers, E. S. Lander, R. J. Xavier, B. W. Birren, G. Ko, and C. Huttenhower, “Sub-clinical detection of gut microbial biomarkers of obesity and type 2 diabetes,” *eng, Genome Medicine*, vol. 8, no. 1, 2016.

- [34] V. Farrokhi, R. Nemati, F. C. Nichols, X. Yao, E. Anstadt, M. Fujiwara, J. Grady, D. Wakefield, W. Castro, J. Donaldson, and R. B. Clark, “Bacterial lipodipeptide, lipid 654, is a microbiome-associated biomarker for multiple sclerosis,” *Clinical & Translational Immunology*, vol. 2, no. 11, n/a–n/a, 2013.
- [35] Y. Lim, N. Fukuma, M. Totsika, L. Kenny, M. Morrison, and C. Punyadeera, “Oral microbiome biomarker panel to detect oral and oropharyngeal cancers in a clinical setting,” *Cancer Research*, vol. 78, no. 13, 2018.
- [36] S. Freilich, R. Zarecki, O. Eilam, E. S. Segal, C. S. Henry, M. Kupiec, U. Gophna, R. Sharan, and E. Ruppin, “Competitive and cooperative metabolic interactions in bacterial communities,” *Nature Communications*, vol. 2, no. 1, p. 589, 2011.
- [37] T. Großkopf and O. S. Soyer, “Synthetic microbial communities,” vol. 18, no. 1, pp. 72–77, 2014.
- [38] I. Lasa and C. Solano, “Polymicrobial infections: Do bacteria behave differently depending on their neighbours?” *Virulence*, vol. 9, no. 1, pp. 895–897, 2018.
- [39] E. A. Yurtsev, A. Conwill, and J. Gore, “Oscillatory dynamics in a bacterial cross-protection mutualism,” *Proceedings of the National Academy of Sciences of the United States of America*, vol. 113, no. 22, pp. 6236–6241, 2016.
- [40] S. Bertrand, N. Bohni, S. Schnee, O. Schumpp, K. Gindro, and J.-L. Wolfender, “Metabolite induction via microorganism co-culture: A potential way to enhance chemical diversity for drug discovery,” vol. 32, no. 6, pp. 1180–1204, 2014.
- [41] H. J. Kim, J. Q. Boedicker, J. W. Choi, and R. F. Ismagilov, “Defined spatial structure stabilizes a synthetic multispecies bacterial community,” *Proceedings of the National Academy of Sciences*, vol. 105, no. 47, p. 18 188, 2008.
- [42] S. Terry, J. Jerman, and J. Angell, “A gas chromatographic air analyzer fabricated on a silicon wafer,” eng, *IEEE Transactions on Electron Devices*, vol. ed-26, pp. 1880–1885, 1979.
- [43] A. Dellaquila. (2017). “Five short stories on the history of microfluidics.” Elveflow, Ed., [Online]. Available: <https://www.elveflow.com/microfluidic-reviews/general-microfluidics/history-of-microfluidics/> (visited on 07/29/2020).
- [44] T. Squires and S. Quake, “Microfluidics: Fluid physics at the nanoliter scale,” *Reviews Of Modern Physics*, vol. 77, no. 3, pp. 977–1026, 2005.
- [45] W. Zhou, J. Le, Y. Chen, Y. Cai, Z. Hong, and Y. Chai, “Recent advances in microfluidic devices for bacteria and fungus research,” *Trends in Analytical Chemistry*, vol. 112, pp. 175–195, 2019.
- [46] C. H. Chen, Y. Lu, M. L. Y. Sin, K. E. Mach, D. D. Zhang, V. Gau, J. C. Liao, and P. K. Wong, “Antimicrobial susceptibility testing using high surface-to-volume ratio microchannels,” *Analytical chemistry*, vol. 82, no. 3, pp. 1012–1019, 2010.
- [47] P. Wang, L. Robert, J. Pelletier, W. L. Dang, F. Taddei, A. Wright, and S. Jun, “Robust growth of escherichia coli,” *Current Biology*, vol. 20, no. 12, pp. 1099–1103, 2010.

- [48] J. Ollion, M. Elez, and L. Robert, “High-throughput detection and tracking of cells and intracellular spots in mother machine experiments.,” *Nature protocols*, vol. 14, no. 11, pp. 3144–3161, 2019.
- [49] J. Moffitt, J. Lee, and P. Cluzel, “The single-cell chemostat: An agarose-based, microfluidic device for high-throughput, single-cell studies of bacteria and bacterial communities,” eng, *Lab On a Chip*, vol. 12, no. 8, pp. 1487–1494, 2012.
- [50] L. Robert, J. Ollion, J. Robert, X. Song, I. Matic, and M. Elez, “Mutation dynamics and fitness effects followed in single cells.,” eng, *Science (New York, N.Y.)*, vol. 359, no. 6381, pp. 1283–1286, 2018, issn: 00368075. [Online]. Available: <http://search.proquest.com/docview/2019814219/>.
- [51] X. Zhang, K. Sun, A. Abulimiti, P. Xu, and Z. Li, “Microfluidic system for observation of bacterial culture and effects on biofilm formation at microscale,” *Micromachines*, vol. 10, no. 9, 2019.
- [52] X. Yuan, Y. Song, Y. Song, J. Xu, Y. Wu, A. Glidle, M. Cusack, U. Z. Ijaz, J. M. Cooper, W. E. Huang, and H. Yin, “Effect of laser irradiation on cell function and its implications in raman spectroscopy.,” *Applied and environmental microbiology*, vol. 84, no. 8, 2018.
- [53] F. Wu, B. G. C. Van Schie, J. E. Keymer, and C. Dekker, “Symmetry and scale orient min protein patterns in shaped bacterial sculptures,” *Nature Nanotechnology*, vol. 10, no. 8, 2015.
- [54] M. Jang, S. Yang, and P. Kim, “Microdroplet-based cell culture models and their application,” vol. 10, no. 4, pp. 310–317, 2016.
- [55] J. Q. Boedicker, L. Li, T. R. Kline, and R. F. Ismagilov, “Detecting bacteria and determining their susceptibility to antibiotics by stochastic confinement in nanoliter droplets using plug-based microfluidics,” *Lab on a Chip*, vol. 8, no. 8, pp. 1265–1272, 2008.
- [56] F. Wu and C. Dekker, *Nanofabricated structures and microfluidic devices for bacteria: From techniques to biology*, 2016.
- [57] J.-p. Frimat, M. Becker, Y.-y. Chiang, U. Marggraf, D. Janasek, J. G. Hengstler, J. Franzke, and J. West, “A microfluidic array with cellular valving for single cell co-culture,” *Lab on a Chip*, vol. 11, no. 2, pp. 231–237, 2011.
- [58] J. Männik, R. Driessen, P. Galajda, J. E. Keymer, and C. Dekker, “Bacterial growth and motility in sub-micron constrictions,” eng, *Proceedings of the National Academy of Sciences*, vol. 106, no. 35, p. 14 861, 2009.
- [59] S. van Vliet, F. J. H. Hol, T. Weenink, P. Galajda, and J. E. Keymer, “The effects of chemical interactions and culture history on the colonization of structured habitats by competing bacterial populations.,” eng, *BMC microbiology*, vol. 14, no. 1, pp. 116–116, 2014.
- [60] N. Chirani, L. Yahia, L. Gritsch, F. L. Motta, S. Chirani, and S. Faré, “History and applications of hydrogels,” *Journal of Biomedical Sciences*, vol. 4, no. 4:2, 2015.

- [61] J. W. Hong, S. Song, and J. H. Shin, “A novel microfluidic co-culture system for investigation of bacterial cancer targeting,” *Lab on a Chip*, vol. 13, no. 15, pp. 3033–3040, 2013.
- [62] K. Y. Lee and D. J. Mooney, “Alginate: Properties and biomedical applications,” *Progress in polymer science*, vol. 37, no. 1, pp. 106–126, 2012.
- [63] D. Patel, Y. Gao, K. Son, C. Siltanen, R. M. Neve, K. Ferrara, and A. Revzin, “Microfluidic co-cultures with hydrogel-based ligand trap to study paracrine signals giving rise to cancer drug resistance,” *Lab on a Chip*, vol. 15, no. 24, pp. 4614–4624, 2015.
- [64] X. Zhang, L. Li, and C. Luo, “Gel integration for microfluidic applications,” vol. 16, no. 10, pp. 1757–1776, 2016.
- [65] X. Luo, K. Shen, C. Luo, H. Ji, Q. Ouyang, and Y. Chen, “An automatic microturbidostat for bacterial culture at constant density,” *Biomedical microdevices*, vol. 12, no. 3, pp. 499–503, 2010.
- [66] M. Rothbauer, H. Zirath, and P. Ertl, “Recent advances in microfluidic technologies for cell-to-cell interaction studies,” *Lab on a chip*, vol. 18, no. 2, pp. 249–270, 2018.
- [67] K. J. Son, P. Gheibi, G. Stybayeva, A. Rahimian, and A. Revzin, “Detecting cell-secreted growth factors in microfluidic devices using bead-based biosensors,” *Microsystems & nanoengineering*, vol. 3, no. 1, p. 17 025, 2017.
- [68] P.-f. Liu, Y.-w. Cao, S.-d. Zhang, Y. Zhao, X.-g. Liu, H.-q. Shi, K.-y. Hu, G.-q. Zhu, B. Ma, and H.-t. Niu, “A bladder cancer microenvironment simulation system based on a microfluidic co-culture model,” *Oncotarget*, vol. 6, no. 35, pp. 37 695–37 705, 2015.
- [69] X. Chen and J. Shen, “Review of membranes in microfluidics,” *Journal of Chemical Technology & Biotechnology*, vol. 92, no. 2, pp. 271–282, 2017.
- [70] J. de Jong, R. G. H. Lammertink, and M. Wessling, “Membranes and microfluidics: A review,” vol. 6, no. 9, pp. 1125–1139, 2006.
- [71] J. A. Brown, V. Pensabene, D. A. Markov, V. Allwardt, M. D. Neely, M. Shi, C. M. Britt, O. S. Hoilett, Q. Yang, B. M. Brewer, P. C. Samson, L. J. McCawley, J. M. May, D. J. Webb, D. Li, A. B. Bowman, R. S. Reiserer, and J. P. Wikswo, “Recreating blood-brain barrier physiology and structure on chip: A novel neurovascular microfluidic bioreactor,” *Biomicrofluidics*, vol. 9, no. 5, p. 054 124, 2015.
- [72] K. Aran, L. A. Sasso, N. Kamdar, and J. D. Zahn, “Irreversible, direct bonding of nanoporous polymer membranes to pdms or glass microdevices,” *Lab on a chip*, vol. 10, no. 5, pp. 548–552, 2010.
- [73] B.-h. Chueh, D. Huh, C. R. Kyrtsos, T. Houssin, N. Futai, and S. Takayama, “Leakage-free bonding of porous membranes into layered microfluidic array systems,” *Analytical chemistry (Washington)*, vol. 79, no. 9, pp. 3504–3508, 2007.
- [74] W. the free encyclopedia. (2019). “Multiphoton lithography.” W. the free encyclopedia, Ed., [Online]. Available: https://en.wikipedia.org/wiki/Multiphoton_lithography (visited on 08/27/2020).

- [75] K. SA, Ed., *Multifunction photolithography system : Dilase 650*. [Online]. Available: <https://www.kloe-france.com/en/laser-lithography/photolithography-systems/direct-laser-writing/dilase-650> (visited on 08/27/2020).
- [76] *User's manual dilase 650 n 20150720*.
- [77] P. M. Dentinger, K. L. Krafcik, K. L. Simison, R. P. Janek, and J. Hachman, "High aspect ratio patterning with a proximity ultraviolet source," *Microelectronic engineering*, vol. 61, pp. 1001–1007, 2002.
- [78] M. Peleg and M. G. Corradini, "Microbial growth curves: What the models tell us and what they cannot," *Critical reviews in food science and nutrition*, vol. 51, no. 10, pp. 917–945, 2011.